Zinc Oxide Thin Films for Optoelectronic Applications

A thesis submitted in partial fulfilment of the requirements for the degree of

Doctor of Engineering (EngD)

Sriluxmi Srimurugananthan

University College London

2023

Declaration

I, Sriluxmi Srimurugananthan, confirm that the work presented in this thesis is my own. Where information has been derived from other sources, I confirm it has been indicated in the thesis.

Abstract

This thesis describes the synthesis of Zinc Oxide thin films for optoelectronic applications. Aerosol assisted chemical vapour deposition was used to deposit the Zinc Oxide thin films on to glass substrates. There were three main objectives for the work carried out in this thesis. The first was to evaluate the effect of using molecular precursors of varying Zn:O ratios to synthesise ZnO thin films. The morphology of the thin films was analysed to evaluate the relationship between the molecular structure of the precursor used and the resultant functional properties of the thin film. The effect of temperature and chemical environment on the morphology of ZnO thin films was also investigated as part of this study.

The second objective was to enhance the optoelectronic properties of zinc oxide thin films through using a seeding layer to achieve highly textured thin films. As such, the second results chapter of the thesis explores the use of ZnO films as structural templates otherwise known as ‘seeding layers’ to epitaxially grow highly self-textured, compact and transparent ZnO film coatings.

The third and final objective of the thesis was to find the optimum doping of ZnO thin films to enhance optoelectronic properties. Aluminium has been investigated as a dopant for ZnO thin films at different concentrations.

The ZnO thin films presented in this thesis have been characterised using a wide range of techniques. The optical properties of the films were characterised using UV-visible-near infrared spectroscopy. Hall effect measurements were carried out on the thin films to examine their electronic properties. X-ray diffraction (XRD) was used to look at the crystallography of the films and elemental analysis of the films was conducted using X-ray photoelectron spectroscopy (XPS). Finally, the morphology of the thin films was observed using scanning electron microscopy (SEM).

Impact statement

The research presented in this thesis represents a series of significant advancements in materials science, particularly regarding indispensable technologies that exist today. In the realm of optoelectronics, where the confluence of light and electronics is paramount, thin films measuring less than 5×10^{-7} m in thickness play a crucial role. These metal oxide films serve as the foundation for a wide range of modern planar technologies. For instance, in solar arrays, it is imperative that photons effectively reach the absorbing layer, and in LED devices, emitted light must successfully reach the eye. This necessitates the use of thin, transparent electrodes with excellent electrical conductivity.

Traditionally, most applications have relied on films of indium (III) oxide doped with tin, commonly known as tin-doped indium oxide. However, due to the critical supply risk associated with the extraction of raw indium, extensive research endeavours have been undertaken to explore alternative materials that are more abundant in the Earth's crust, yet still viable for practical applications. As this thesis is being written, researchers are actively seeking workable substitutes to mitigate the supply concerns and pave the way for sustainable optoelectronic technologies.

The research in this thesis represents a significant breakthrough in the development of thin film coatings for optoelectronic applications from a materials science perspective. The use of the newly developed precursor in this thesis, EZI, offers a fast, cost-effective, and safe route to obtain c-axis oriented ZnO thin films characterised by high purity, grain coalescence, and transparency. The synthetic route described in this work circumvents blockage issues commonly encountered and yields ZnO film coatings with morphology, orientation, thickness, and carbon contamination levels comparable to those achieved using physical vapor deposition (PVD) methods.

The second results chapter also shows promising results in using ZnO seeding layers to epitaxially grow highly textured ZnO thin films with near to monocrystalline structure. This simple two step methodology is a novel approach to achieve c-axis oriented ZnO thin films that can be achieved at low temperatures. This new methodology opens up the possibility of growing highly oriented ZnO thin films on temperature sensitive substrates for transparent optoelectronic properties.

Furthermore, it is important to highlight that the ZnO coatings produced in this study were developed at rates exceeding 40 nm/min and required minimal instrumentation without fire hazards or low-pressure configurations.

Acknowledgements

Firstly, I would like to thank my supervisors Professor Ivan Parkin and Professor Claire Carmalt for their unwavering support and guidance throughout the EngD. Ivan, thank you so much for granting me the opportunity to undertake this doctorate; I am truly grateful for the opportunity to learn, grow, and carry out research at UCL.

I am indebted to Dr Clara Sanchez-Perez for her invaluable mentoring; you took me under your wing and taught me how to use the Schlenk line. Collaborating on the ZnO seeding project has been the highlight of the project. I feel truly grateful for everything you have done for me.

I would also like to thank Dr Sanjayan Sathasivam for his support and guidance throughout the EngD. Lina Zhang, Georgia Fleet, Dr Sebastian Dixon, Faizal Amin, and Alina Negrea – thank you for all your support, encouragement and the fun times we've shared along the way!

I'd like to formally thank EPSRC M3S and NSG for funding my research. I would also like to extend my appreciation to all the staff at the Chemistry department, in particular Dr Steve Firth, Martin Vickers and Charles Willoughby.

Owen Stubbs, thank you for your unwavering support especially during the write up stage. Your words of encouragement and belief in me kept me going when I needed it most.

Finally, I would like to thank my ever understanding and supportive parents without whom none of this would be possible. *Nandri Amma and Appa*.

Table of Contents

List of Abbreviations

AACVD	Aerosol assisted chemical vapour deposition
ALCVD	Atomic layer chemical vapour deposition
ALD	Atomic layer deposition
ALE	Atomic layer epitaxy
AO	Atomic orbitals
APCVD	Atmospheric pressure chemical vapour deposition
AZO	Aluminium doped zinc oxide
B_g	Band gap
CBM	Conduction band minimum
CVD	Chemical vapour definition
DC	Direct current
DEZ	Diethyl zinc
EDX	Energy dispersive X-ray
EF	Fermi level
EZI	Ethylzinc isopropoxide
FCA	Free carrier absorption
FTO	Fluorine doped tin oxide
FV	Frank van der Merwe
FWHM	Full width half maximum
GZO	Gallium doped zinc oxide
HMS	Ecopia HMS-3000 instrument
HOMO	Highest occupied molecular orbit
ICSD	Inorganic Crystal Structure Database
IPA	Isopropanol

ITO	Tin doped indium oxide
LIQUIFOG	Ultrasonic liquid atomiser
LPCVD	Low pressure chemical vapour deposition
LUMO	Lowest unoccupied molecular orbit
MBE	Molecular beam epitaxy
NIR	Near infrared
PECVD	Plasma enhanced chemical vapour deposition
PET	Polyethylene tetraphthalate
PICVD	Photon-induced chemical vapour deposition
PLD	Pulsed lased deposition
PPA	Polypropylene adipate
PTFE	Polytetrafluoroethylene
PV	Photovoltaics
RF	Radio frequency
SEM	Scanning electron microscopy
SK	Stranski-Krastanov
SSP	Single source precursor
TCO	Transparent conducting oxide
TGA	Thermogravitational analysis
UHCVD	Ultra-high chemical vapour deposition
UHV	Ultra-high vacuum
UV	Ultraviolet
VBM	Valence band maximum
VW	Volmer Webber
XPS	X-ray photoelectron spectroscopy

XRD	X-ray diffraction

List of symbols

%	percent
°	degree
θ	theta
n	carrier concentration
μ	mobility
ρ	resistivity
Ω	ohms
°C	degrees Celsius
K	kelvin
nm	nanometre
eV	electron volt
E_F	Fermi energy
E_g	band gap
λ	wavelength
λ_p	plasma wavelength
Tc	texture coefficient
Å	angstroms
σ	conductivity
m_e	true mass
R_e	Reynolds number
Hz	Hertz
hkl	Miller plane

Table of Figures

List of Tables

Chapter 1 – Introduction

1.1 The “Rare Metal Age”

In the modern era, a wealth of information is effortlessly within reach, with just one tap. This vast reservoir of information is displayed to us through an array of digital screens, spanning from smartphones to laptop computers. Digital screens have seamlessly integrated into our lives, becoming an indispensable component of our daily routine. As the adoption of smartphones and other portable devices becomes more prevalent worldwide, the demand for such devices grows exponentially.

Despite the global ubiquity of smartphones and other devices, most people are unaware of the materials that constitute these devices which lie in their hands. The rising adoption of smartphones and other digital displays has inadvertently led to the devouring of rare earth metals which power our devices and enable us to interact with screens. Smartphones, as well as renewable energy sources such as solar panels and wind turbines which will supply an increasing proportion of our energy supply, all contain more metals than ever before. This larger consumption of rare metals is set to rise as we race towards a more green and high-tech future.

The growing dependence on rare metals can be characterised as the dawn of a new era, the “rare metal age”. “Rare” in this context refers to the difficulty in finding concentrated deposits of these metals and their limited global availability. This era signifies the increasing importance and indispensability of rare metals in various sectors and industries, highlighting their critical role in the future. For example, lithium in batteries, indium in touchscreens, terbium to produce more vibrant light in television, or dysprosium and neodymium to make stronger magnets. Such materials will have a transformative impact on the 21st century, comparable to the influence that coal and oil had on the 20th century.

1.1.1 Optoelectronic device

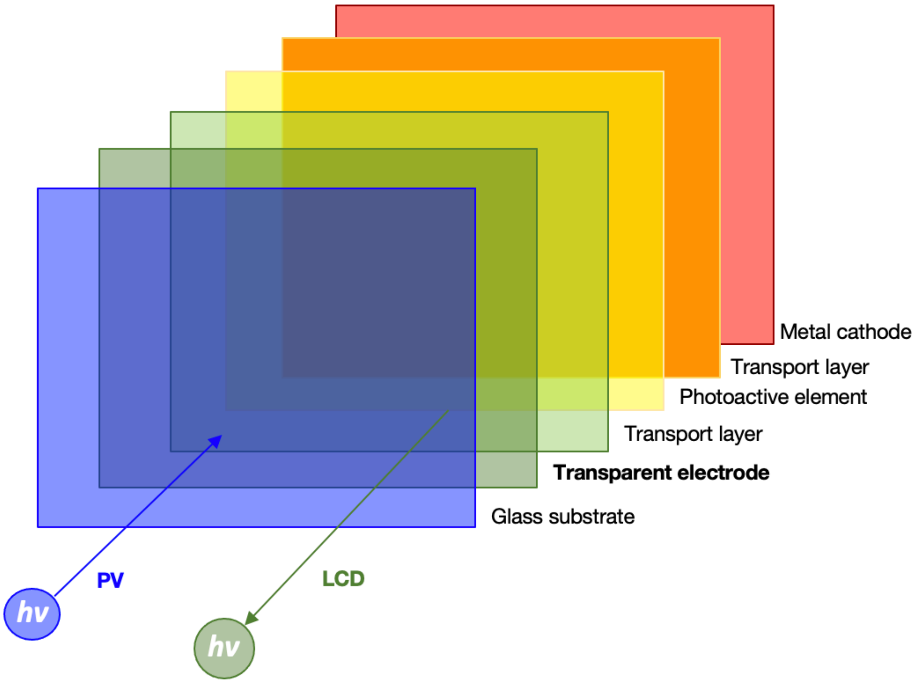

Figure 1.1 – Diagram showing the general structure of an optoelectronic device.

A generic scheme of an optoelectronic device is shown in Figure 1.1, consisting of layers of semiconducting and metallic materials. The flow of electrons forms a complete circuit, enabling the optoelectronic device to function. The flow of current to the pixel is facilitated through a rear contact called the metal cathode, typically made of aluminium (Al) or copper (Cu). This current passes through the photoemitting layer, where electrons release energy in the form of photons. The colour of these emitted photons varies depending on the characteristic of the photoemitting layer. At the front electrode electrons are extracted. A crucial feature of this front electrode is transparency to the photons emitted by the underlying layer. This transparency ensures that the emitted light is visible, allowing the device to fulfil its intended purpose.

Similarly, in photovoltaic devices, known as PVs or solar cells, a solar absorber replaces the photoemitting layer, which absorbs photons instead of emitting them. Therefore, the front electrode must be transparent to incoming light, permitting a broad range of useful radiation which maximises the PVs ability to harness energy from the light.

The thin films fabricated and presented in this thesis focus on finding substitute sustainable materials to replace the rare metals used in the transparent electrode layer of optoelectronic devices.

1.1.2 Indium Supply Risk

Optoelectronic devices are used in many applications ranging from smart watches, sensors, medical imaging devices, automotive dashboards, and refrigerators with new applications emerging regularly. Population growth, rising adoption of renewable energy technologies such as photovoltaic power generation and the diversification of optoelectronic devices all fuel the rapid expansion of the optoelectronics industry.

Taking a closer look at the transparent electrode (material of interest) found within optoelectronic devices, the current market leading material used in most applications is tin doped indium oxide (‘ITO’). Indium is classed as a rare metal due to both its relatively low concentration in the Earth’s crust, compared to more abundant materials, and its fragile supply chain. The use of ITO as transparent electrodes in optoelectronic devices is driven by its high visibility in the visible spectrum and low resistivity, making it a good electrical conductor exhibiting excellent optoelectronic properties. The exponential growth in usage of optoelectronic devices has put pressure on the global supply chain for indium to keep up with ever-increasing demand.

The use of indium-based materials such as ITO poses a supply risk in the optoelectronics industry. Indium is a relatively rare metal and is mined in just few countries around the world including China, South Korea and Japan. China is by far the largest producer of Indium, exporting indium and other rare metals to the world. This concentration makes the supply chain vulnerable to disruptions and can incur increased costs for indium-based devices. Therefore, as the demand for indium-based materials grows, there is a heightened risk of Indium supply not being able to keep up with increasing demand.

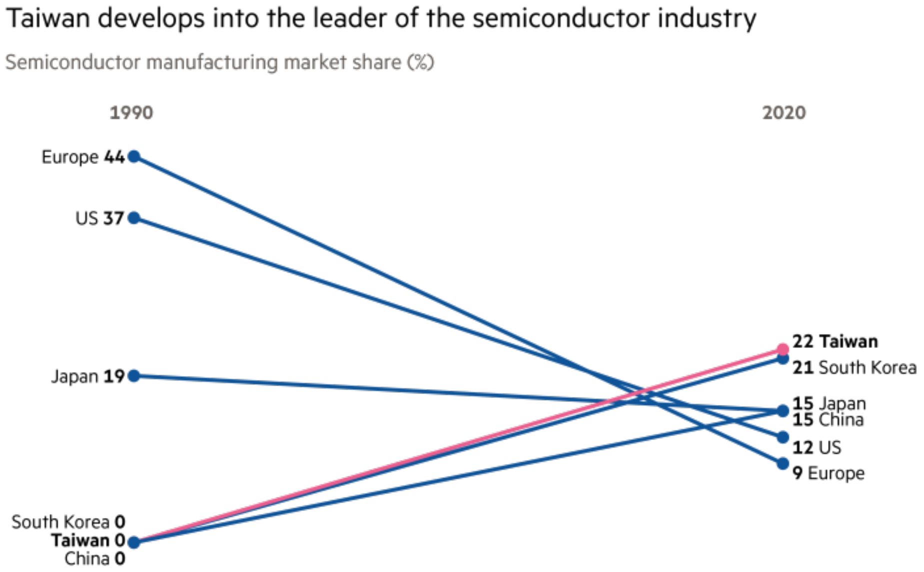

Figure 1.2 - Semiconductor industries over the last 30 years[1]

From the Financial Times. October 2022. ‘TSMC: the Taiwanese chipmaker caught up in the tech cold war.’ Hille K, Sevastopulo D.

Over the last three decades, Europe has lost its lead in the semiconductor industry; the fabrication of optoelectronic devices is now concentrated in Taiwan as seen in Figure 1.3. The combined dominance of Chinese and Taiwanese semiconductor markets together presents a tangible threat to the global economy and production of semiconductors used in optoelectronic devices.

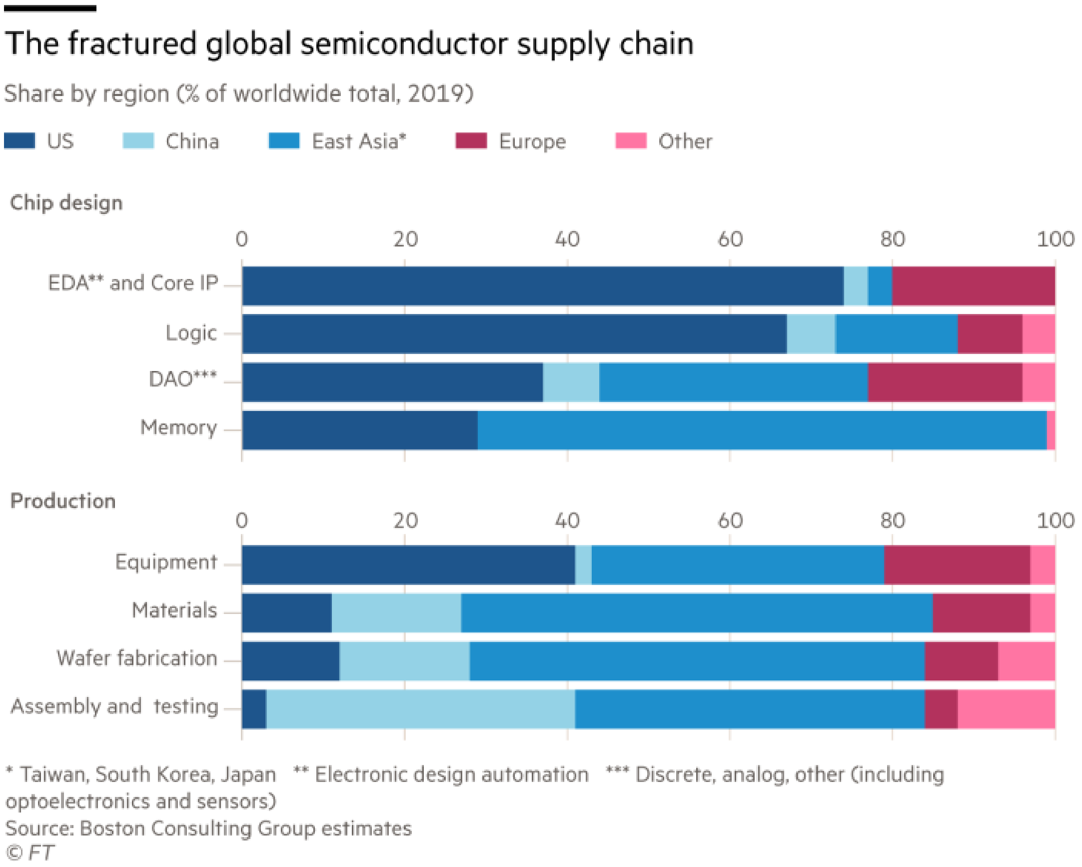
The fractured global semiconductor supply chain

Share by region (% of worldwide total, 2019)

* Taiwan, South Korea, Japan ** Electronic design automation *** Discrete, analog, other (including optoelectronics and sensors)
Source: Boston Consulting Group estimates
© FT

Figure 1.3 - The fractured global semiconductor supply chain [1]

From the Financial Times. October 2022. 'TSMC: the Taiwanese chipmaker caught up in the tech cold war.' Hille K, Sevastopulo D.

These concerns are further compounded by the ongoing 'chip war' between China and the US; American sanctions on Chinese production of chips are likely to increase the supply risk of China's indium exports to the rest of the world. China's increasingly aggressive stance over Taiwan, which produces over 60% of the world's chips, poses a significant risk to many industries worldwide including military and medical productions. The fragility of the semiconductor supply chain and huge dependence on Taiwan for high end chip fabrication has spurred Western governments to diversify chip production and find alternate sustainable materials to replace higher-risk indium-based materials.

1.2 Semiconductors

Semiconductors are the foundation of modern-day electronics; from smartwatches to automotive systems, they have become an integral component in optoelectronic devices. Semiconductors, as the name suggests, have electrical conductivity that falls between that of a conductor (such as a metal) and an insulator (such as glass).

1.2.1 Transparent Conducting Oxides

Transparent conducting oxides (material of interest in this thesis) are an important branch of semiconductors which exhibit both transparency in the visible region and electrical conductivity, two properties that are mutually exclusive otherwise.[2,3] This rare combination of properties found in TCOs make these materials useful in applications where electrical conductivity and optical transparency is simultaneously needed. TCOs have widespread use in applications such as solar cells, solid state lighting [4], smart windows[5], and flat panel displays.[2,6,7] The expansion of the display and lighting industries, along with the increasing demand for alternative greener energy sources, has fuelled the need for cost-effective and high-performance TCOs for optoelectronic applications.[6] The work presented in this thesis discusses the deposition of

ZnO based thin films as an alternative TCO material for optoelectronic applications.

1.2.2 Band Theory

Understanding the principles of conductivity in semiconductors and TCOs requires examination of the molecular orbital theory, which can be extended to solids to explain how electrons behave within a solid. Solids can be seen as a giant molecule, in which atomic orbitals interact and overlap to form molecular orbitals. As the number of atoms *N* (atomic orbitals) approaches infinity, the space between discrete energy levels of molecular orbitals decrease to form a continuous 'band' of energy levels, depicted in Figure 1.4.[8] Energy gaps, known as the band gap (E_g), can exist between bands where there are no molecular orbitals or available electronic states.

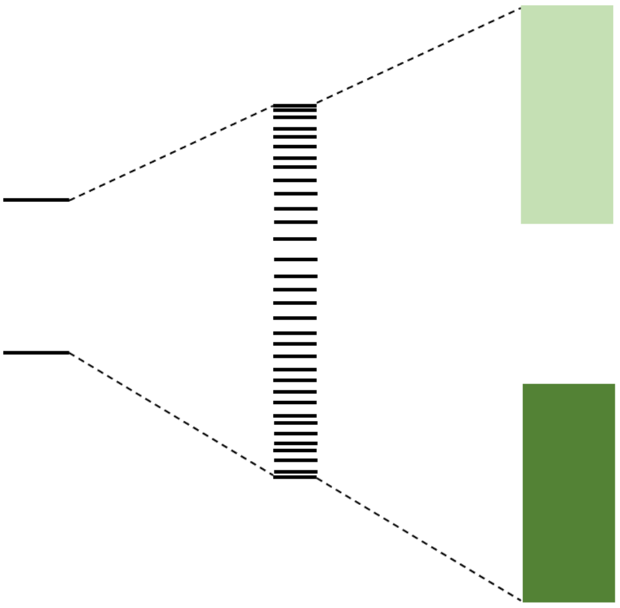

Figure 1.4 - Diagram showing the formation of bands of energy levels

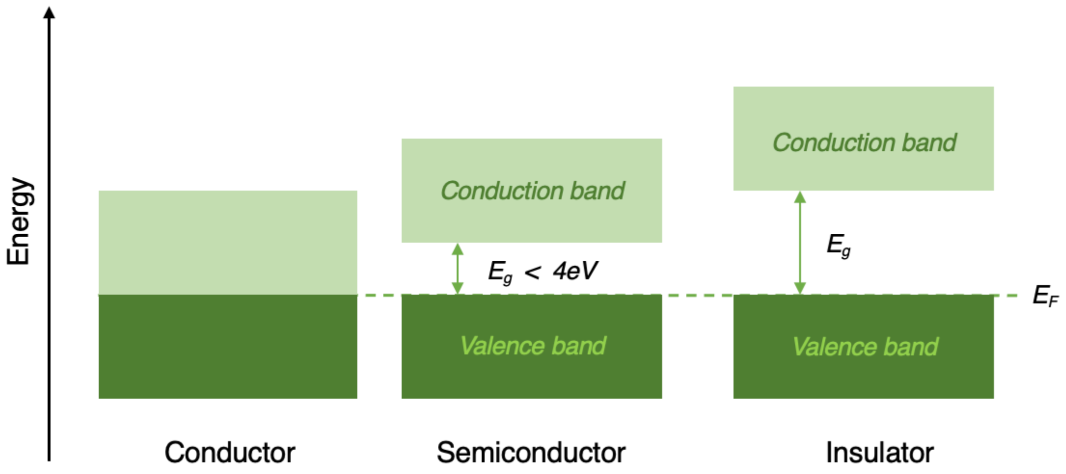

Figure 1.5 - Schematic showing the bandgaps (E_g) of conductors, semiconductors and insulators at T=0K. E_f denotes the Fermi energy. Semiconductors generally have band gaps < 4eV but this is not always the case.)

The overlap of different types of atomic orbitals (AO) gives rise to different types of bands that range over several electron volts (eV).[9,10] The overlap of antibonding atomic orbitals creates conduction bands with higher energy levels and the overlap of bonding atomic orbitals generates a valence band with lower energy levels.[11] The valence band is the band of energy levels occupied by electrons in their ground state. The conduction band can be unoccupied or partially occupied. The movement of electrons within the electronic bands (i.e., from the valence band to the conduction band) dictates electrical conductivity in a material.[12] The Fermi level, E_f, represents the highest occupied energy level at absolute zero, T=0K.

In conductors, such as metals, the valence band and conduction band partially overlap, resulting in a continuous range of energy levels available for electron movement. The movement of delocalised electrons between the valence band and conduction band are responsible for electrical conductivity in conductors.[9]

Insulators however have a large band gap between the valence band and the conduction band. The Fermi level lies at the top of the valence band, which is fully occupied by electrons, while the conduction band is empty or almost empty. As a result, there are no free electrons available to move and conduct electricity. Insulators do not conduct electricity and have a high electrical resistance due to this large band gap that prevents electron flow.

Table 1 – Band gap energies of various materials

Type of material	Band gap energy /eV
metal (conductor)	<0.3
semiconductor	<4
insulator	4-12

Semiconductors, on the other hand, exhibit intermediate behaviour. They have a band gap smaller than that of insulators but larger than that of conductors, typically less than 4eV. At low temperatures, semiconductors tend to behave as insulators and the electrons do not have enough energy to be excited into the conduction band. However, upon irradiation or heating electrons can be excited from the valence band into the conduction band. Therefore, at higher temperatures semiconductor materials tend to have higher electrical conductivities.[13] In contrast, in conductors such as metals, electrical conductivity is significantly reduced at higher temperatures due to the increased resistance caused by thermal vibrations within the lattice.

The conductivity of semiconductors can also be enhanced by doping, which involves intentionally introducing impurities to alter the number of free electrons or electron deficiencies (holes) in the material.

In summary, conductivity in terms of band theory is based on the availability of free electrons in the conduction band that can move and carry an electric current. Conductors have overlapping bands, insulators have a large band gap, and semiconductors have a moderate band gap that can be manipulated to control their conductivity.

1.2.3 Direct and indirect semiconductors

In semiconductors, the movement of electrons from the valence band to the conduction band can take place in two types of electronic transitions: direct and indirect, as shown in the figure below.

For direct band gap semiconductors, the conduction band minimum and the valence band maximum align at the same crystal momentum. This means electrons in these bands move in the same vector. In such materials, the transition of an electron from the valence band to the conduction band requires the conservation of momentum, necessitating the absorption of a photon for electronic promotion (as shown in the Figure 1.6). Zinc oxide (ZnO), amorphous silicon (Si) and gallium arsenide (GaAS) are examples of direct band gap semiconductors.[14]

On the other hand, semiconductors with an indirect band gap have different crystal momentum and the conduction band minimum and the valence band maximum do not align.[15] As depicted in Figure 1.6, electron excitation from the valence band to the conduction band necessitates both a photon and a phonon for conservation of momentum.[16] A phonon represents lattice vibrations and possesses low energy but high momentum and is an additional non radiative process which takes place in indirect semiconductors.

Consequently, indirect band gap semiconductors tend to have poor optical properties due to the reduced likelihood of electron and phonon interactions causing lower rate of radiative emission. Thus, the poor optical properties and inefficient electronic transitions observed in indirect band gap semiconductors makes these materials less favourable for transparent electrode applications. Some examples of indirect band gap semiconductors include crystalline Si and germanium (Ge).

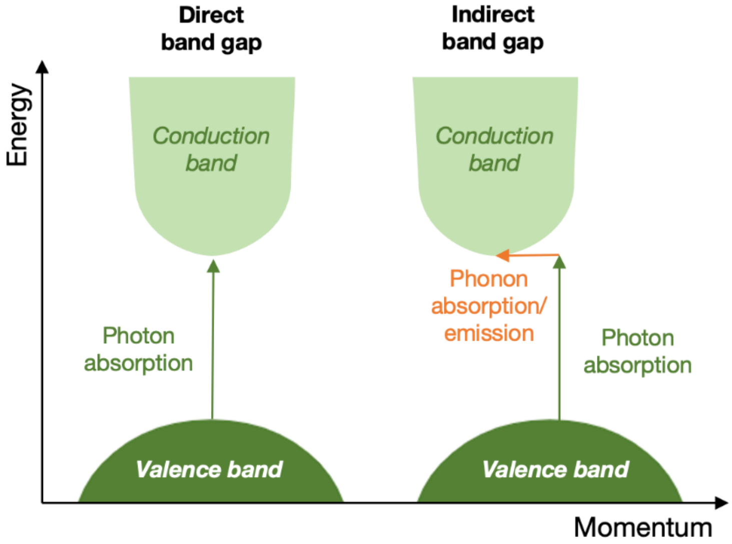

Figure 1.6 - Schematic showing the electronic processes in direct and indirect band gap semiconductors.

1.2.4 Intrinsic semiconductors

Semiconductors typically exist as crystalline solids, although they can also be found in amorphous forms. Pure semiconductors are undoped and can be referred to as intrinsic semiconductors or i-type semiconductors. In such semiconductors, the concentration of charge carriers is determined solely by the material itself and not by the influence of external species.[9]

Pure semiconductors typically exhibit low conductivity due to a limited number of crystal defects, which are necessary for generating charge carriers (electrons and holes).[9] However, at room temperature, some electrons can acquire enough thermal energy to cross the band gap and transition to the conduction band, becoming free electrons. These thermally excited electrons increase the number of free electrons and allows for some conductivity in pure semiconductors.

At a finite temperature, the Fermi level (E_F) in an intrinsic semiconductor resides midway between the valence band maximum (VBM) and the conduction band minimum (CBM).

1.2.5 Extrinsic semiconductors

As mentioned above the conductivity of semiconductors can be enhanced through adding impurities to increase or decrease the number of electrons, thus improving electrical conduction.[17] This method is commonly known as doping where the impurities added is referred to as a dopant and the doped semiconductor is called an extrinsic semiconductor.[18] N-type doping or p-type doping can be used to incorporate impurities.[2,11]

In n-type semiconductors, an impurity known as a donor substitutes an atom in the lattice structure. The donor has a higher valency, meaning it possesses one additional valence electron. The donor impurity provides an extra electron available for conduction. The Fermi level (E_F) shifts closer to the conduction band in n-type semiconductors, allowing electrons to be easily donated directly into the conduction band (see Figure 1.7). The free electrons introduced as a result of doping serve as mobile charge carriers and electron flow occurs through the conduction band. ITO is an example of a n-type semiconductor; the addition of tin (Sn), a group IV element with greater valency, as a dopant to indium oxide (group III element).

In contrast, in p-type semiconductors an impurity known as an acceptor substitutes the lattice atom, which has one less valence electron. The Fermi level (E_F) moves closer to the valence band in p-type semiconductors and the acceptor atom can easily accept an electron leaving a “hole” behind in the valence band. P-type semiconductors have positive charge carriers referred to as "holes" as the majority carriers and electron flow occurs through a continuous process of electrons hopping into available "holes" within the valence band which can conduct electricity. The addition of Zn atoms to GaAs is an example of a p-type semiconductor.

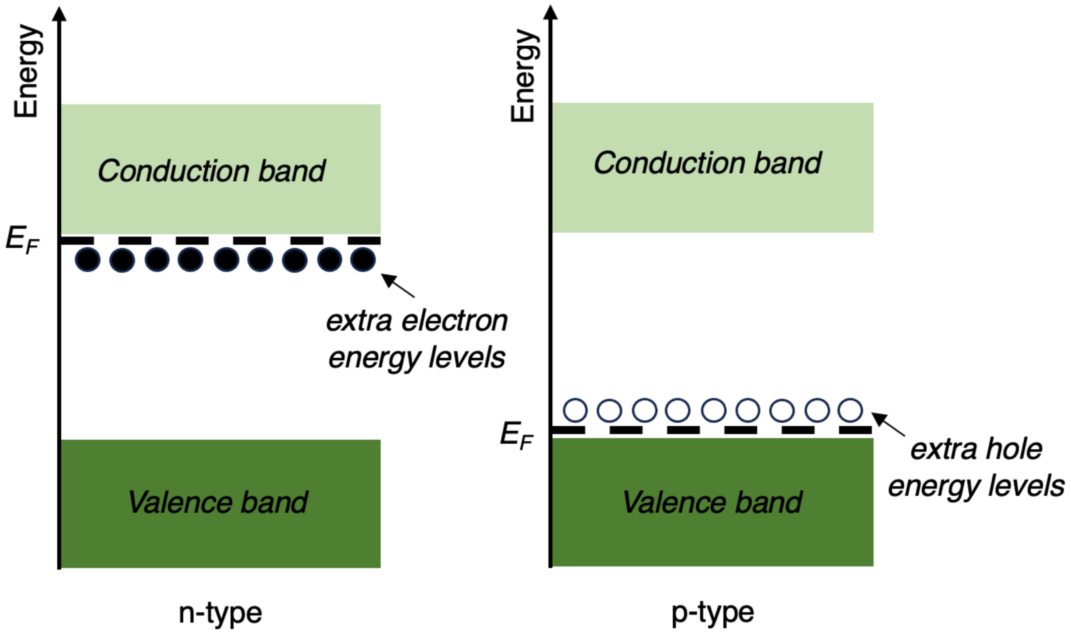

Figure 1.7 - Diagram illustrating n-type and p-type doping in semiconductors

1.2.6 Moss-Burstein Effect

In semiconductors, the valence band maximum (VBM) corresponds to the highest occupied molecular orbital (HOMO), and the conduction band minimum (CBM) represents the lowest unoccupied molecular orbital (LUMO). The absorption of a photon provides the energy needed for the excitation of electrons across the band gap into the conduction band. As the band gap increases, higher-energy photons are needed to supply sufficient energy for electrons to transition to the conduction band. The visible portion of the electromagnetic spectrum lies between 400-750 nm (i.e., energies between 3.1-1.7 eV), an optical band gap Eg opt > 3.1 eV results in visible transparency. For a TCO to be optically transparent in the visible range, the band gap to needs to be greater than *E*g = 3.1 eV. The widening of the bandgap above 3.1eV to achieve optical transparency increases the energy difference between the VBM and CBM. As a result this increase decreases the likelihood of exciting an electron into the conduction band.[2,19]

The fundamental band gap between the VBM and CBM is denoted as E_g and the optical band gap is denoted as E_g^{opt}. This optical bandgap determines the transparency of a TCO material which is an important extrinsic property of TCOs. There is an important differentiation between the band gap and optical bandgap which indicates the lowest energy level for allowed optical transitions.

TCOs have been developed to overcome this challenge by introducing doping into the material, which facilitates the generation of charge carriers. In an n-type TCO, electrons can be injected from a nearby defect donor level directly into the conduction band, enabling conductivity.[20] In these n-type TCOs, lattice defects within a metal oxide crystal (oxygen vacancies, proton interstitials, and specific substitutional defects) create an excess of electrons near the defect location. If there is sufficient orbital overlap, it allows the electrons from the defect sites to spread out or delocalise, filling the electronic states at the conduction band minimum (CBM). As a result, the Fermi level shifts above the CBM.[21–23] This effect is called the Moss-Burstein shift, and leads to an expansion of the optical band gap as follows[24–26]:

$$E_{\mathrm{g}} = E_{\mathrm{CBM}} - E_{VBM}$$

to

$$E_g^{opt} = E_g^{MB} + E_{\mathrm{g}} = E_{\mathrm{F}} - E_{VBM}$$

since the Moss-Burstein shift is:

$$E_g^{MB} = E_{\mathrm{F}} - E_{CBM}$$

where E_g is represents the fundamental energy gap, E_g^{opt} denotes optical bandgap, E_g^{MB} is known as the Moss-Burstein shift and E_F represents the Fermi level. Therefore, lattice defects in TCOs play a role in enhancing both optical transparency and electrical conductivity.

1.3 Transparent Conducting Oxides (TCOs)

TCOs exhibit both optical transparency and electrical conductivity; attracting scientific interest due to this particular combination of properties.[3] The unique combination of properties in transparent conducting oxides makes them ideal for a variety of applications, including solar cells[4], solid state lighting[27] and flat panel displays.[28] The expanding display and lighting industries and the increasing demand for greener energy has driven the need for affordable, high-performance TCOs in optoelectronics.

TCOs tend to be either binary or ternary metal oxides (one or two metals elements combined with oxygen) and wide bandgap semiconductors.[19] Doping is used to improve their TCO properties for optoelectronic applications.

To maintain transparency in TCO materials, the bandgap must exceed $E_g = 3.1$ eV to prevent absorption of visible light ($\lambda = 400 – 700$ nm) and achieve transmittance greater than 80% across the visible spectrum. To match the electrical conductivity of metals, TCOs need to have resistivities as low as 10^{-4} $\Omega \cdot$cm, along with high carrier concentration and mobility.[29]

1.3.1 Tin doped indium oxide

Tin-doped indium oxide (ITO) is the leading TCO material used on an industrial scale as a transparent electrode in optoelectronic devices. ITO displays optimal optoelectronic properties with high transparency in the visible range and low resistivity. Polycrystalline ITO has a low resistivity of 1-2 x 10^{-4} Ω·cm, making it an effective conductor. ITO films are typically grown through magnetron sputtering in industrial applications. While ITO possesses the desirable properties for TCOs, it is made from indium, a rare metal with low natural abundance. As a result, the cost of indium can be unpredictable and expensive.

Additionally, indium is primarily produced through zinc refining, where it is obtained as a by-product. As the demand for indium-based materials increases, the supply of indium through zinc refining will struggle to keep up with demand and demand will soon outstrip supply.[31] In order to keep up with demand a shift to primary indium refining will become necessary. This transition however will come at an increased cost as current sourcing methods benefits from the shared production costs with zinc. As a result, the production of indium will become costly and subject to significant price fluctuations. Ultimately costing the end consumers reliant on indium-based devices.

From the concentration of device fabrication in Taiwan all the way down to the ores from which indium are extracted from, primarily in China, the supply chain of indium-based materials sits on wobbly foundations making its supply chain vulnerable to disruptions and unpredictable spikes in pricing.

Therefore, the search for alternative low cost and sustainable replacements for indium-based materials in optoelectronic applications is urgent. The production of ITO for use as transparent electrodes or TCOs in an optoelectronic device is the primary demand for indium supply.[32] Developing alternate sustainable and high performing TCO materials to replace ITO is of upmost importance in the semiconductor industry and wider scientific community worldwide.

However, due to its low natural abundance and localised geological distribution, the commercial supply of indium is expensive and in a perpetual state of risk, which is problematic for several reasons. As such, it has naturally become desirable to seek an alternative to ITO as a commercial TCO, which is evident from the amount of research dedicated to this end in recent years.

1.3.2 Fluorine Doped Tin Oxide

Fluorine doped Tin Oxide (FTO) is another widely used transparent conducting oxide (TCO). Fluorine doped Tin Oxide thin films were originally produced using spray pyrolysis. During World War II, FTO films were primarily used as anti-fog coatings in aircrafts. In the 1990s, industrial manufacturing of FTO films moved away from spray pyrolysis to being grown via Atmospheric Pressure Chemical Vapour Deposition (APCVD).

FTO films maintain the same rutile structure as bulk tin oxide (SnO_2). Unlike ITO thin films, the addition of fluorine does not cause an expansion in the lattice parameters. This is due to the smaller iconic radius of F (1.77 Å) than O^{2-} (1.22 Å). As a result of its smaller iconic radius, fluorine doping causes a contraction in the unit cell of FTO films.[33,34]

At room temperature, undoped tin oxide is known to have a band gap of 3.6eV. Upon Fluorine doping, the bandgap increases to 4.2eV at room temperature, owing to the Moss-Burstein effect. FTO is also a n-type semiconductor, like ITO. Highly conductive FTO thin films have been produced with resistivities as low as 10^{-4} Ω·cm, carrier concentrations on the order of 10^{20} cm^{-3} and Hall mobilities ranging from approximately 1-20 $cm^2/V{\cdot}s$.[35–37] FTO thin films exhibit lower electrical conductivity with higher resistivity in comparison to ITO thin films making it unfit for optoelectronic devices that require thin films with higher conductivities. Compared ITO, FTO also has lower transparency in the visible region which is disadvantageous for display applications such as touchscreens where high visible transparency is essential.

APCVD depositions of FTO thin films require the use of scrubbers to remove harmful gases from the exhaust gases generated during manufacturing. The installation and maintenance of scrubbers in the manufacturing process increasing operational costs of FTO thin film production which is then passed onto the cost of electronic devices. The additional expenses involved in using halogen doping and the lower optoelectronic properties of FTO in comparison to ITO means a suitable sustainable replacement for ITO remains to be found.

1.3.3 Zinc Oxide

Zinc oxide has a wide direct band gap of 3.37eV, Eg > 3.1 eV, enabling visible light to pass through and making it transparent. The high transparency of ZnO in the visible region makes it suitable as a transparent electrode for applications such as solar cells and transparent displays. ZnO is a n-type semiconductor and is typically doped to increase the number of charge carriers and enhance electrical conductivity. Zinc is a relatively abundant element and exhibits good stability in its oxide form. The combination of wide band gap, high transparency, electrical conductivity, good stability and high natural abundance places ZnO in good stead as a TCO material.

Zinc Oxide occurs in three possible polymorphs: cubic rocksalt, cubic zincblende and hexagonal wurtzite. In thin films, Zinc Oxide almost exclusively exists in the wurtzite crystal structure as this is the most thermodynamically stable polymorph. At considerably higher pressures the wurtzite structure can be transitioned into the cubic rock salt crystal structure. The zinc blende structure is rare and only remains stable when grown epitaxially on cubic substrates. The standard XRD pattern of ZnO in the wurtzite crystal structure, commonly observed in ZnO thin films, is show in the figure below. This standard is used throughout the thesis to identify the crystal phases present in thin films; by comparing the observed diffraction pattern of the sample with the XRD pattern of the standard shown in the figure below.

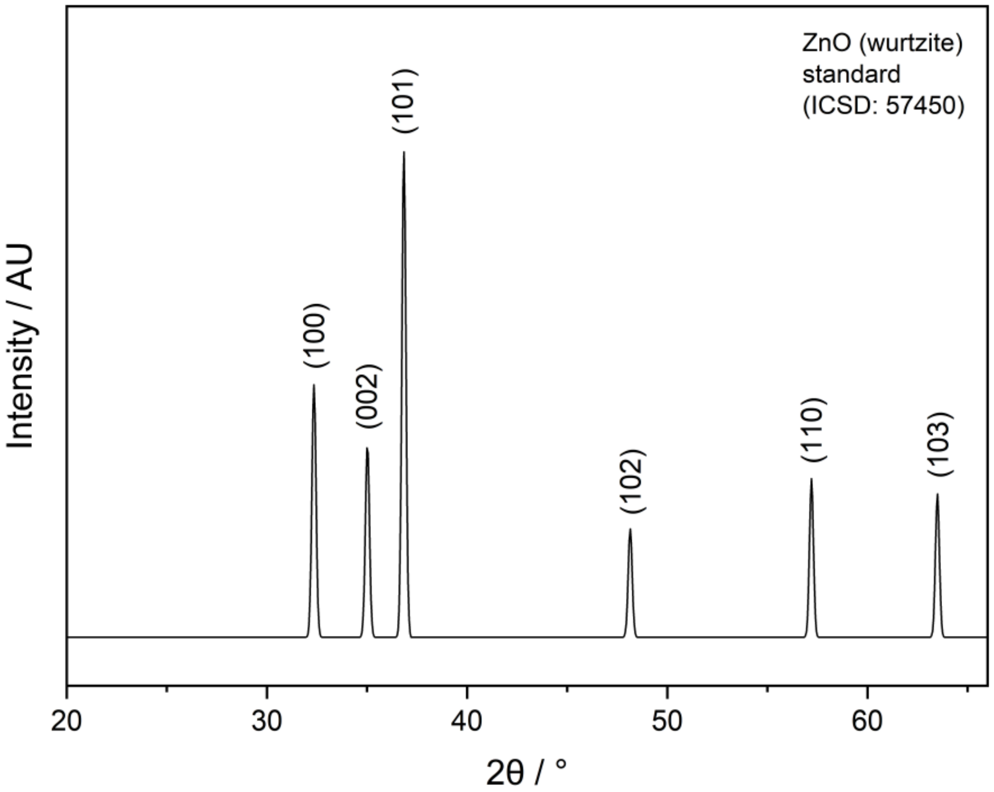

Figure 1.8 - Standard XRD pattern of wurtzite phase of ZnO

In the wurtzite crystal structure of ZnO, the zinc centre adopts a tetrahedral geometry with four oxygen on each corner of the tetrahedron as shown in the diagram below. Similarly, each oxygen atom is surrounded by four zinc atoms, also forming a tetrahedral configuration. This arrangement creates a tightly packed structure with a hexagonal geometry (hexagonal close-packed structure) in the wurtzite lattice of ZnO. Zn^{2+} and O^{2-} have an ionic radius of 0.74 Å and 1.34 Å, respectively.

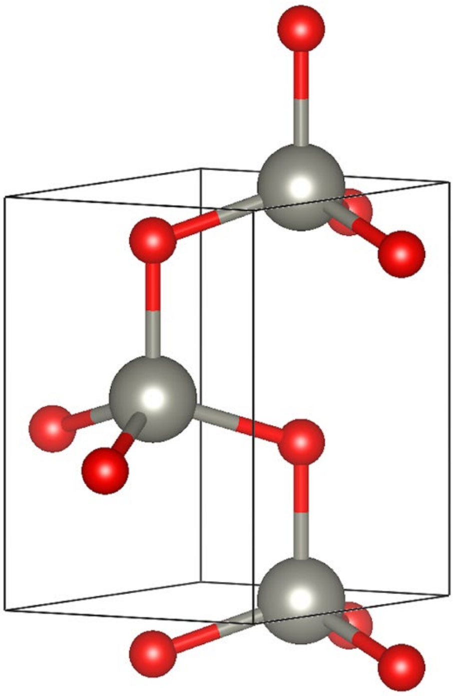

Figure 1.9 - The wurtzite unit cell of Zinc Oxide whereby grey represents Zn^{2+} and red represents O^{2-}.

Electrical conductivity comparable to ITO has been achieved by doping Zinc Oxide with trivalent elements such as Al and Ga. A study by Minami *et al* has shown the resistivity of impurity doped ZnO films has continued to decrease over the last three decades, while research findings show the resistivity values of SnO_2 and In_2O_3 thin films have remained relatively stable.[6] From this analysis of resistivity values in impurity-doped thin film coatings of binary compound TCOs, ZnO holds great promise as a viable alternative to ITO. The relatively natural abundance of Zinc reduces the production cost of ZnO when compared with rare metal TCOs like ITO. The low-cost production combined with good comparable optoelectronic properties and non-toxicity makes ZnO an attractive choice for TCO applications.[38]

1.4 Properties of TCOs

Conductivity and transparency in Transparent Conducting Oxides (TCOs) are achieved by incorporating dopants or creating non-stoichiometric compositions. By employing degenerate doping, these TCO materials have their conduction bands populated with free electrons, resulting in high conductivity. [39] For novel TCO materials, it is ideal for the electrical resistivity to be around 10^{-5} Ω·cm, with an absorption coefficient typically lower than 10^{4} cm^{-1} in the near UV and visible range. Moreover, a band gap greater than 3.1 eV is preferred to ensure optical transparency in the visible spectrum.

1.4.1 Electrical properties

The conductivity of Transparent Conducting Oxides (TCOs) relies on the presence of charge carriers and their mobility within the metal oxide. The mobility describes the ability of these charge carriers, whether electrons, ions, or holes, to move through the material.[40] As a result, conductivity (σ, measured in S cm^{-1}) can be directly related to the microscopic parameters that define the movement of charge carriers within the material.

$$\sigma = ne\mu$$

$$\mu = e\tau/m^*$$

$$\sigma = ne(e\tau/m^*)$$

Where n denotes carrier concentration (cm^{-3}), e represents the charge of an electron (1.602×10^{-19}C), τ denotes relaxation time between collisions, and m^* denotes effective mass of the electron. Through increasing carrier concentration or mobility, electrical conductivity can be enhanced as these values are directly correlated as seen in the equation above. The carrier concentration consists only of electrons that can be easily excited from occupied states to empty states. As a result, electrons with energies very close to the Fermi level (E_F) can contribute to conductivity. The remaining electrons are localised. Without external excitations, such as light, thermal excitation is needed.

In an n-type Transparent Conducting Oxide (TCO), the mobility of electrons, or their ability to move through the metal oxide, is inversely proportional to their effective mass. The effective mass describes the apparent mass of electrons as they move through the material. Mobility is affected by how electrons respond to local forces within the solid and is defined in relation to the electron's true mass (m_e).[41] Importantly, the effective mass (m^*) is influenced by the bandwidth, which is determined by the overlap of electron orbitals.

The electrical resistivity, ρ (Ω cm), of TCOs is represented by:

$$\mathrm{r} = s^{-1} = \frac{1}{nem}$$

The electrical resistivity, ρ (Ω cm), of TCOs needs to be minimised and is an important consideration in TCO development. From the equation above, electron density represented by n, and the electron mobility denoted as µ influence the electrical resistivity (as well as the conductivity of a material).

The sheet resistance of thin films, R_{sh}, is calculated using the equation below whereby ρ is the resistivity of the film and d is the thickness of the thin film.

$$R_{sh} = \frac{r}{d}$$

In order for a Transparent Conducting Oxide (TCO) to be applicable in optoelectronic applications, it is crucial to optimise its charge carrier mobility to approximately 50-70 $cm^2V^{-1}s^{-1}$. Additionally, it is desirable to maintain low electrical resistivity, ideally within the range of $\rho = 10^{-4}$-10^{-5}, while simultaneously keeping the carrier concentration below $2x10^{21}cm^{-3}$ to minimise optical absorption.[40] It should be noted that heavy doping in n-type TCOs introduces donor electrons into the conduction band, widening the band gap. However, the optical absorption associated with the excitation of electrons from the conduction band minimum (CBM) to higher energy states sets an upper limit on the carrier concentration in the CBM.

This can be expressed as the absorption coefficient α of the TCO as show in the equation below:

$$\alpha = n\sigma$$

where σ represents the absorption coefficient cross-section. Therefore, these limitations must be considered when designing TCOs. Optimising TCO properties, requires trade-offs since no single TCO formula is ideal.[20]

$$\alpha = {}^{\lambda^2 e^3 N}\!/_{4\pi^2 \varepsilon_0 c^3 n (m_e^*)^2 \mu_{opt}}$$

From this equation the absorption coefficient is directly proportional to the wavelength and carrier concentration. In the equation above, λ represents the photon wavelength, e denotes the elementary charge, N stands for the free carrier concentration, ε_0 represents the permittivity in vacuum, n signifies the refractive index, e_m^* indicates the effective electron mass, and μ_{opt} represents the optical mobility.

Upon irradiation of electromagnetic waves, the carriers within the conductor oscillate collectively at the same frequency as these waves, a phenomenon known as plasma oscillation. The plasma frequency, denoted as ω_p, characterises the threshold frequency for plasma oscillation and is proportional to the carrier concentration and effective mass of the charge carriers as shown in the equation below:

$$\omega_p^2 = \frac{Ne^2}{\varepsilon_0 \varepsilon_{opt} m_e^*}$$

N represents the density of free charge carriers, e is the electron charge, ε_0 and ε_∞ represent the permittivity in vacuum and at high frequencies, respectively, and m_e^* denotes the effective mass of electrons.

The equation highlights how the plasma frequency is determined by the carrier concentration and the effective mass of the charge carriers. In TCOs, optimising carrier concentration and mobility is crucial for achieving high conductivity and transparency. Increasing carrier concentration (n) while maintaining high mobility (μ) can enhance the plasma frequency, leading to improved electrical conductivity and optical transparency in TCO materials. Therefore, understanding and controlling these parameters are essential for designing efficient TCOs for various applications such as transparent electrodes in displays, solar cells, and optoelectronic devices.

1.4.2 Optical properties

The optical bandgap dictates the optical transparency of a TCO. This wide bandgap enables TCOs to remain transparent across the visible portion of the electromagnetic spectrum. Their transparency is a result of their primarily ionic behaviour, which inhibits the formation of shallow donor and acceptor levels near the conduction and valence bands that could be easily ionized. For TCOs to perform effectively as transparent electrodes in optoelectronic applications, they must achieve over 80% transmittance in the visible spectrum.

In this thesis, the Haacke figure of merit (F.o.M) has been employed to evaluate and compare the performance of TCOs.[42] The Haacke equation provided below is used for calculating the figure of merit values for the TCOs throughout this study.

$$\mathrm{F.o.M} = \frac{T_l = 550(\%)}{R_{sh}}$$

1.5 Design Considerations in TCOs

The current strategy for designing Transparent Conducting Oxides (TCOs) focuses largely on heavily doping wide bandgap semiconductors to achieve desired optical and electrical properties. This ensures interband transitions take place above the visible range (> 3.25 eV), utilising the wide bandgap semiconductors. Electrical conductivity of the material is improved through maximising the dopant concentration. The overall performance of TCOs depends on optimising the electrical conductivity, carrier mobility, and scattering time, with the ratio of carrier concentration (n) to effective mass (m*) being a key factor in achieving optimal performance.

1.5.1 Band Structure

When designing Transparent Conducting Oxides (TCOs), it is essential to consider the band structure and its corresponding bandgap of the material. The electron affinity (energy difference from the conduction band minimum (CBM) and the vacuum level) plays a key role in this analysis. The electron affinity represents the energy required to add an electron and affects the dopability of the selected TCO. A higher electron affinity indicates a deeper CBM which provides ideal properties for n-type TCOs. The reason being a higher electron affinity makes it easier to introduce n-type carriers (electrons) into the system, thus enhancing dopability and conductivity. Considering these factors is crucial for optimising TCO performance.

In p-type Transparent Conducting Oxide (TCO) materials, a low ionisation potential is beneficial. The ionisation potential refers to the energy difference between the valence band minimum (VBM) and the vacuum level, representing the energy required to remove an electron from the VBM and place it in the vacuum. A lower ionisation potential indicates that the material is more conducive to hole formation, making it a suitable choice for p-type TCO applications. By having a smaller ionisation potential, the material promotes the generation of positive charge carriers (holes), enabling efficient p-type conductivity. Carefully considering the ionisation potential is key to designing effective p-type TCO materials.

Another key aspect of the band structure is the energy difference from the Fermi level in the conduction band to the next electronic energy level, known as 'CBM + 1'. It is important to ensure that the energy gap between these two levels, denoted as Eg, is greater than 3.1 eV. This is necessary to prevent electrons from being promoted to higher energy states within the conduction band, which could lead to unwanted optical absorption. This effect, called free carrier absorption (FCA), can be especially significant in thick or heavily doped TCO materials, and should be carefully considered during the design process. By managing optical absorption, TCOs can be optimised for the desired transparency and performance.

1.6 Challenges and limitations in TCOs

The most common method for developing TCOs involves degenerate doping of wide bandgap semiconductors. As mentioned earlier, this approach relies on heavy doping, which introduces defect donor levels near the conduction band. These donor levels enable the injection of extra electrons into the conduction band, boosting the material's electrical conductivity. However, it's important to recognise that excessive doping can place intrinsic limits on the conductivity of TCOs. This is because, at higher carrier concentrations (n), it becomes difficult to independently enhance both carrier concentration and carrier mobility (μ).

As a result, the carrier concentrations reached through heavy doping of wide bandgap semiconductors are capped at around $3\text{x}10^{21}$ cm^{-3} due to the solubility limit of the dopants and the occurrence of self-compensation. It is worth noting that increasing the doping concentration beyond this limit can lead to a decrease in carrier mobility, thereby limiting the enhancement of conductivity in TCOs. This threshold in carrier concentrations achieved through doping represents one of the challenges in the development of TCOs.

High dopant concentrations in TCO materials can reduce the overall scattering time, mainly due to phonon scattering at room temperature. This reduction is caused by increased ionised and impurity scattering from the high dopant concentrations used to improve conductivity in TCOs. As a result, the mobility of charge carriers becomes limited by the Coulombic interactions between electrons and dopants as they move through the material, leading to an increase in ionised and impurity scattering.

Beyond limiting conductivity, high dopant concentrations can cause dopant ions to cluster. This clustering can significantly raise the scattering rate and potentially disturb the parabolic shape of the conduction band. Therefore, when working with degenerately doped semiconductors, where the conduction bands are already filled, the effects of high dopant concentrations must be carefully considered.

1.7 Thin Film Deposition Techniques

The electrical conductivity and optical transparency of TCO materials are closely related to the film's nanostructure, coverage and particle interconnectivity and are important properties that are observed in thin film production.[53, 54] These key factors of TCO thin film can be altered and influenced by the chosen deposition technique making them dependent on the method employed. The cost of producing TCO thin films is also largely constituted by the deposition technique used as well as the cost of the materials required to produce the TCO. Therefore, it is crucial to consider the quality and cost of the film produced by each technique as this can vary largely from one technique to another.

TCO thin films can be produced by an extensive number of techniques such as sol gel process, molecular beam epitaxy (MBE)[43], pulsed lased deposition (PLD) and electron beam evaporation to name a few, each of which have their own advantages and disadvantages.[55, 56]

Thin films can be grown using a wide range of techniques and they can be categorised based on the physical and chemical processes involved in their deposition. This section presents the commonly used techniques to deposit thin films and the controllable parameters in each of them.

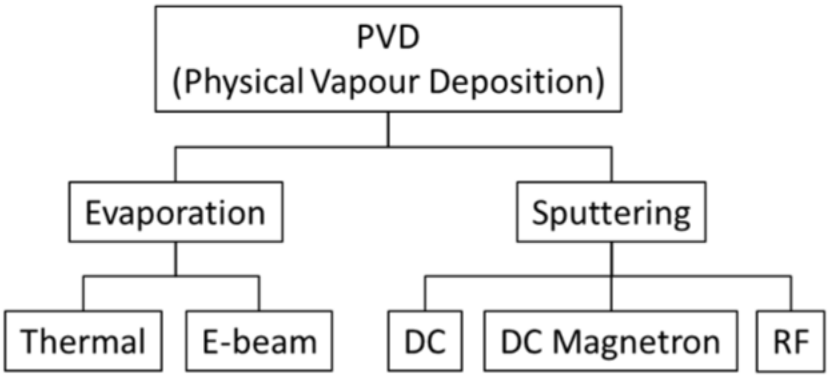

1.7.1 Physical deposition methods

Physical deposition methods usually require vacuum or low-pressure environments for thin film growth.[44,45] The process involves the transfer of the target material from a solid or gaseous phase to a substrate in a controlled atmosphere. These methods utilise physical phenomena such as evaporation, sputtering or molecular beam epitaxy to deposit thin films.

1.7.1.1 Evaporation

In evaporative deposition, the precursor used tends to be a solid material, often in the form of a wire or thin foil. The solid material is heated to a high temperature, causing the solid to enter the vapour phase. The temperature is carefully controlled to ensure the precursor vaporises without decomposing. The vapourised particles travel through the chamber before reaching the substrate, where it condenses and forms a thin film layer.

The resultant thin films grown using evaporation have high purity without contamination from the environment. As a result, there is good control over the elemental composition of the thin film which can be precisely determined by the composition of the source material. Although evaporation is a straightforward process requiring basic equipment, achieving uniform thickness and coverage over large areas can be challenging. This is due to the variation in deposition rates across the substrate. The relatively low deposition rates employed in evaporation make it more suitable for the deposition of thin films rather than thick films.

1.7.1.2 Sputtering

Sputtering involves a sputter source and a target; the bombardment of high energy ions from the sputter source to a target material causes atoms or molecules to be ejected from the surface. A thin film is made when the sputtered species ejected from the target material condenses onto the substrate. The target material used is the desired composition of the resultant thin film. Sputtering is carried out in a vacuum environment which minimises contamination from the surrounding atmosphere and can produce thin films with high purity. One limitation of sputtering in TCO production is its lower deposition rate compared to techniques like chemical vapor deposition (CVD). This slower deposition rate in sputtering can limit throughput and scalability, especially for high-volume manufacturing applications.

DC (direct current) sputtering, RF (radio frequency) sputtering, magnetron sputtering, and ion beam sputtering are all commonly used sputtering techniques to deposit thin films. The deposition of conductive materials uses a DC power supply and RF is used for insulating materials. DC magnetron sputtering is the method used to make widely used ITO thin films. In DC magnetron sputtering, a magnetic field is used near the target materials to trap electrons. This creates a plasma (partially ionised gas) in the sputter chamber which are then accelerated towards the substrate surface forming a thin film with similar composition to the target material.

Sputtering can deliver thin films across large areas of substrates at high rates with competitive costs to other deposition techniques.[66, 67] Magnetron sputtering is one of the deposition methods in practical use.[63] The lowest film resistivity achieved using this method is slightly higher than films made using PLD, on the order of 10^{-4} Ω cm.

TCO layers used in photovoltaic (PV) cells must have smooth surfaces in order to make good contact with photon-absorbing layers.[15] In this application, films deposited using DC magnetron sputtering are favourable; where thin TCO layers with low surface roughness can be coated on substrates.[68]

High deposition rates, uniform film thickness over large substrate areas, and high-quality deposition of ITO thin films with desirable electrical and optical properties enables the efficient and cost-effective deposition of ITO films using DC magnetron sputtering.[46] DC magnetron sputtering is a well-established technique to deposit conductive thin films like ITO for use in touchscreens, solar cells, displays and optoelectronic devices.

1.7.1.3 Molecular beam epitaxy (MBE)

Molecular beam epitaxy (MBE)[43] is another physical deposition technique used to grow complex thin films with precise control over film thickness and composition. MBE is particularly used to make advanced semiconductor materials which require precise control over thin film growth to produce high quality thin films. One drawback of using Molecular Beam Epitaxy (MBE) for Transparent Conductive Oxide (TCO) production is its difficulty in depositing intricate multicomponent films. While MBE excels at growing epitaxial layers with precise control over thickness and composition, it may struggle to achieve the complexity and uniformity required for certain TCOs, especially those with complex compositions or doping profiles.

MBE uses an ultra-high vacuum (UHV) chamber to minimise contamination and ensure a clean environment for thin film growth. The layer-by-layer growth of films in MBE allows precise control over film thickness and interfaces producing thin films of superior quality and performance, important in the production semiconductor materials. Defect free thin films can be produced using this method making it a powerful tool in the manufacture of high-performance semiconductors.

1.7.1.4 Pulsed laser deposition (PLD)

Pulsed laser deposition (PLD) is a physical deposition method that uses a high energy laser to ablate a target material. When the target material is ablated, it undergoes a phase change from solid to gas forming a plasma plume. The species in the plume are directed towards the substrate where it condenses and forms a thin film.

PLD is compatible with a wide range of materials, particularly materials with high melting points or low solubility. Its ability to transfer stoichiometry accurately from the target material to deposit complex thin films makes it commonly used in the research and development of advanced thin film devices and functional coatings.

Among all deposition techniques, pulsed laser deposition encompasses the most control in the morphology and composition of the thin films produced.[63] Park *et al* and Agura *et al produced* thin films of Ga doped ZnO (GZO) and Al doped ZnO (ADO) with low resistivities in the order of 10^{-5} Ω cm using PLD, respectively.[64, 65] This is the best resistivity measurements of ZnO thin films to be reported. Thin films grown via PLD exhibit better conductivities than films obtained from other deposition techniques.[63] However, issues with the stabilities of films and cost of processing prevent PLD being used for large scale fabrication of thin films.

1.7.2 Inkjet printing

Inkjet printing offers a cheap, alternative film deposition method for patterned TCOs. This technique can be scaled for industrial production with high throughput deposition rates.[70] Inkjet printing minimises precursor wastage, reducing the overall cost of film production making this technique favourable from an economic perspective.[71]

The surface roughness of thin TCO films fabricated using inkjet printing can be high, a drawback of using this technique. For instance, smooth surface TCO thin films with a low surface roughness are needed, for use in photovoltaic cells at the heterojunction, to make good contact between layers.[15] TCO thin films printed via the inkjet technique would be unsuitable in this scenario as the surface roughness of the film would be high causing poor contact at the heterojunction.[15]. This demonstrates the importance of taking into consideration the purpose of the TCO and the properties required of the thin film for that application.

1.7.3 Chemical deposition methods

Chemical deposition methods involve chemical reactions between precursor compounds and the substrate surface to deposit target materials onto the substrate and form a thin film. This section summarises the two categories of chemical deposition methods: wet chemical deposition and vapour-phase chemical deposition.

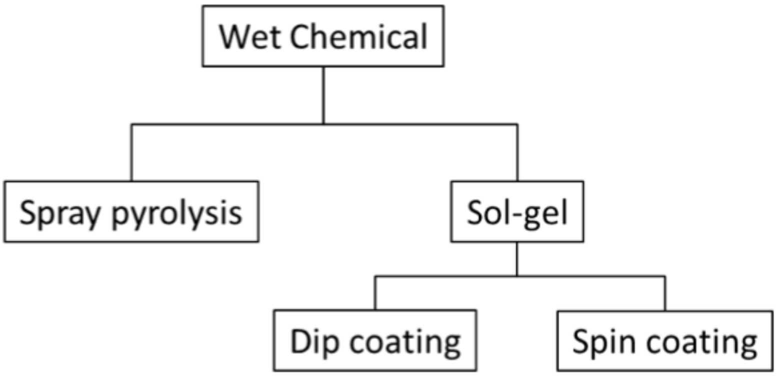

1.7.3.1 Wet chemical deposition

This category involves the use of liquid-phase chemical reactions; where the target material is dispersed in liquid by reacting the precursors and depositing onto substrates to form thin films. Spray pyrolysis and sol-gel are the two common wet chemical deposition methods used to make thin films.[47,48]

Spray pyrolysis

Spray pyrolysis, also known as spray deposition or aerosol deposition, is a wet chemical technique used for the deposition of thin films onto a substrate surface. It involves the formation of a fine mist or aerosol of the precursor solution, which is sprayed onto a heated substrate. Upon contact with the heated substrate, the precursor droplets undergo pyrolysis, where the solvent evaporates, and the precursor material decomposes to form the desired thin film. The precursor solution typically contains the target material in a solvent.

In this method, the selected precursor solution must produce by-products that are volatile at the deposition temperature of the thin film.[47].The crystallinity and morphology of the resultant thin film is strongly influenced by the precursor materials chosen for this method of deposition.[49] Achieving precise control over film thickness and uniformity, particularly over large areas may be difficult as the method involves spraying precursor solutions onto a heated substrate, which can lead to variations in film thickness and uniformity.

The simplicity and scalability of this method and the ability to deposit films over large substrate areas makes this a widely used technique to deposit thin films. Thin films grown using spray pyrolysis are used in a wide range of applications such as solar cells, gas sensors and catalysts.

Sol-gel

Sol-gel is a versatile chemical deposition method to produce thin films. Thin films are made by reacting precursors to form a colloidal suspension of precursors known as the “sol”. The sol transforms into a gel through hydrolysis and condensation which is then deposited as a thin film on the substrate.[48]

Sol gel is an attractive film deposition due its advantageous ease of film composition control and fabrication of large thin films at low cost. High purity, homogeneous films of indium doped zinc oxide have been achieved on large glass substrates using the sol gel process at low temperatures.[61] Luo *et al* produced thin films with resistivities of 2.35×10^{-2} Ω cm using microwave assisted non aqueous sol gel in combination with dip coating.[62] These are promising results in the development of versatile film deposition processes using liquid-phase routes.

In order to produce good quality TCO films using sol gel all stages of the process need to be optimised. This includes preparation of the solution, aging of the sol to form nanoparticles, thin film coating and post deposition annealing; all of which needs to be enhanced to achieve high standard films using the sol gel method.[63] Sol-gel techniques in TCO production can struggle to maintain uniformity and precise control over film thickness. Factors like solution consistency, drying conditions, and substrate interactions can impact the final film's quality. Ensuring consistent properties across large areas may be harder compared to methods like sputtering or chemical vapor deposition (CVD).

Dip-coating

Dip coating is a common technique used in sol-gel to deposit thin films onto substrates. This wet chemical technique allows deposition on flexible substrates such as polypropylene adipate (PPA) which is of significant interest due to the demand for transparent flexible conductive materials.[57] Indium doped zinc oxide thin films for transparent electrode applications have been successfully made on a nanoscale using this method.[58] Large surface coverage, low temperature deposition and evaporation makes dip coating favourable over other deposition techniques.[59]

Spin coating

Spin coating is another widely used technique in sol-gel to deposit thin films. Unlike dip coating the substrate is not immersed into the sol solution instead the precursor solution is dropped onto the centre of the substrate surface. The substrate is mounted on to a spin coater which rotates at high speeds. As the substrate spins, the solution spreads across the substrate and the solvent in the sol evaporates leaving behind a thin film. Once the film has dried the process can be repeated to make multi-layered thin films. The thickness of the thin films is controlled by the size of the precursor droplet and the speed of the rotation of the substrate. Similar to sol-gel and dip coating, using spin coating it is difficult to achieve even thickness across large areas and it is not suitable on complex surfaces where the substrate is non-flat.

1.7.4 Chemical Vapour Deposition (CVD)

Vapour-phase deposition or more commonly known as chemical vapour deposition (CVD) is a widely used deposition technique to make thin films of high purity and quality for semiconductor applications. Chemical vapour deposition generally involves the chemical reaction in the vapour phase or on the surface of substrates to form thin films. In this method the precursors need to be volatile and thermally stable transition into the gas phase. The vapourised precursor and solvent molecules are transported to the glass substrate, where energy is provided to facilitate chemical reactions, leading to the growth of a thin film on the substrate. In general, vapourised precursor molecules are transported using a carrier gas.[50] During the transport of vapourised precursor molecules, they encounter different forces from this movement to the substrate, which is later described by fluid dynamics.

The energy required for chemical reactions to take place can come from three different sources and dictates the different branches of CVD: thermal, photon and plasma. In this thesis thermally activated chemical vapour deposition was employed to deposit thin films and will be described in detail below.

The key stages of CVD described above have been illustrated in the diagram below:

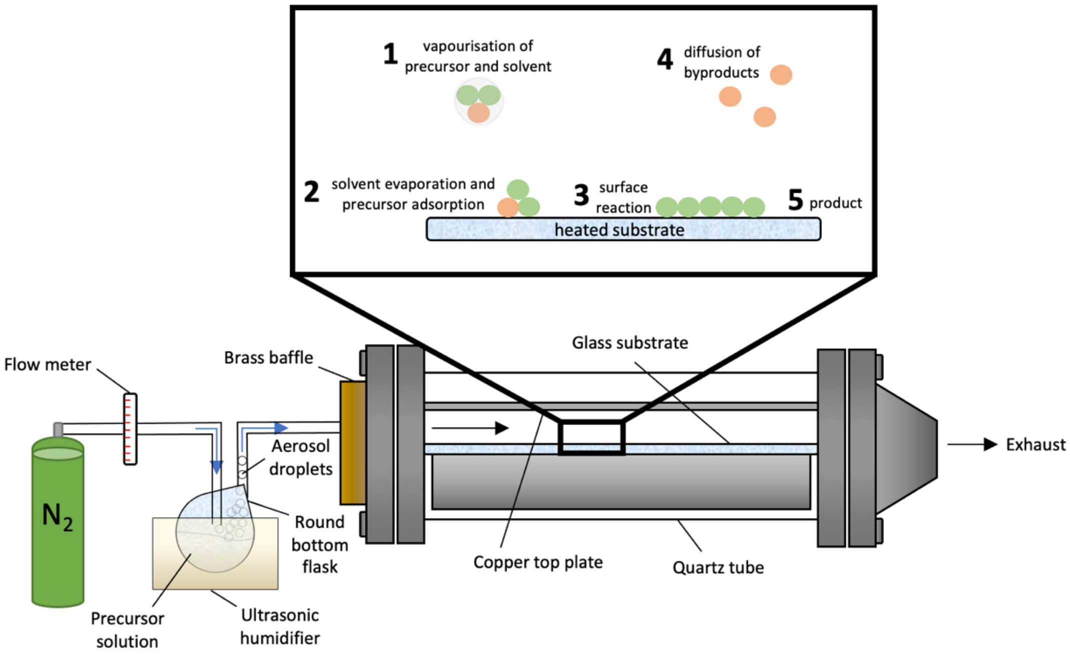

Figure 1.10 – Schematic representation of the AACVD set up showing the key steps involved in the AACVD process

The key steps involved in chemical vapour deposition are described below:

1. Precursor delivery: The precursor, in gaseous form, is transported to the heated substrate either directly or with the aid of an inert carrier gas.[51,52]
2. Adsorption and decomposition: The solvent evaporates, and the precursor undergoes a heterogeneous reaction. The precursor decomposes on the heated substrate and is adsorbed onto the surface. The adsorption of precursor molecules on the hot substrate is known as a physisorption process.
3. Surface diffusion: The heated substrate provides the adsorbed precursor molecules with energy, causing surface diffusion across the substrate. The precursor molecules rearrange until they reach a strong binding site (lowest energy vacant site). This is called chemisorption.
4. Nucleation and film growth: The reaction of precursor molecules on the substrate surface results in thin film growth. The growth process can occur via several mechanism, described later.
5. Desorption: Unwanted organic chemicals (by-products) are desorbed from the surface of the substrate and transported away through the exhaust.

1.7.4.1 Variations of chemical vapour deposition (CVD)

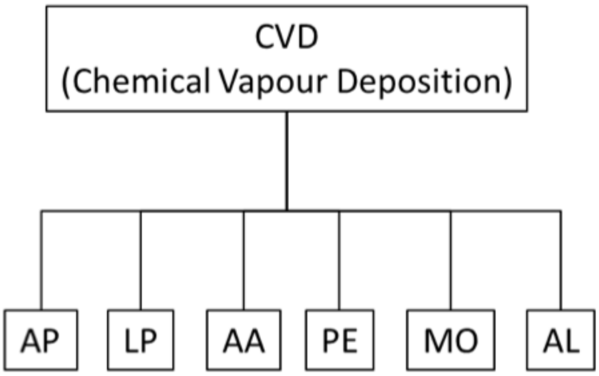

There are many distinct types of chemical vapour deposition methods utilised to grow thin films. Each method uses different gas sources and deposition conditions (pressure and temperature) which can result in varying films for the same target material, depending on the method used. Therefore, it is important to understand the effects of deposition conditions on film growth and the limitations of each method when selecting a CVD route for thin film production. Some of the commonly used CVD routes for thin film production are discussed below:

- APCVD (Atmospheric Pressure Chemical Vapour Deposition)

  APCVD is a CVD technique that operates under atmospheric pressure and uses thermal energy to activate chemical reactions. It is a widely used deposition technique in industry due to the feasible scalability of the technique and fast production of thin films on a large scale. Resultant thin films exhibit good uniformity, durability and adhesivity to the substrate. This method requires precursors to be volatile as it involves the vaporisation precursor molecules in bubblers which can limit the number of precursors available to use to deposit target thin films. The deposition rate in APCVD depends on the diffusion of gaseous precursor molecules to the surface of the substate. In this method the surface reactions are limited by diffusion of the precursors and variations in gas flow rates can lead to non-uniform thin films.

- LPCVD (Low Pressure Chemical Vapour Deposition)

  LPCVD is another thermally activated CVD route to thin films which requires reduced pressures to deposit thin films. Like APCVD, this method also requires precursors to be volatile, narrowing the use of available precursors. Unlike APCVD, LPCVD is not limited by the diffusion rates of precursors as the pressure gradient increases the flow rate of precursors within the chamber. Therefore, the rate of surface reactions is primarily governed by the temperature and the availability of sites for the reactions to occur. Consequently, resultant thin films deposited using LPCVD have improved uniformity and better coverage across the substrate. One limitation of LPCVD is its limited scalability for large-area deposition. LPCVD processes are typically conducted in batch reactors or small-scale systems, which may restrict the size of the substrates that can be coated and hinder the application of LPCVD in manufacturing processes.

- UHCVD (Ultra High Vacuum Chemical Vapour Deposition)

  UHCVD utilises a high vacuum environment in the deposition of thin films where low pressures such as $<10^{-6}$ Pa are needed. The deposition of thin films in UHCVD also occurs through the activation of precursor molecules by thermal energy. UHCVD enables the deposition of thin films with high purity and minimises contamination due to the ultra-high vacuum conditions employed. Film properties can be fine-tuned as

UHCVD allows precise control over deposition parameters enabling thin films with complex structures to be produced. Due to the high vacuum environment the range of substrates that can be used to deposit thin films is limited as substrates need to be able to withstand high vacuum conditions. UHCVD requires complex and expensive equipment to provide high vacuum conditions for thin film growth.

- PECVD (Plasma Enhanced Chemical Vapour Deposition

PECVD generates a low-pressure plasma by applying an electric field to a precursor gas which forms reactive species such as ions and radicals. These reactive species interact with precursor gas, resulting in the growth of thin films on the substrate. The formation of reactive ions and radicals allows reactions to take place at lower activation energies. This enables deposition of thin films at relatively low deposition temperatures compared to the techniques described above. Low temperature deposition in PECVD makes this technique versatile and allows a wider range of materials to be used. Unlike other high temperature depositions in other CVD methods, the substrates and components are not damaged by high temperatures employed. However, this method is susceptible to impurities introduced by the plasma generated leading to film contamination and compromise of film stoichiometry and quality. PECVD requires complex and specialised equipment to generate and control the plasma making this a more expensive method to deposit thin films.

- PICVD (Photon-induced Chemical Vapour Deposition)

PICVD harnesses the power of photons to induce chemical reactions required to form thin films on substrates. Photons, typically UV light is used in PICVD to irradiate precursor gases in the reaction chamber as they enter. This triggers photochemical reactions which form thin films on the substrate. The use of photons in PICVD promotes cleaner and controlled chemical reactions which can produce highly controlled patterns or localised coating areas producing thin films with reduced impurity. The lower deposition temperatures employed in this method enables the use of temperature sensitive substrates which can be advantageous and cost effective when compared to thermally activated CVD methods. A limitation of PICVD is its reliance on specific light sources like lasers or UV lamps. Obtaining and maintaining these sources can be costly, and controlling light parameters adds complexity to the process limiting its widespread use.

- ALCVD or ALD (Atomic Layer Chemical Vapour Deposition)

Atomic layer CVD also known as atomic layer deposition (ALD) or atomic layer epitaxy (ALE) is a specialised deposition technique used to grow thin films with precise thickness and composition. Atomic layer deposition is achieved by alternating pulses of precursor gases and purging with inert gas to control film formation. The transportation of pulses of precursors to the substrate limits further reactions and results in the deposition of individual atomic layers at a time. This technique utilises the alternating self-limiting surface reaction (half reactions) to deposit ultra-thin films with high uniformity and accuracy. This method produces thin films on complex 3D structures with conformal coating capabilities making this advantageous in advanced applications such as coating nanowires, nanoparticles and high-aspect-ratio structures. ALCVD has a relatively slower deposition rate due to the deposition of one atomic layer at a time. This CVD technique requires advanced equipment and complex parameter controls; such as controlled pulsing of precursors, precise gas handling for purging and controlled temperature conditions to precise atomic layer by layer deposition.

- AACVD (Aerosol Assisted Chemical Vapour Deposition)

Aerosol assisted chemical vapour deposition (AACVD) is a more recent low-cost CVD method that has gained interest due to not requiring highly volatile precursors. This method does not rely on the evaporation of precursors in a carrier gas instead a solution of the precursors is aerosolised which is then transported to be deposited on to the substrate by a carrier gas. AACVD allows for the use of a broader range of precursors, as they do not need to be volatile. The only requirement is that the precursor must be soluble in the solvent, enabling the formation of an aerosol mist containing the precursor.

Although a wider range of precursors can be used in AACVD, this technique has a slower deposition rate and involves multiple steps including aerosol generation, transport, and deposition. Transporting aerosols over long distances is difficult in AACVD and as a result limits its scalability and throughput in industrial settings.

1.7.5 Aerosol Assisted Chemical Vapour Deposition

1.7.5.1 Precursor requirements

In AACVD deposition, precursors need to decompose cleanly to ensure by-products or ligands are not left behind to avoid thin film contamination. As such, precursors used in AACVD need to be designed such that by-products are volatile and lost into gas phase when the precursor decomposes leaving behind the thin film of interest on the substrate.

In order to obtain thin films with high purity and desired composition, precursors can be studied using Fourier transform infrared spectroscopy (FT-IR), gas chromatography mass spectroscopy (GC-MS) and thermogravimetric analysis (TGA). These characterisation techniques can be used to better understand the precursor decomposition path and predict how it would behave in AACVD. When choosing a precursor for AACVD deposition for a target material the following needs to be considered:

Purity of precursor: This is one of the most important considerations when selecting a suitable precursor for AACVD deposition. In order to produce thin films with high purity, the precursor decomposition path needs to be clean to reduce unwanted impurities which can be related to the precursors molecular structure.

Reactivity of precursor: The precursor needs to undergo chemical reactions on the surface of the substrate for film growth to take place; the precursor should not be highly reactive and begin reacting in the vapour phase before film deposition. This will lead to no film growth and instead a powdery residue on the glass.

Solubility in solvent: In CVD most precursors are required to be volatile, AACVD is an exception and requires the precursor used to be soluble in the chosen solvent.

Stability in air: Precursors that are stable in air do not require to be handled in glove boxes or other specialised equipment making it easier to handle and use for AACVD depositions.

Hazard risk: Precursors with low toxicity and non-hazardous by-products are advantageous, to prevent the requirement of additional specialised equipment for deposition, storage or removal of hazardous by-products.

Cost and scale up: In order to produce economically viable thin films, the synthetic steps and waste products needs to be kept to a minimum. For industrial applications, precursors need to be scaled up easily to produce thin films with high purity keeping costs low.

The first chapter of this thesis investigates the decomposition path of Zn precursors and the resultant properties of thin films. The decomposition of a precursor is related to the molecular structure of the precursor. This chapter studies the effect of molecular structure of the precursor used on the morphology and electronic properties of the films.

1.8 Thin film growth

Thin film growth takes place when the precursor molecules undergo a heterogeneous reaction upon contact with the heated substrate, glass is the substrate used for the films produced in this thesis. This reaction involves the thermal decomposition of the precursor and subsequent absorption onto the glass. The deposition conditions, surface diffusion of precursor molecules and nucleation during deposition determine the type of film produced. Thin film growth via CVD can be categorised as: epitaxial growth (single layer or single crystalline), polycrystalline growth or amorphous.[50]

Epitaxial growth is the growth of single layer crystalline films that have similar lattice spacings to the substrate. For epitaxial growth to take place the lattice mismatch between the substrate and film needs to be minimised. High lattice mismatch between the film and substrate will result in defects like dislocations, which can reduce the adhesivity and stability of the film. Epitaxial films can be subdivided into homoepitaxy and heteroepitaxy; homoepitaxy is when the film and substrate are of the same material, heteroepitaxy is when the film and substrate are of a different material. Epitaxial growth is typically achieved at high temperatures and low growth rates, which facilitate faster surface diffusion on the substrate. These growth conditions provide the atoms with sufficient time to arrange in a layer-by-layer structure, as the surface energy for the crystal orientation is lower than that of other orientations. Epitaxial growth of thin films with single crystalline layer is favoured in superconductor and semiconductor applications such as TCO thin films.[53]

Chapter 2 explores the use of seeding layers to promote epitaxial growth in thin films, without the need for high temperatures, which is advantageous in TCO thin film production.

Amorphous growth, in contrast, takes place at low temperatures and high growth rates resulting in a high number of adsorbed atoms on the surface, also referred to as adatoms. The high concentration of adatoms with low mobility inhibits nucleation (surface diffusion), preventing the formation of a crystalline film on the substrate. Amorphous thin films have a disordered structure with a random arrangement of atoms or molecules. The amorphous nature of the films, along with the absence of grain boundaries, makes them ideal for use in transistor applications.

Polycrystalline growth is the growth of multiple individual crystalline grains, across different sites on the surface of the substrate. These crystalline grains are sometimes referred to as ‘islands’. The expansion and enlargement of the different crystalline grains ‘islands’ on the substrate coalesce to form a polycrystalline thin film. Unlike epitaxial growth, polycrystalline growth can take place on any type of substrate and are not affected by lattice mismatch of the material and substrate. Thus, this type of growth typically takes place when the atoms on the surface interact strong with each other as opposed to the substrate. Polycrystalline growth occurs at intermediate temperatures and growth rates, which are between those used for epitaxial and amorphous thin films. The level of crystallinity in the films is affected by the deposition temperature. Polycrystalline thin films are used in renewable technologies such as thin film solar cells.

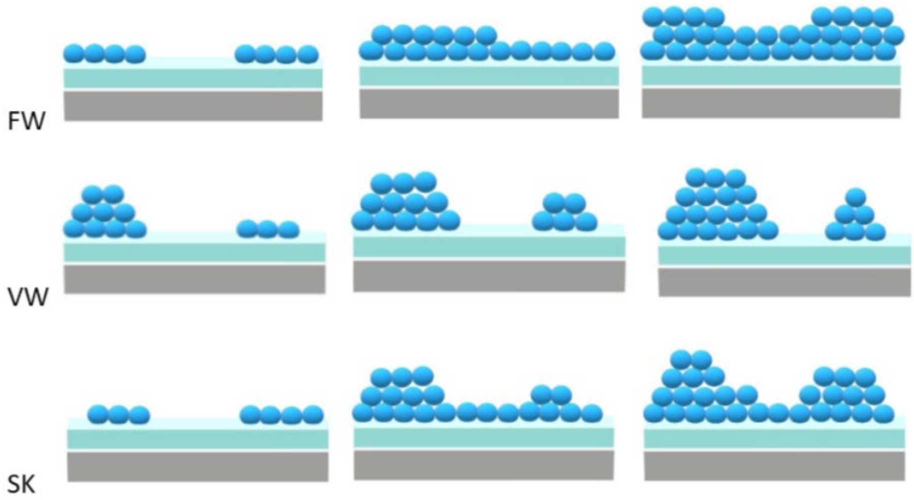

Figure 1.11 - Schematic showing the different types of film growth

Frank van der Merwe (layer by layer), Volmer Webber (island growth) and Stranski-Krastanov are three primary growth modes used to describes the different types of growths and morphologies observed in thin films grown using CVD.

In Frank van der Merwe (FV) growth layer by layer growth of the thin film is seen where the adatoms (adsorbed atoms) are strongly bounded with the substrate than each other. This results in fast nucleation (surface diffusion) of each layer promoting 2D growth. The layer-by-layer growth produces conformal and smooth thin films which are advantageous in semiconductor applications. The Frank van der Merwe growth mode tends to produce thin films with a higher degree of crystallinity.

In Volmer Webber (VW) island growth takes place, unlike Frank van der Merwe, adatom to adatom interactions are stronger than adatom to substrate interactions. This leads to the formation of individual islands or clusters of material on the surface of the substrate resulting in 3D growth. As deposition continues the islands grow and merge grow continuous thin films. This type of growth mode typically gives rise to polycrystalline thin films with rougher and more textured film surfaces.

Stranski-Krastanov (SK), also referred to as the layer-plus-island growth mode, incorporates elements of both layer-by-layer (FV) and island growth (VW). In this mode, growth begins with layer-by-layer formation, followed by island growth on top. The islands then grow and eventually merge to form a thin film. SK growth mode results in more uniform thin films compared with films grown via VW growth mode.

The growth mode observed in thin film deposition is determined by several factors, including the substrate material, deposition technique, growth conditions, and interactions between the film and substrate. Controlling the growth mode is key for achieving desired thin film properties and optimising the performance of thin film-based devices and applications.

1.9 Fluid dynamics of CVD

The transport process of the precursor gas (along with the carrier gas) within the reaction chamber can be characterised using principles from fluid mechanics. In fluid mechanics, the nature of the gas flow in the reactor can be described by the dimensionless parameter, Reynolds (R_e) number. It is the ratio of inertial forces to viscous forces and highlights the relative dominance of the two forces.[54] The magnitude of the Reynolds number can be used to classify the flow regime as either laminar, transitional or turbulent.[55]

A low Reynolds (Re) number below 2300 results in laminar flow where viscous forces are dominant and the gas flows in distinct parallel layers with no mixing of layers or disruption to flow.[54] If Re exceeds 4000, turbulent flow occurs where the gas experiences irregular changes in velocity and direction, resulting in slower movement through the reactor and could lead to the precursor being trapped which is undesirable for film growth.[55] Transitional flow, which is a combination of turbulent and laminar flow, occurs when the Reynolds number lies between 2300 and 4000.

The Reynolds number is defined as shown in the equation below:

$$R_e = \frac{\rho u L}{\mu}$$

In the given equations, where ρ represents the gas density, u denotes the flow density, L indicates the distance from the gas inlet, and μ represents the gas viscosity.

In most CVD reactors the Re number is low, indicating laminar flow, due to the low precursor flow rate. [56,57] The velocity of the gas at the surface of the substrate within the CVD chamber is zero. The boundary layer is known as the region between substrate surface (where the gas volume velocity is zero) to where the gas volume has a velocity.[54] As such the precursor gases in motion must diffuse into the boundary layer and adhere to the surface of the substrate for CVD to occur.[58]

1.10 Thermodynamics and kinetics of CVD

Chemical vapor deposition (CVD) is a non-equilibrium process. During CVD, the continuous supply of the gaseous precursor (reactants) in the system increases the number of reactants and disrupts the equilibrium. As the reaction continues, the film (solid product) is deposited on the substrate, removing reactants from the gas phase and driving the system towards film deposition.

The feasibility of a chemical reaction is assessed by calculating and comparing the Gibbs free energy of each product and reactant.[59] A more negative change in Gibbs free energy indicates a stronger tendency for thin film formation.[54] As a result, thermodynamics is both key in determining whether deposition occurs and the maximum rate of deposition.

Another key consideration is the activation energy which is the kinetic barrier that must be overcome for a reaction to occur. There needs to be sufficient energy to surpass this barrier for exothermic reactions to take place. The kinetics of CVD are governed by the mass transport of the precursors to the substrate.[54] The rate of deposition is restricted by the slowest step in the CVD process known as the rate-determining step.

The growth rate of thin films can be examined as a function of substrate temperature, as shown in Figure 1.12. Depending on the temperature. there are three factors that can influence the rate-determining step:

1. Surface reaction is the rate-determining step at low growth temperatures.[54] The surface reaction is strongly dependent on the substrate temperature and at low temperatures, the reaction takes place slowly. As such, increasing the temperature will accelerate the deposition rate.

2. Once the substrate temperature increases to a certain point, the deposition rate is no longer controlled by the temperature but by the mass transport of precursors through the boundary layer. As a result, the partial pressure of precursors above the boundary layer becomes the key factor and this stage is known as mass transport limited.[55]
3. As the temperature continues to rise to higher temperatures, there is a decrease in the deposition rate.[55] This is because at such high temperatures, reactions in the gas phase become dominant, causing the precursors to fully decompose into unwanted solid particles rather than the intended film. The substrate is usually hottest region in the reaction chamber, as such the particles tend to move further from the

substrate. This is known as thermophoresis and reduces the growth rate and in turn film thickness.[58]

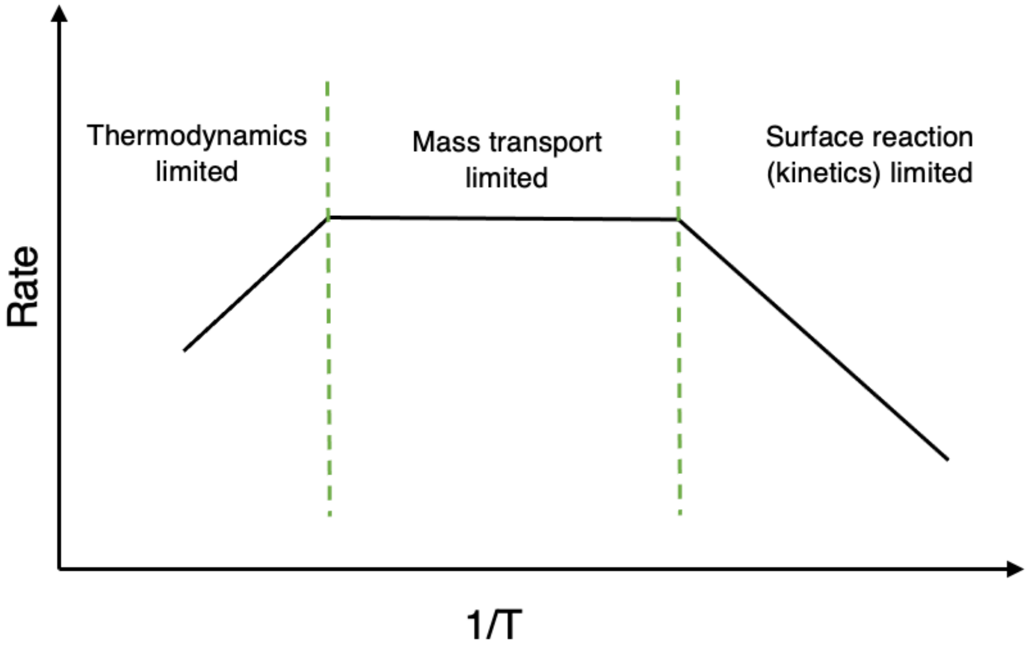

Figure 1.13 - Growth rate of CVD films as a function of temperature

1.11 Aerosol-assisted CVD

AACVD uses an aerosol mist to transport precursors to the reaction chamber, enabling the use of previously impractical solid and liquid precursors with low volatility. This capability is advantageous as it allows for the use of a wider range of precursors that were incompatible due to their limited volatility. In the case of solid precursors, the only requirement is their solubility in a suitable solvent and the ability of either the precursors themselves or their decomposition products to exist in the vapor phase.

Furthermore, the cost of producing high-quality thin films for devices using AACVD can often be lower than traditional CVD methods due to reduced concerns regarding volatility and thermal stability of the precursors.

To generate the aerosol mist in AACVD, various methods can be employed, including ultrasonic atomisers, pneumatic sprayers, or electrostatic atomisers. Ultrasonic aerosol generation, a widely used technique, relies on a piezoelectric transducer. When an electric field is applied, the transducer vibrates at a high frequency, producing ultrasonic waves that create fine droplets by disrupting the precursor solution

The size of these droplets can be determined using Lang's equation, which provides a relationship between the droplet size and the properties of the precursor solution, such as its surface tension and viscosity.[44]

$$d = 0.34\left(\frac{2\pi y}{\rho f^2}\right)^{\frac{1}{3}}$$

The diameter (d) of the droplets formed during AACVD is influenced by factors such as the excitation frequency (f), the density (ρ), and the surface tension (γ) of the liquid or solution. The equation shows that increasing the ultrasonic vibration frequency decreases droplet size. Smaller droplets are generally advantageous for film deposition as they promote efficient solvent evaporation and precursor vaporisation, both crucial for CVD. Therefore smaller droplet sizes can lead to better quality thin films.

Aerosol droplets are generated by a 20 kHz piezoelectric transducer and transported into the CVD reactor using an inert carrier gas (nitrogen or argon).

Inside the reactor, the solvent in the droplets evaporate, reducing their size, followed by vaporisation of the precursors and formation of the thin film.

Aerosol-assisted CVD is a effective method for depositing ZnO thin films, as both single-source precursors and dual-source precursors can be used. One notable advantage of AACVD is that it operates without the requirement for ultra-high vacuums, leading to lower operational costs.

Chapter 2 – Experimental and characterisation methods

The first section of this chapter will outline the various AACVD setups used to deposit the ZnO thin films discussed in later results chapters. The subsequent sections will detail the analytical techniques employed for materials characterisation.

2.1 Preparation

2.1.1 Glass substrates

Glass provided by NSG Pilkington is used as the substrate for thin film deposition via AACVD. Firstly, a UV beam is used to identify the side of the glass with the silica coating. A score is made on the back of the glass substrate (uncoated side) to easily distinguish between the coated and uncoated sides. The large glass panel is measured and cut into smaller substrates measuring (50 x 145 x 4mm) so that they can fit into the reactor. The substrates are cleaned with detergent and rinsed, followed by further cleaning with acetone and isopropanol before being placed in an oven to remove any excess solvent on the surface. After drying in the over, the glass is sprayed with isopropanol once again and Nitrogen gas is used to remove the solvent and any remaining debris. The glass substrate is then clean and ready for deposition.

2.2 Aerosol assisted chemical vapour deposition (AACVD)

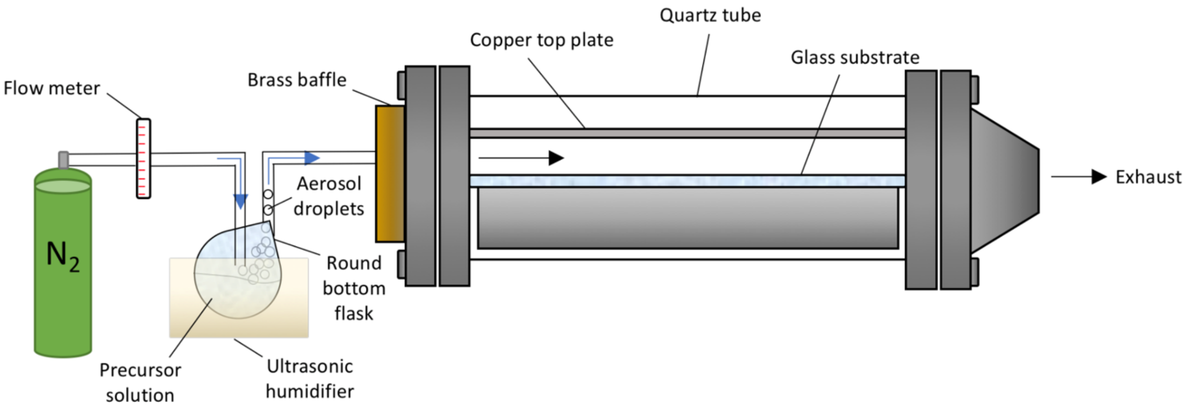

Figure 2.1 - Diagram of single source AACVD set up

Aerosol assisted chemical vapour deposition (AACVD) is set up as illustrated above in Figure 2.1. The glass substrate is inspected to ensure it is clean and then positioned on top of the reactor's heating block ensuring the silica coated side is facing upwards (scored side facing down). The copper top plate is then carefully placed about 8 mm above the substrate into the holder. The top plate helps ensure the N_2 carrier gas has a laminar flow above the substrate throughout the deposition process.

The temperature of the heating block is controlled by a Whatman cartridge heater. The reactor is screwed closed, and the controller is activated to heat up the block at a rate of 15°C/min until the deposition temperature is reached. A safety function is always used to automatically turn off the reactor if the temperature exceeds the limit set, typically 10 degrees higher than the desired deposition temperature.

Whilst the reactor heats up, a round bottom flask is securely clamped inside the piezoelectric ultrasonic humidifier. The humidifier is filled halfway with deionised water, followed by adding the precursor solution into the round bottom flask. The flask has 2 joints, one of which is connected to the carrier gas and the other is linked to the brass baffle connecting it to the reactor. The purpose of the baffle is to create a uniform flow of the aerosol into the reactor. Nitrogen, an inert carrier gas, is pumped into the reactor for at least 15 minutes to ensure a stable environment prior to deposition.

When the reactor reaches and remains stable at the deposition temperature, the humidifier is switched on transforming the precursor into an aerosol. The precursor aerosol is transported into the reactor at a controlled flow rate via the carrier gas. The precursor then undergoes thermal decomposition on the substrate, resulting in film growth.

Once all the precursor solution has been aerosolised and no precursor solution or mist is visible in the round bottom flask, the deposition has ended. The heater is then turned off and allowed to cool down to room temperature while the N_2 carrier gas continues to flow. When the substrate reaches 100°C, the carrier gas supply is turned off and the reactor is left to cool to room temperature. Once cooled down, the substrate is taken out and inspected for film formation. The substrate is then cut into the necessary sizes ready for material characterisation.

2.3 Characterisation Methods

The following section provides a summary of the characterisation methods used to analyse the thin films produced in this thesis. Where necessary background information and theory of the analysis method has been discussed. A range of characterisation techniques have been used to determine the properties of the films. The structural characterisation of the thin films has been carried out using X-ray Diffraction (XRD), Scanning Electron Microscopy (SEM) and X-ray photoelectron Spectroscopy (XPS). Optical and electronic properties of the thin films have been assessed using UV-Vis and Halls Effect measurements to determine the TCO merit of the films.

2.3.1 X-ray diffraction (XRD)

X-ray diffraction analysis is usually the first characterisation conducted on the thin film, as the sample can be placed directly into the XRD machine without the need for cutting. Hence XRD is a non-destructive characterisation method and does not damage the sample. X-ray diffraction (XRD) provides valuable information such as phase identification, crystallinity, crystallite size and preferred orientation.[60,61] These parameters can be determined through analysing the XRD pattern of the thin film as described below.

2.3.1.1 Miller planes

The arrangement of atoms in a material's crystal structure is defined by its long-range order at the atomic level. This order manifests as periodic atomic planes, referred to as Miller planes, which arise from the repeated replication of the unit cell in three dimensions. The Miller planes are identified by their corresponding Miller indices and are represented by three integers enclosed in parentheses (hkl). The Miller indices (hkl) correspond to the reciprocals of the intercepts of the plane with the axes and the equation used to determine Miller indices for cubic crystal structures is:

$$(hkl) = \left(\frac{1}{a}, \frac{1}{b}, \frac{1}{c}\right)$$

The a, b and c are the lengths of the lattice parameters along the x, y, and z directions, respectively.

In cubic crystal structures with a lattice parameter of a, the interplanar spacing for a specific Miller plane (hkl) can be calculated using the following equation:

$$d_{hkl} = \frac{a}{\sqrt{h^2 + k^2 + l^2}}$$

When a crystal structure is exposed to incident radiation and scanned at different angles, distinct Miller planes within the crystal lattice induce diffraction phenomena. Each crystal structure possesses its own unique set of Miller planes, resulting in a characteristic X-ray diffraction (XRD) pattern, often referred to as a "fingerprint," for that particular crystal structure.

2.3.1.2 *Bragg's Law*

The interplanar distance, d_{hkl}, in a crystal structure is typically in the range of 10^{-10} meters, which is comparable to the wavelength of X-ray radiation.[8] This property makes X-rays well-suited for investigating the crystal structure of materials. When a beam of X-rays is directed onto the surface of a material at an angle θ, the photons interact with the electron clouds surrounding the atoms. At specific angles, constructive interference occurs between the reflected photons originating from different crystal planes, leading to the formation of high-intensity peaks. This phenomenon is governed by the Bragg equation:

$$n\lambda = 2d_{hkl}\sin\theta$$

In the context of Bragg's law, the equation can be expressed as follows, where n represents the order of the reflection (typically set to 1), and λ denotes the wavelength of the incident photon. The underlying principles of Bragg's law are illustrated in the accompanying figure below.

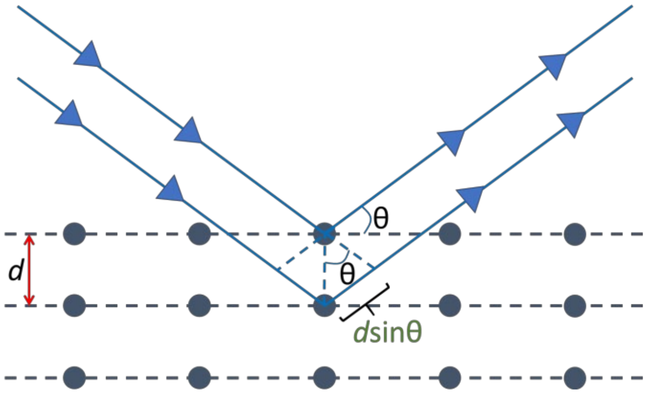

Figure 2.2 - Diagram illustrating Bragg's law

2.3.1.3 *Crystallite size*

Within a polycrystalline material, such as the films discussed in this thesis, the quality of the crystals can be assessed by analysing the diameter of the crystallites. Generally, a larger crystallite size indicates a higher degree of crystallinity. The determination of the crystallite diameter can be achieved by examining the broadening of peaks observed in an X-ray diffraction (XRD) pattern. This analysis utilises the Scherrer equation:

$$d = \frac{k\,\lambda}{\Delta\,(2\theta)\cos\theta}$$

The average diameter of the crystallites, denoted as d, can be calculated using the Scherrer equation, where k is the Scherrer constant typically set to 0.9.[8,61,62] The equation involves the wavelength of the incident radiation, λ, the full width at half maximum in radians denoted as Δ(2θ), and the Bragg diffraction angle represented as θ.

Although using a value of 0.9 for the Scherrer constant is an empirical approximation assuming spherical crystallites, it serves as a widely accepted value in literature and is common practice in X-ray diffraction (XRD) analysis despite variations in crystallite shape.[63] The absence of alternative techniques such as transmission electron microscopy (TEM) necessitates a default value which provides a starting point for estimating crystallite sizes in ZnO materials. Therefore it is important to note that this leads to a considerable error in the calculation of crystallite dimensions using the Scherrer equation.

2.3.1.4 Texture coefficient

In the context of thin films and other deposition processes, preferred orientation of the crystallites is often observed, which can be influenced by various deposition parameters. As a result, certain angles may exhibit fewer reflections that are detected. The intensities of these peaks are then compared to those of a bulk standard, which quantifies the degree of preference for a specific crystal plane. Barrett and Massalski developed an equation known as the texture coefficient equation to calculate this preferred orientation:

$$Tc_{(hkl)} = \left[\frac{I_{(hkl)}}{I_{0(hkl)}}\right] \cdot \left[\frac{1}{n}\sum_{1}^{n}\frac{I_{(hkl)}}{I_{0(hkl)}}\right]^{-1}$$

In the equation above, texture coefficient for the *hkl* plane is denoted Tc, *I(hkl)* is the measured intensity, I_0(*hkl*) is the intensity of the bulk standard and *n* is the number of reflections observed. If the Tc(*hkl*) value is above one, this means that the crystallites in this (*hkl*) plane are preferentially orientated.

2.3.1.5 Equipment

X-ray diffraction (XRD) analysis is conducted using a Bruker D8 Discover diffractometer under ambient conditions. Monochromatic Cu Kα1 and Kα2 radiation (with respective wavelengths of 1.54056 Å and 1.54439 Å) is employed. Diffraction data is collected across a range of 2θ = 10-66° with a step size of 0.05° and dwell time of 2s per step. The diffractometer is operated at 40 kV and 40 mA. The obtained diffraction patterns are compared against reference data from the Inorganic Crystal Structure Database (ICSD). The sample used for XRD remains intact and can be further analysed.

2.3.2 UV-visible-near infrared spectroscopy

UV/Vis spectra were recorded using a Perkin Elmer Fourier Transform Lambda 950 UV/Vis spectrometer covering a range of 250–2500 nm, in both transmission and reflectance modes.

2.3.3 X-ray photoelectron spectroscopy (XPS)

The elemental composition of a 1 cm x 1 cm thin film was analysed using X-ray photoelectron spectroscopy (XPS) with a Thermo Scientific K-alpha spectrometer. Firstly, a survey scan is conducted across 0–1200 eV to identify the elements presents in the film. Followed by high-resolution XPS measurements on the specific elements identified during the survey scan. CASA XPS software is then used to calibrate the data to C1s (285 eV) and determine the chemical composition of the film. XPS analysis may damage the samples due to prolonged ion beam exposure and X-ray radiation, which can alter surface chemistry or introduce defects. Additionally, vacuum conditions may cause sample heating, potentially leading to thermal damage. As a result, samples used for XPS are disposed of and not reused for further testing.

2.3.4 Scanning electron microscopy (SEM)

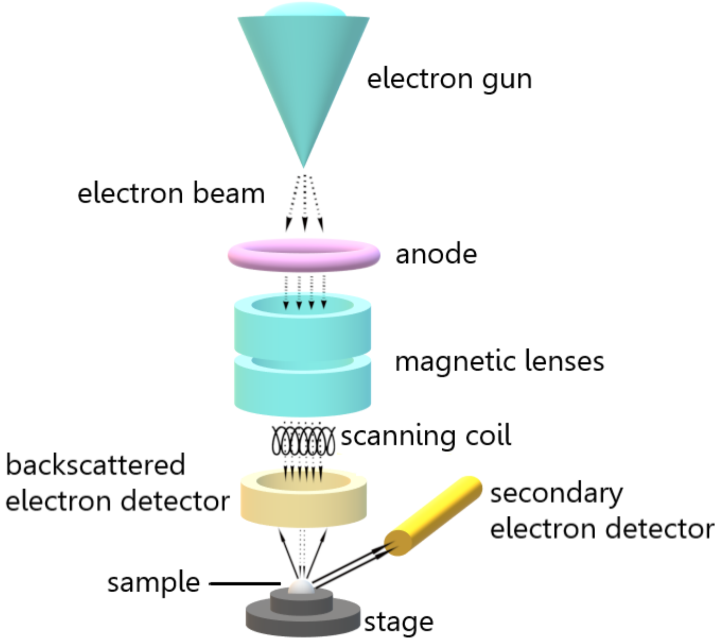

Figure 2.3 - Schematic of a scanning electron microscope

A scanning electron microscope (SEM) is used to capture high-resolution top-down and side-view images of the thin films to analyse their morphology and determine their thickness. Firstly, the substrate is cut to roughly 2 cm x 2 cm squares and affixed to the sample stubs with carbon and copper tape. This is to ensure secure attachment and enhance conductivity for improved image quality. Samples are sputter-coated with gold for 20 seconds before imaging with a JEOL JSM-6301F SEM instrument. The gold-coated samples are not reused after imaging and are discarded.

2.3.5 Electrical testing

Thin film resistivity, free charge carrier concentrations, and mobilities are measured using Hall effect measurements with the Van der Pauw method. Substrates were cut roughly to 1 cm x 1 cm squares and an Ecopia HMS-3000 instrument, equipped with a 0.58 T magnet is used for testing electrical properties.

2.3.6 Optical measurement of film thickness

The thickness of the films was determined by using the Filmetrics F20 machine in reflectance mode, comparing it to an FTO standard. The device measures light reflection from the sample across a wavelength range of 350-1000nm, and this data is processed using the fast Fourier transform (FFT) technique. The resulting data is presented as a graph of oscillations, which is then fitted to a theoretical model using a goodness of fit approach. The thickness measurements obtained for the thin films using this method are verified using side on SEM images to ensure reliable results.

2.3.7 Film adherence

Finally, the adhesion of the thin film to the glass substrate was tested using the standard Scotch tape test. This involved applying Scotch tape to the film and then peeling it off to assess whether the thin film adhered properly to the substrate without peeling away.

Following the scotch tape test, abrasion resistance of the thin film was tested using a steel scalpel.

2.4 Project Aims

The first results chapter of this thesis focuses on exploring the morphology and optoelectronic properties of ZnO thin films made using various molecular precursors with differing Zn:O ratios. Specifically, commercially available precursors such as zinc acetylacetonate and diethyl zinc are initially used to deposit ZnO thin films via AACVD and correlate the effects of the Zn:O ratio in the precursor on the final film properties. Additionally, ZnO thin films are synthesised using an innovative alkylzincalkoxide precursor developed by Sanchez-Perez *et al*.[64] This precursor features a preorganized Zn_4O_4 structure, facilitating the deposition of highly oriented and well-defined thin films. Importantly, this first chapter lays the groundwork for the rest of the thesis by examining the ZnO thin films to elucidate how the choice of precursor influences the final properties of thin films for TCO applications.

The second results chapter of this thesis explores the use of ZnO thin films as structural templates to epitaxially grow highly self-textured, compact, and transparent ZnO film coatings. This method presents an alternative to expensive and opaque c-silicon or c-Al_2O_3 which are widely used as crystallographic templates to grow highly oriented thin films. The growth of highly textured ZnO thin films aims to minimise resistance and optimise mobility in the thin films. The final chapter uses the precursor designed by Sanchez-Perez *et al* to deposit Al doped ZnO thin films to grow highly oriented thin films.[64]

Chapter 3 – Understanding the effect of Zn:O ratio in molecular precursors on the morphology and optoelectronic properties of ZnO thin films

3.1 Introduction

This chapter explores the use of 3 different precursors with varying Zn:O ratio to deposit zinc oxide thin films and compares the resultant morphologies and optoelectronic properties of the thin films. The study aims to understand how the chemical environment of the Zn centre during film growth impacts crystal growth and thus optoelectronic properties of the film. In particular, the study focuses on comparing oxygen rich and oxygen poor environments around the Zn centre during nucleation and sheds light on the crystal growth observed in these different conditions.

A study by Fujimura *et al.* reported preferential crystal growth is observed in the 002 direction (most energetically stable plane) in oxygen rich conditions resulting in tetrahedrally coordinated ZnO with 1:1 Zn/O ratio.[65] As such, these oxygen-rich conditions are typically used in research and industry. In contrast, it was suggested that oxygen poor conditions deteriorate tetrahedral coordination in ZnO leading to the preferential growth of thin films towards (110) and (101) crystal planes.[66,67] This results in the growth of polycrystalline ZnO materials with high grain boundaries that can significantly reduce mobilities in thin films which is unwanted.

The first set of ZnO thin films presented in this chapter are prepared using commercially available precursor, zinc acetylacetonate, commonly known as Zn(acac)$_2$. Zinc acetylacetonate has a Zn:O ratio of 1:4 providing oxygen rich conditions for film growth to take place. These films were grown employing a single-pot AACVD setup, with methanol serving as the solvent.

The second series of Zinc Oxide thin films were prepared using another commercially available Zinc precursor, diethyl zinc also known as DEZ. Diethyl zinc in this case creates an oxygen deficient environment in which the Zinc centres have a 1:0 Zn/O ratio. For the deposition of these films a dual source AACVD set up was employed using diethyl zinc as the Zinc precursor with either Hexane or Toluene used as the solvents and either methanol or IPA used as oxygen sources. In the gas-phase reaction, when DEZ reacts with methanol and isopropanol, the reaction intermediates are identified as ethyl zinc methoxide (EZM) and ethyl zinc isopropoxide (EZI). In this study, the aforementioned solvents are kept the same for the purpose of this study as we know solvents play a role in the AACVD process.

The final set of ZnO thin films presented in this chapter uses a single source AACVD set up using ethylzinc isopropoxide (EZI) as the Zinc precursor, synthesised using the method published by Sanchez-Perez *et al.*[64] The thin films were all deposited between temperatures ranging from 300°C to 500°C, at intervals of 50°C.

The intermediate formed during the reaction of DEZ with toluene and IPA is isolated to create this single-source precursor, designed to provide all the required bonds for the target thin film. EZI has a Zn:O ratio of 1:1 forming “preorganised Zn_4O_4 heterocubane like structure” to provide an oxygen rich environment.

The synthesis of a precursor with pre-existent Zn-O bonds enables the growth of thin films at lower temperatures requiring less energy intensive deposition conditions reducing overall manufacturing costs. Thus, designing single source precursors (SSPs) to have a similar molecular structure to the bulk structure of the thin film, in this case ZnO has attracted scientific interest. SSPs are generally more stable in air and moisture, simplifying handling compared to dual-source precursors (DEZ and Tol/IPA). In addition to these advantages, the lower deposition temperatures needed for highly textured films using EZI means they can potentially be used to deposit on to temperature sensitive substrates.

The strong pre-existent ZnO bonds in SSPs presents a low-cost route to grow highly textured thin films that exhibit excellent optoelectronic properties, removing the need for costly growth techniques currently employed to achieve such properties. It also avoids the need for expensive single crystal substrates that enable epitaxial growth of thin films which is further explored in Chapter 4.

Zinc oxide has attracted scientific interest as an alternative TCO material due to its low cost and high abundance of naturally occurring zinc containing minerals. Unlike ITO, zinc oxide avoids the need for rare metals like indium and is not reliant on unstable supply chains. Compared with indium and tin, ZnO also has a relatively low toxicity and has equally become an industrially important semiconductor used for TCO applications.[38]

Zinc oxide exhibits high transparency due to its wide direct band gap of 3.37eV which is greater than the optical bandgap of 3.1eV allowing visible light to pass through, making it a transparent conducting oxide. ITO in comparison has a slightly larger direct band gap value of 3.6eV. Undoped ZnO exhibits low conductivity due to the presence of inherent defects.

ZnO thin films have been extensively studied in literature and have commonly been doped to improve its electrical conductivity. However, these ZnO thin films are limited to the palette of commercially available Zn precursors such as zinc acetylacetonate and diethyl zinc.

This chapter studies the effect of using Zn precursors with different Zn:O ratios in different both oxygen rich and oxygen poor environments to understand the relation between resultant film properties and chemical environment of Zn centres during thin film growth. The final set of films produced in this chapter uses a preorganised molecular precursor designed by Sanchez *et al* which promotes the growth of highly oriented thin films. This orientation reduces resistance from grain boundaries, thereby enhancing mobility and, consequently, increasing the conductivity of the films.[64]

3.2 Precursors

Three precursors are studied in this chapter, 2 of which are commercially available precursors and the final precursor presented in this study is a single source precursor (SSP) designed by Sanchez Perez *et al.*[64]

The first precursor used to make ZnO thin films is commercially available zinc acetyl acetonate $Zn(acac)_2$. Zinc acetyl acetonate has been widely used to deposit ZnO thin films using AACVD. It was used to deposit a range of thin films between a temperature range of 300°C to 500°C using a single pot AACVD deposition set up as described in the earlier section. It is important to note during depositions using $Zn(acac)_2$ pipe blockages frequently took place requiring the need to clean out all the pipes and remove decomposed precursor. This was due to the low solubility of the precursor in the MeOH solvent resulting in highly diluted precursor solutions. The low solubility of this precursor has been noted in other studies and other chemicals have been added to aid the solubility of $Zn(acac)_2$. [68] This precursor presents an oxygen rich environment in which the Zn/O ratio is 1:4.

The second precursor employed to make ZnO thin films is diethyl zinc (DEZ) which is another commercially available zinc precursor. A dual source AACVD set up was employed to deposit thin films using the precursor DEZ. Diethyl zinc is highly pyrophoric and needed to be treated with caution as it reacts violently with O containing species therefore deposition using this precursor was carried out under inert conditions. The high reactivity of this precursor required the need to use a cooling system around the baffle to prevent blockages caused by the decomposition of the precursor before entering the reaction chamber. A variation of solvents and alcohols was used in the dual source deposition of the DEZ thin films to determine the best growth conditions. This precursor presents an oxygen poor environment where the Zn/O ratio is 1:0.

The third and last precursor used to deposit ZnO thin films is ethylzinc isopropoxide (EZI) a single source precursor (SSP) developed by Sanchez Perez *et al.*[64] EZI is the isolated intermediate from DEZ and Tol/ IPA solution and is not highly pyrophoric like its counterpart DEZ (Precursor 2). Toluene has been used as the solvent to deposit EZI across a temperature range of 300°C to 500°C at 50°C intervals. Ethylzinc isopropoxide presents an optimal oxygen environment around the Zn centres with a 1:1 Zn/O ratio.

Table 2 below summarise the variations in hydrocarbons and alcohols used as co solvents for the delivery of the three different precursors studied in this chapter. The carrier gas flow rate, deposition time and calculated growth rates have also been reported in the table below.

Table 2 - Experimental details for the synthesis of ZnO thin films using three different Zinc based precursors: ($Zn(acac)_2$, DEZ and EZI. The temperature of the reaction chamber ranged from 300 ˚C to 500 ˚C in intervals of 50 ˚C.

Precursor #	**Precursor**	**Zn:O ratio**	**AACVD Configuration**	**Hydrocarbon**		**Alcohol**		**Flow**	**Time**	**Growth rate**
				solvent	*(mL)*	*solvent*	*(mL)*	*(L min^{-1})*	*(min)*	*(nm min^{-1})*
1	$Zn(acac)_2$	1:4	Single source	-		MeOH	*100*	1.2	100	6
2	DEZ	1:0	Dual source	Hexane	*30*	MeOH	*35*	2x 0.8	20	30
				Toluene	*20*	MeOH	*35*	2x 0.8	30	20
				Hexane	*30*	IPA	*15*	2x 0.8	10	60
				Toluene	*20*	IPA	*15*	2x 0.8	20	30
3	EZI	1:1	Single source	Hexane	*15*	IPA	*15*	1.8	15	40
				Toluene	*10*	IPA	*15*	1.8	15	40

3.3 Materials

Precursor 1 - Zinc acetylacetonate (Sigma) and methanol (99.5%) were used as supplied.

Precursor 2 - diethylzinc (DEZ) in anhydrous hexane (1.0 M, Acros Organics) or toluene (1.1 M, Sigma) and anhydrous methanol (MeOH, Sigma) and isopropanol (IPA, Acros Organics) were used as supplied in the thin film depositions.

Precursor 3 – diethylzinc (DEZ) in anhydrous toluene (1.0 M, Acros Organics) or toluene (1.1 M, Sigma) and anhydrous isopropanol (IPA, Acros Organics) were employed for the synthesis of the ZnO precursors and thin films.

For all 3 precursor depositions: Nitrogen carrier gas (N_2, 99.99%) was obtained from BOC; Float glass with a 25 nm SiO_2 barrier layer was provided by NSG Pilkington Ltd and cut manually into substrates (50 × 145 × 4 mm).

3.4 Thin film growth

AACVD depositions were carried out using the methods described in previous sections. The deposition temperature ranged from 300 ˚C to 500 ˚C in steps of 50˚ and deposition times varied from 10 to 100 min.

Precursor 1

1.3 g of anhydrous $Zn(acac)_2$ was dissolved in 100 mL of MeOH and sonicated for 10 minutes using an ultrasonic bath to dissolve precursor 1 in the solvent. A single-pot AACVD setup was used in which the carried gas flow rate was maintained at 1.2 L min^{-1} for all deposition temperatures and deposition times lasted as long as 100 min.

Precursor 2

Commercially available precursor, diethyl zinc (DEZ) has been used as the Zn precursor in a dual source AACVD set up. The depositions involved a combination of hydrocarbon solvent (such as hexane or toluene) mixed with DEZ in one bubbler. The second bubbler contained the alcohol (oxygen source) in this case MeOH or IPA was used.

The variation of hydrocarbon solvents and alcohols used in each of the bubblers for DEZ depositions has therefore been further broken down into the following naming format to make it clear which combination of solvents have been used in the deposition (**precursor number** - **hydrocarbon solvent** – **alcohol**).

2-H-M) Diethylzinc solution (DEZ) with MeOH as the alcohol/ oxygen source. A dual-source AACVD setup was employed in which 5 mL of DEZ in hexanes (1.0 M) was diluted in 30 mL (hexane) in the first bubbler and 35 mL of anhydrous MeOH was placed in the second bubbler.

2-T-M) Diethylzinc solution (DEZ) with MeOH as the alcohol/ oxygen source. A dual-source AACVD setup was employed in which 3.5 mL of DEZ in toluene (1.1 M) was diluted in 15 mL (toluene) of solvent in one bubbler and 35 mL of anhydrous MeOH was placed in the second bubbler.

Flow rates were kept equal for both bubblers between 0.8 - 1.0 L min^{-1}. On average, depositions took 20 min for DEZ in hexane and 30 min DEZ in toluene.

During the dual source deposition reaction, the aerosolised mists of diethylzinc and methanol combine in the Y-joint. In this reaction, it is expected that zinc methoxide[69] as well as other clusters, such as cubanes, are formed as intermediates like the ones discussed in the studies by Jana *et al*. and Sokolowski *et al*.[70,71] Subsequently, these precursor intermediates undergo decomposition in the CVD reactor, leading to the formation of the ZnO film.

2-H-I) Diethylzinc solution (DEZ) with IPA as the alcohol/ oxygen source. A dual-source AACVD setup was employed in which 5 mL of DEZ in hexanes (1.0 M) were diluted in 15 mL (hexane) solvent in one bubbler and the second bubbler was filled with a mixture of anhydrous IPA and hexane (15 + 15 mL).

2-T-I) Diethylzinc solution (DEZ) with IPA as the alcohol/ oxygen source. A dual-source AACVD setup was employed in which 3.5 mL of DEZ in toluene (1.1 M) were diluted in 10 mL (toluene) of solvent in one bubbler and the second bubbler was filled with a mixture of anhydrous IPA and toluene (10 + 10 mL).

Flow rates were equal for both bubbles at 0.8 - 1.0 L min^{-1}. In general, depositions took 10 min for the precursor, DEZ in hexane and 20 min for DEZ in toluene.

Precursor 3

Ethylzinc isopropoxide (EZI) required a single-source AACVD setup. 5 mmol solution of ethylzinc alkoxide precursor was prepared according to the method published by Sanchez Perez *et al* as described below.[64]

Diethyl zinc and anhydrous toluene were added and mixed as the initial step in preparing the precursor. Subsequently, a cold bath was arranged around the Schlenk flask to cool the mixture down to a temperature of -78°C. Anhydrous isopropanol was then added drop by drop to the cooled down solution. After the reagents were mixed, a turbid solution formed and was allowed to stir for 5 minutes under an inert argon atmosphere. Following this, the solution was gradually warmed up to room temperature while continuing to stir, resulting in the dissipation of the turbidity. The precursor solution was prepared mixing DEZ in toluene and isopropanol (10 + 10 mL).

3.5 Result and discussion

3.5.1 Crystallography

3.5.1.1 Precursor 1 – Zinc acetyl acetonate

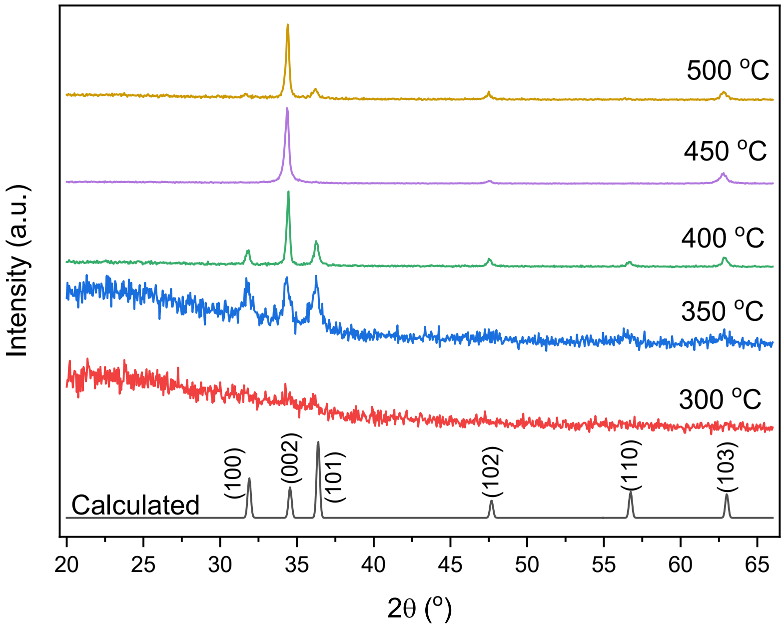

Figure 3.1 - X-ray diffraction pattern of ZnO thin film grown on glass substrate using precursor 1 - Zn(acac)$_2$

The x-ray diffraction patterns of the zinc oxide thin films synthesised from precursor 1, zinc acetyl acetonate (Zn(acac)$_2$), are presented above in Figure 3.1. The films were deposited onto glass substrates between a temperature range of 300°C to 500°C. The XRD pattern of the film deposited at 300°C is dominated by a low signal to noise ratio which is indicative of an amorphous thin film, as no peaks can be assigned. At 350°C, peaks can be observed roughly at 32°, 34.5° and 36° which correspond to the (100), (002) and (101) crystallographic planes of the hexagonal wurtzite structure of ZnO.

At a higher deposition temperature of 400°C a much more crystalline thin film is produced showing a principal peak corresponding to the (002) plane, suggesting preferred orientation in this plane. Smaller peaks are also seen in the (100) plane corresponding to the basal plane in the hexagonal unit cell and (101) plane corresponding to the non-basal plane of the hexagonal unit cell. A highly directional thin film is produced at 450°C with a strong peak corresponding to the (002) plane and at this temperature peaks corresponding to the (100) and (101) planes have disappeared. At the final deposition temperature of 500°C a similar pattern of preferred orientation is observed in the (002) plane with a principal peak seen at 34.5°. Similar observations have been made by Walter *et al.* using Zn(acac)$_2$ and methanol whereby preferred orientation is observed in the (002) plane and this orientation has been reported to be the most electrically conductive orientation for ZnO thin films.[72]

In general, as the deposition temperature increases, sharper peaks are observed in the XRD patterns, the increase in intensity and narrowing of the peaks suggest an increase in crystallinity in the thin films deposited. This trend is in close agreement with ZnO thin films grown using other techniques.[73] The crystal quality of the thin film is related to the crystallite diameters of the thin films. Thus, it is further corroborated by the crystallite diameters estimated using the Scherrer equation in Figure 3.2 below. Except for the thin film grown at 400°C, all the other films show a positive correlation between the estimated crystallite sizes and deposition temperature. The large errors associated with crystallite size estimations means these calculations should only be used to observe trends. Determining error values in crystallite size measurements using the Scherrer equation presents challenges because of assumptions regarding spherical crystallites, instrumental broadening effects, sample heterogeneity, variability in data analysis techniques, and sample preparation methods. As such these factors contribute to uncertainties in determining crystallite size accuracy, making it difficult to precisely quantify error values.

As deposition temperature increases, adatoms on the substrate gain kinetic energy, enabling them to migrate to lower energy sites before nucleation. This results in thin films with larger grain growth at higher temperatures as seen in the study of ZnO thin films grown using precursor 1, Zn(acac)$_2$. Similar observations have been made by Potter *et al* when using precursor 1 for AACVD depositions of ZnO thin films.[68,74]

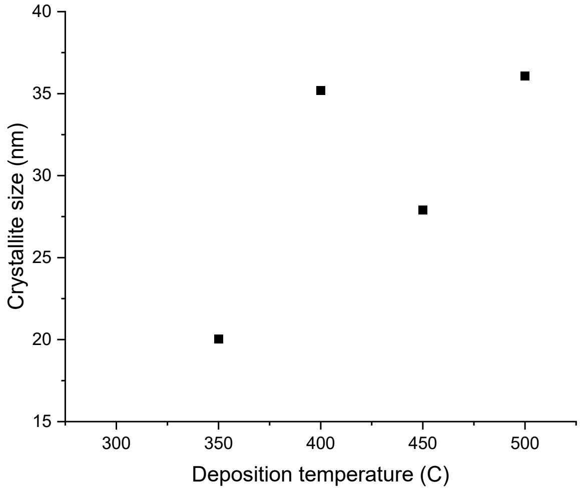

Figure 3.2 - Estimated crystallite diameters for ZnO thin films grown using precursor 1 - Zn(acac)$_2$

As expected, the thin films grown using precursor 1 has preferential growth along the (002) crystallographic plane. This plane is perpendicular to the basal plane of the hexagonal unit cell and offers the lowest surface energy for growth, making it the most energetically favourable plane. The variation in texture coefficients in each of the planes has been calculated and plotted in Figure 3.3 below. From this figure it is clear the thin film grown at 450°C has a highly texture film in the c-axis with a Tc value above 5.

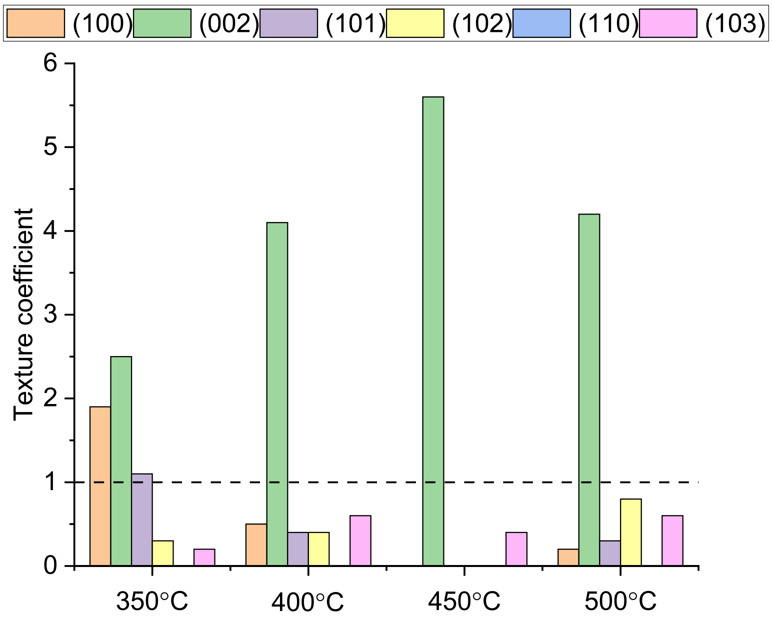

Figure 3.3 -Variation of (Tc) of each plane in ZnO thin films grown using precursor 1 - Zn(acac)$_2$

Despite the highly textured thin films grown using precursor 1, growing such films using this precursor is unreliable and difficult in AACVD. Although precursor 1 is a readily available precursor that can be used as supplied it presents some issues as a viable precursor for AACVD.

Firstly, its low solubility in solvents requires the extra step of using an ultrasonic bath to sonicate the solution to help the precursor dissolve in a given solvent, in this case methanol. The low solubility of this precursor lead to pipe blockages in the AACVD leaving large residues of undissolved precursor in the AACVD system. Requiring extensive cleaning of the equipment used after each deposition. Several deposition temperatures had to be repeated multiple times to achieve good substrate coverage. Further to this the low solubility of the precursor resulted in highly diluted solutions reducing the concentration of precursor 1 that was delivered to the reaction chamber.

Section 1.2.2.1 outlines the key requirements of a precursor for use in AACVD depositions, based on these requirements precursor 1 does not tick many of these requirements and as a result presents many problems during thin film depositions. The low solubility and other observations described above make this precursor a far from ideal precursor to use for AACVD depositions.

3.5.1.2 Precursor 2 – Diethyl Zinc

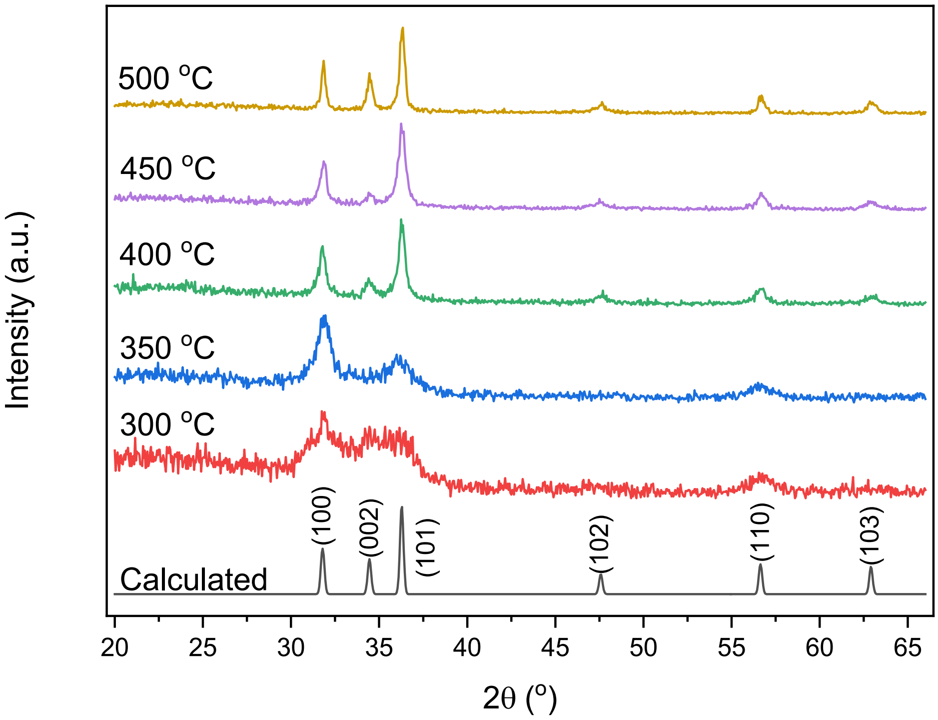

Figure 3.4 - X-ray diffraction pattern of ZnO grown on glass substrate using precursor 2-H-M, DEZ in Hexane with MeOH grown between a temperature range of 300℃ to 500℃

X-ray diffraction patterns of ZnO thin films grown using precursor 2-H-M, diethyl zinc (DEZ) in a dual source deposition with Hexane/ MeOH are presented in Figure 3.4. The thin film grown at 300°C has a relatively broad peak corresponding to the (100) plane showing very low crystallinity at this temperature. At 350°C the signal to noise ratio is much lower and peaks can be seen to form around 32° and 36°, corresponding to the (100) and (101) crystallographic planes. Deposition at 400°C have more pronounced and sharper peaks with a principal peak seen at 36° followed by a smaller peak at 32°. The formation of a peak is seen at 34.5° suggesting small growth in the (002) crystallographic plane as well.

Interestingly, unlike the thin films made using $Zn(acac)_2$, these films do not exhibit preferential growth in the (002) plane. The same is observed for the thin film produced at 450°C where preferential growth is not observed in the (002) plane but rather in the (101) plane. The film made at 500°C shows a highly crystalline film with preferential growth seen in the (101) crystallographic plane corresponding to the non-basal plane of the hexagonal wurtzite structure. Following a similar pattern to the other films produced using DEZ in Hexane and MeOH, the film at 500°C has peaks corresponding to the (100) and (101) crystallographic planes as well confirming the presence of wurtzite ZnO.

The texture coefficients of each of the planes in the ZnO thin films grown using precursor 2-H-M all show crystal growth preference in the non-polar (100) and (110) planes. The precursor 2-H-M had a Zn/O of 1:0 creating an oxygen deficient environment for Zn centres during nucleation. It is likely the reaction proceeds via the formation of ethyl zinc methoxide as an intermediate.[75] Similar observations and conclusions have been made by Fujimura *et al* who have suggested oxygen poor environments give rise to non-polar growth.[65]

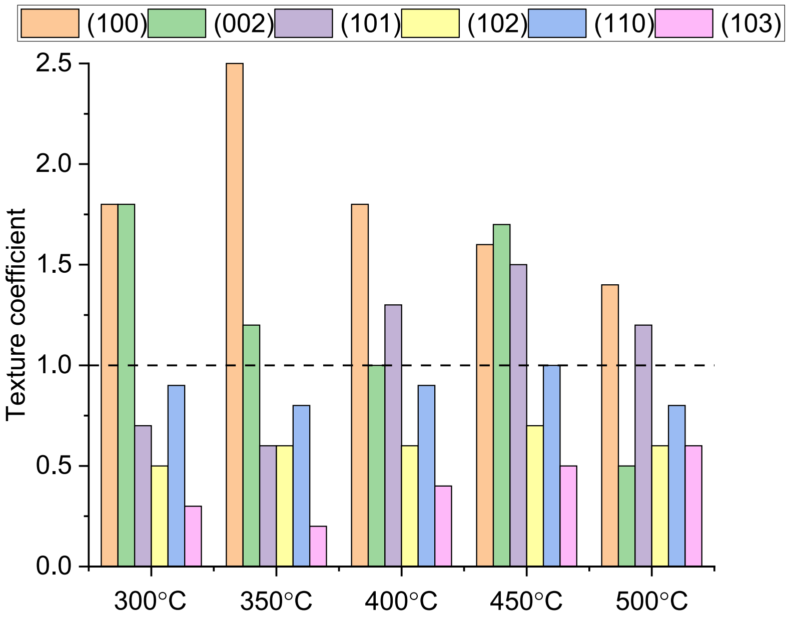

Figure 3.5 - Variation in texture coefficient for films deposited using precursor 2-H-M, DEZ in Hexane with MeOH

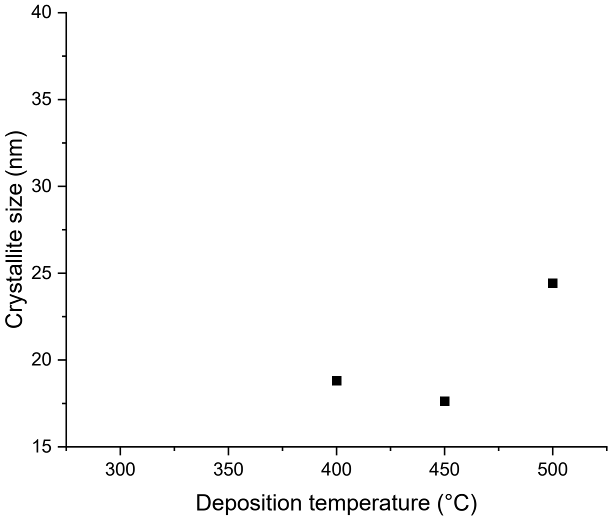

Figure 3.6 - Estimated crystallite diameters for ZnO thin films grown using precursor 2-H-M, DEZ in Hexane with MeOH

The crystallite sizes of the thin films grown using precursor 2-H-M were estimated using the Scherrer equations to identify trends in the crystal growth. Films grown at 300°C and 350°C were not crystalline enough to calculate crystallite sizes. For the remaining thin films, the crystallite sizes ranged from 15nm – 25nm. This is much lower than the thin films grown using precursor 1 suggesting overall reduced crystallinity in the films grown using 2-H-M.

From the observations above we can see non-polar growth is favoured in oxygen poor environments. The lack of oxygen around the Zn centre during nucleation gives rise to smaller crystallites when deposited at the same deposition temperature as oxygen rich conditions.

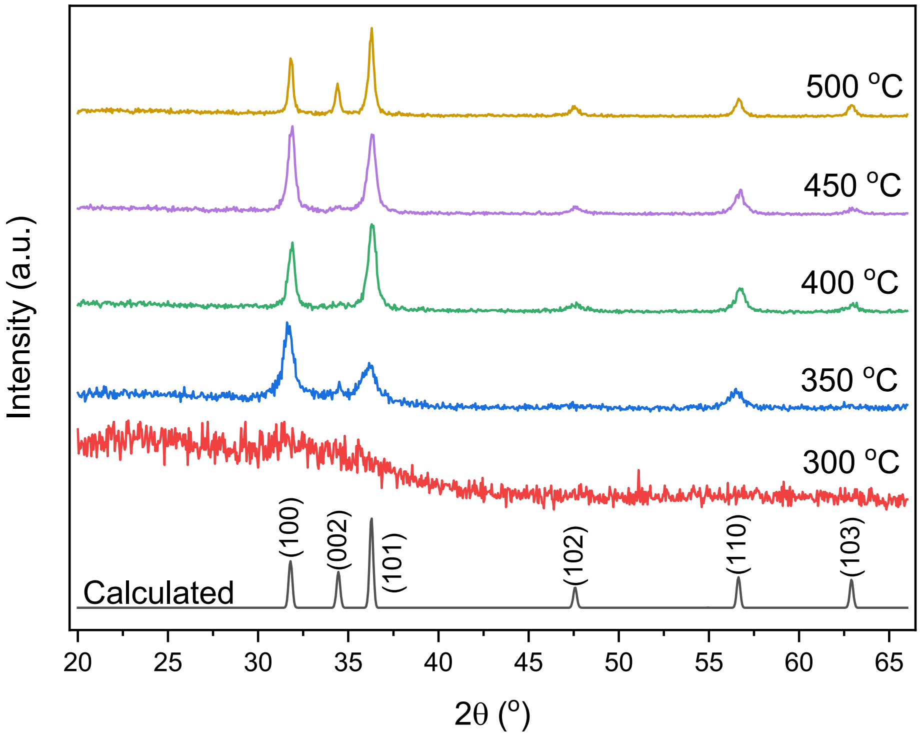

Figure 3.7 - X-ray diffraction pattern of ZnO grown using 2-T-M, DEZ in Toluene with MeOH

The crystal structure of the thin films produced using diethyl zinc in a dual source deposition with Toluene and MeOH can be determined from the x-ray diffraction patterns presented in Figure 3.7. At a low temperature deposition of 300°C an amorphous film is observed with no peaks that can be assigned to crystallographic planes. As the deposition temperature is increased to 350°C peaks are seen and growth along the (100), (101) and (110) planes are observed. A similar pattern is also seen in Figure 3.4, when depositing at 350°C. At 400°C the intensities of the peaks corresponding to the (100), (101) and (110) planes intensify.

A highly crystalline thin film is produced at 450°C with similar peaks as observed in the 400°C thin film. When deposition temperature is increased to 500°C a small peak is observed indicating growth along to (002) plane as well as (100) and (101) planes. The use of methanol as the oxygen source in the dual source depositions in both Figure 3.4 and Figure 3.7 shows growth along to (100) and (101) planes and growth in the (002) plane is only observed in insignificant amounts at a higher deposition temperature of 500°C.

Again, a similar trend is observed where nonpolar growth has been favoured in oxygen poor conditions around the Zn centre using precursor 2-T-M. The texture coefficients have been calculated for each of the planes and the (100) plane dominates across all thin films with an increase in (101) growth observed at higher temperatures.

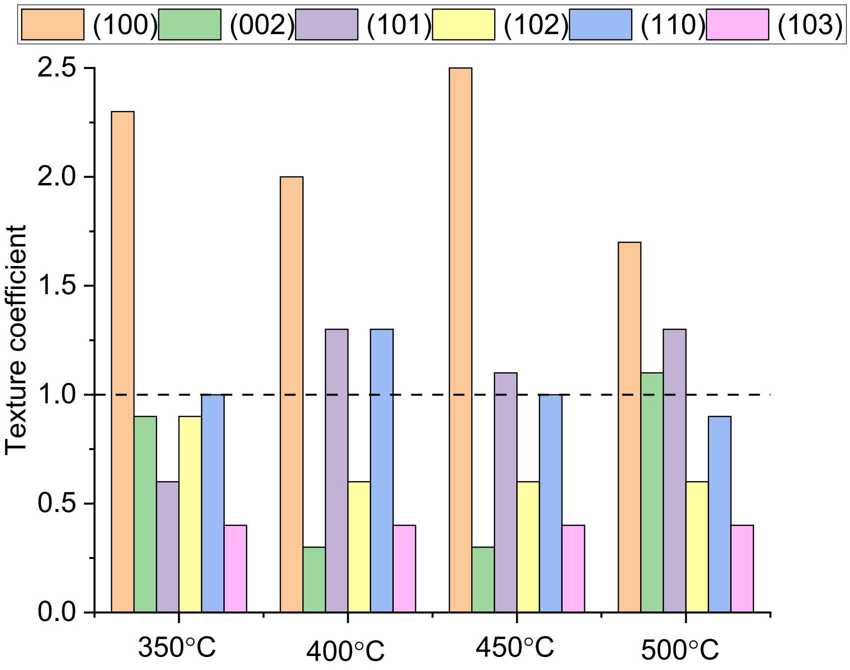

Figure 3.8 - Variation in texture coefficient for films deposited using 2-T-M, DEZ in Toluene with MeO

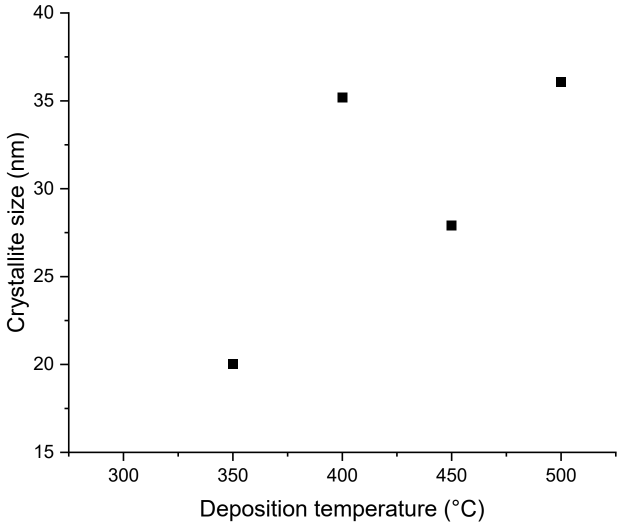

Figure 3.9 - Estimated crystallite diameters for ZnO thin films grown using precursor 2-T-M, DEZ in Toluene with MeOH

Crystallite diameters have been estimated using the Scherrer equation. Thin films grown above 350°C were crystalline enough to calculate the crystallite sizes. Pseudo-Voigt fitting of the peaks yielded FWHM values, used to estimate average crystallite diameter. These calculations are treated with caution due to the high error associated with them. Thin films grown using precursor 2-T-M have yielded thin films with larger crystallites suggesting these thin films have greater crystallinity than the films made previously using 2-H-M.

As temperature increases crystallite sizes also increase this is because grain grow to minimise their surface energy. Therefore, through reducing the number of grain boundaries, grain growth can lower the energy associated with grain boundaries giving rise to larger crystallites as seen in the Figure 3.9 above.

Both precursors 2-T-M and 2-H-M discussed above present ZnO thin films grown in oxygen poor conditions with the only difference being the use of solvent. For depositions using 2-H-M much lower crystallite sizes and overall crystallinity of the thin films was observed across the deposition temperatures. In contrast, in precursor 2-T-M where toluene was used as the hydrocarbon solvent the crystallite sizes were much larger and higher quality crystal growth is seen.

In general, the solubility of the DEZ precursor was lower in the hexane solvent and higher in the toluene solvent. Hexane has a lower boiling point than toluene which could result in faster grain growth. Therefore, it could be suggested that using hexane as a hydrocarbon solvent lead to fast nucleation which can yield smaller particles. When using toluene as the hydrocarbon solvent, slow nucleation takes place to give rise to larger grain sizes as seen in Figure 3.9.

Finally, it is worth noting for both precursors 2-H-M and 2-T-M the depositions were carried out under inert conditions using 2 bubblers to separate the oxygen containing species and prevent reactions taking place before entering the reaction chamber. A cooling system that uses ice cold water to main cool temperatures around the baffle was also employed to avoid earlier reactions outside the chamber. These extra steps were necessary to prevent the precursor from reacting outside the chamber due to its highly reactive nature. Although DEZ is a commercially available precursor, there are many steps involved in ensuring the successful deposition of ZnO thin films using this precursor. Further to this the solubility issues of the precursor reduces the concentration and purity of the precursor transported to the substrate. All of which results in thin films with subpar optoelectronic properties that are not fit for TCO applications.

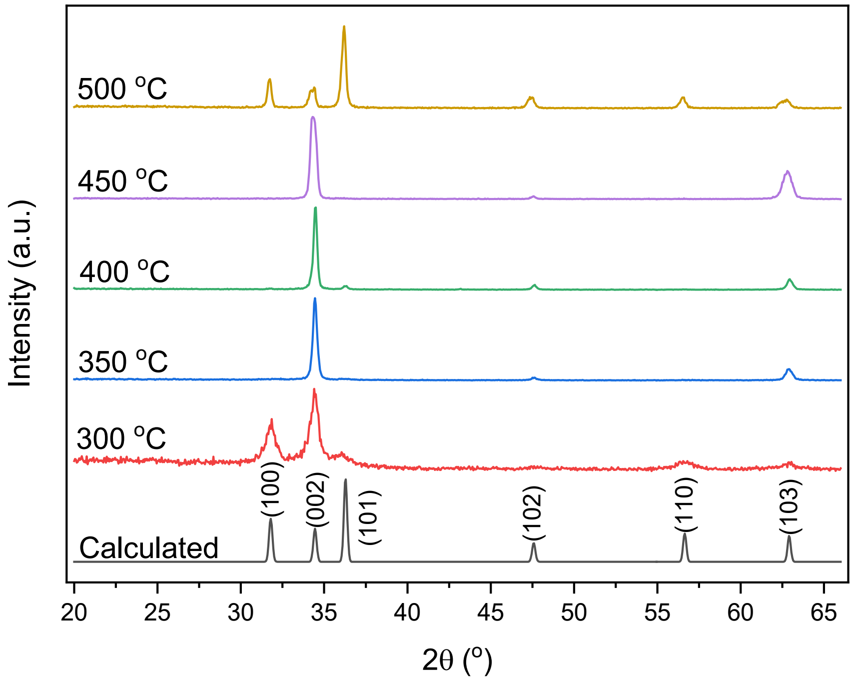

Figure 3.10 - X-ray diffraction pattern of ZnO grown using precursor 2-H-I, DEZ in Hexane and IPA

Figure 3.10 displays the x-ray diffraction pattern of the films produced in a dual source deposition with Hexane and IPA using diethyl zinc as the precursor. In contrast to Figures 3.4 and 3.7, the XRD patterns seen in Figure 3.10 show preferential growth in the (002) plane as opposed to (100) and (101) as seen in Figure 3.4 and Figure 3.7. At a low temperature deposition of 300°C, a crystalline film is observed where the principal peaks can be assigned to the (002) plane showing preferential growth in this plane. A secondary peak with a lower intensity is also seen in the (100) plane.

When increasing the deposition temperature to 350°C the secondary peak observed previously in the 300°C film disappears, and an intense principal peak is observed in the (002) peak with an insignificant peak corresponding to the (103) plane. The film produced at 400°C follows a similar pattern with a highly directional film in the (002) plane. At 450°C the principal peak remains in (002) plane with a higher intensity peak seen in the (103) plane. The film produced at 500°C does not follow a similar pattern and the principal peak is now seen in the (101) plane with smaller peaks seen in (100) and (002) planes.

Overall crystallinity of the thin films appears to increase with temperature. Thin films grown using precursor 2-H-I appear to have preferential growth in the 002 plane as confirmed by the texture coefficient calculations displayed in the bar chart below. At 450°C a texture coefficient above 4.5 is observed, thin films grown above this temperature suffer from a reduction in preferentially orientation. Particularly at 500°C, preferential orientation is significantly reduced and is now seen in the (101) polar plane.

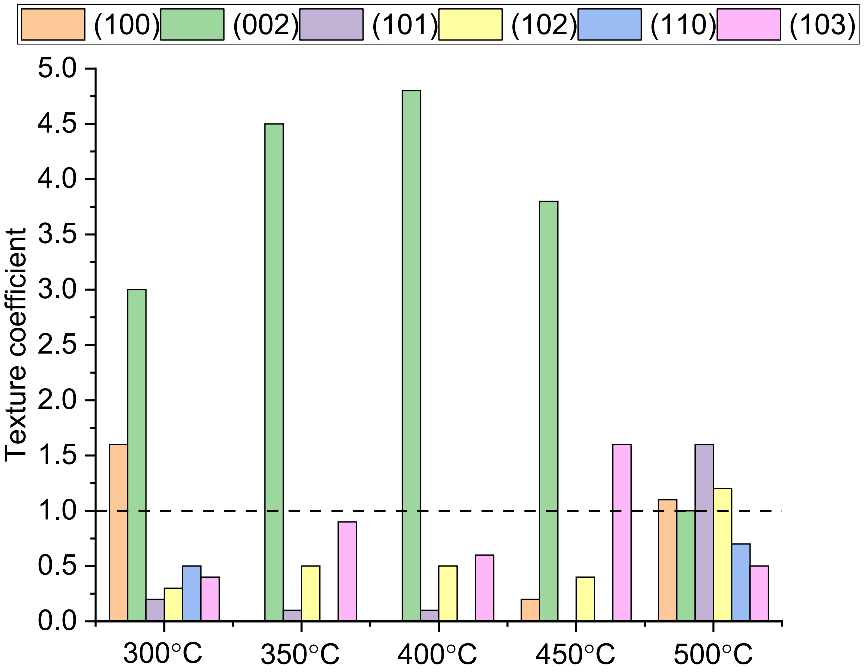

Figure 3.11 - Variation in texture coefficient for films deposited using precursor 2-H-I, DEZ in Hexane and IPA

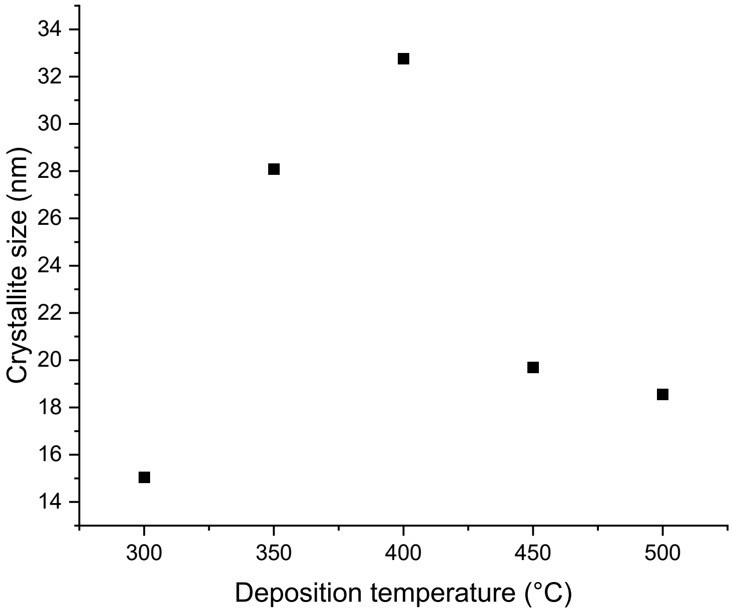

Figure 3.12 - Estimated crystallite diameters for ZnO thin films grown using precursor 2-H-I, DEZ in Hexane and IPA

Crystallite diameters of ZnO thin films (grown from 300°C to 500°C) were calculated using the Scherrer equation.[76] As expected, crystallite sizes decrease in thin films grown above 400°C. Crystal growth in multiple crystal planes leads to the reduction of grain sizes due to the increase in grain boundaries. Thus, this type of polycrystalline growth is unfavoured in thin films grown for TCO applications as this gives rise to increased grain boundaries which hinder electron mobilities and reduces conductivity.

The deposition of ZnO thin films grown using precursor 2-H-I presents thin films growth with preferred orientation towards polar planes such as 002. However, at higher temperatures this no longer remains the case and polycrystalline growth leads to a decrease in estimated crystallite sizes and overall film crystallinity.

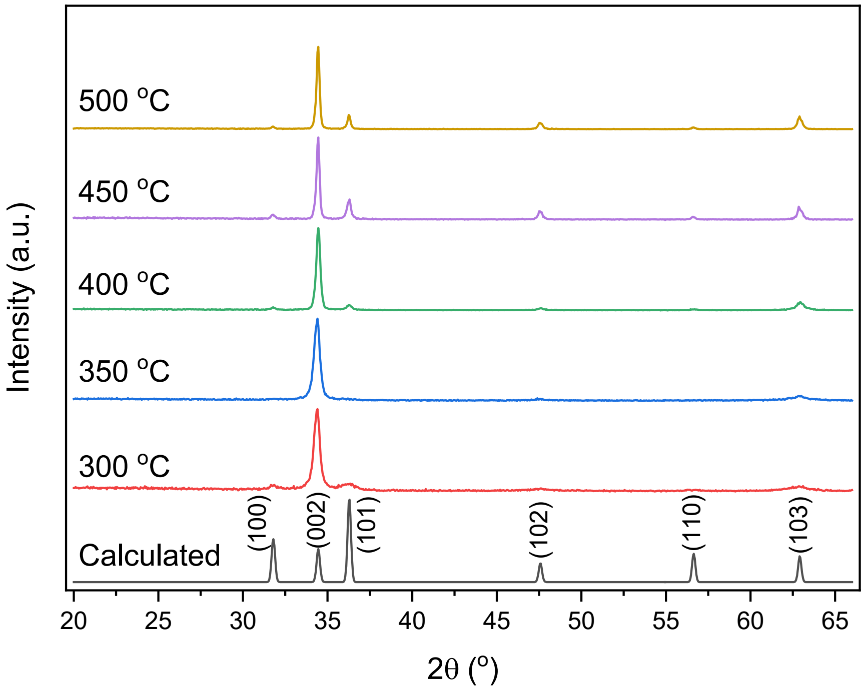

Figure 3.13 - X-ray diffraction pattern of ZnO grown using precursor 2-T-I, DEZ in Toluene and IPA

Like the films made using Hexane and IPA (seen earlier in Figure 3.10) the films in Figure 3.13 also show highly oriented thin films in the (002) plane. From a low temperature deposition of 300°C a principal peak is seen in the (002) plane. At 350°C a more crystalline thin film is produced with an increased peak intensity in the (002) plane. At 450°C peaks start to appear in the (101), (102) and (103) planes showing the formation of new crystalline phases. The film produced at 500°C follows a similar pattern with sharper peaks seen in the crystallographic planes present showing an increase in the crystallinity of the film produced.

Overall, as deposition temperature increased, the broader (002) peak seen in the 300°C thin film has become sharper as the deposition temperature was increased in increments of 50°C. This change in peak shape from a broad peak at 300°C to a very sharp peak at 500°C is due to the increased crystallinity and orientation in the (002) planes as deposition temperature increased.

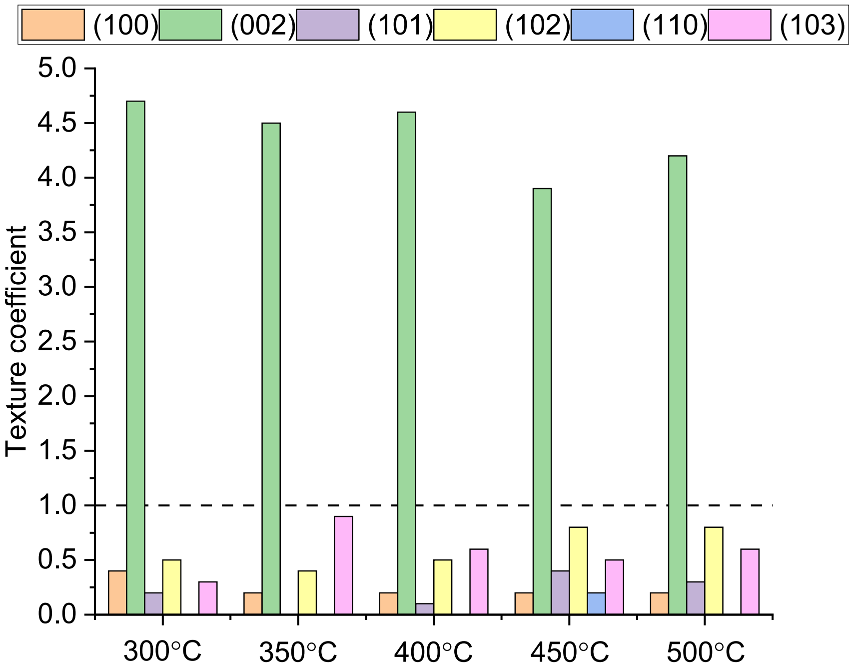

Figure 3.14 - Variation in texture coefficient for films deposited using precursor 2-T-I, DEZ in Toluene and IPA

The texture coefficients calculations of the thin films grown using precursor 2-T-I confirms preferential growth in the 002 direction across all deposition temperatures. Unlike precursor 2-H-I, precursor 2-T-I mostly promotes the growth of crystals in a singular crystal plane which is highly desirable for TCO applications.

Crystallite sizes of the thin films grown using precursor 2-T-I have been determined using the Scherrer equation to examine the crystal quality of the thin films. At higher deposition temperatures, adatoms possess greater energy to locate lower surface energy sites, resulting in the anticipated increase in crystallite size. In this case the 002 is the most energetically favourable therefore larger grains can be yielded at higher deposition temperatures.

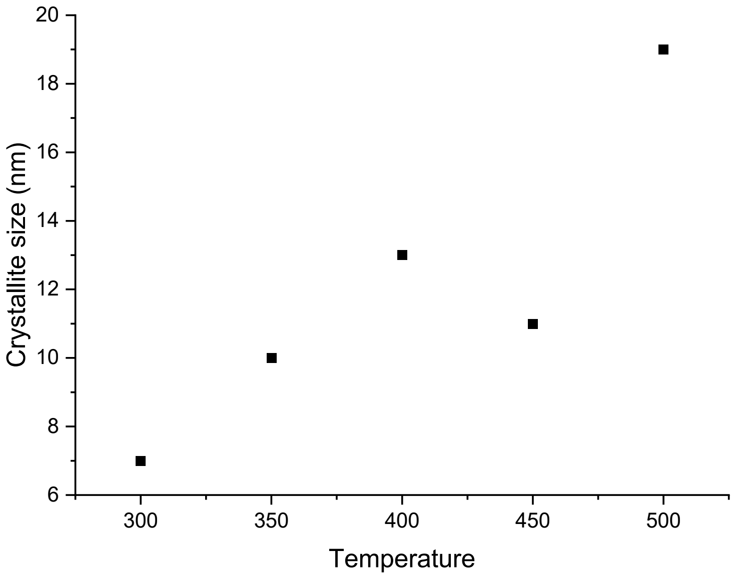

Figure 3.15 - Variation in crystallite size (nm) in thin films made using precursor 2-T-I, DEZ in Toluene and IPA

Although DEZ has been widely used in ZnO thin films depositions using AACVD and has been reported in literature many times. The pyrophoric nature of this precursors presents some hazards and requires additional measures to be taken to ensure the precursor is used safely to avoid violent reactions that could cause fire. Thus, industrially scaling the production of highly textured thin films made using this precursor would require additional costly steps which are not favourable or feasible in mass production. Further to this, the depositions carried out using precursor 2, diethyl zinc, required the need for a cooling system to be placed around the inlet to prevent decomposition of the precursor prior to being delivered to the substrate.

More importantly, the study of precursor 2 has shown that when thin films are grown in oxygen poor environments using MeOH as the alcohol solvent, crystal growth in non-polar planes is promoted. On the hand, highly textured thin films with crystal growth in the polar plane 002 is observed when isopropanol is used instead as the alcohol.

All the reasons mentioned above about DEZ makes the usage of the precursor dangerous and deems it an unsuitable precursor to scale up ZnO based TCOs for optoelectronic applications. Therefore, the next section of this chapter explores precursor 3 as a viable option to deposit ZnO thin films. Precursor 3 is a single source precursor designed by Sanchez-Perez *et al* which isolates the intermediate formed during the reaction of DEZ in toluene with toluene (hydrocarbon solvent) and isopropanol (alcohol/ oxygen source).[64] This precursor opens up a more facile and non-hazardous route to obtain highly textured thin films.

3.5.1.3 Precursor 3 – Ethyl zinc isopropoxide

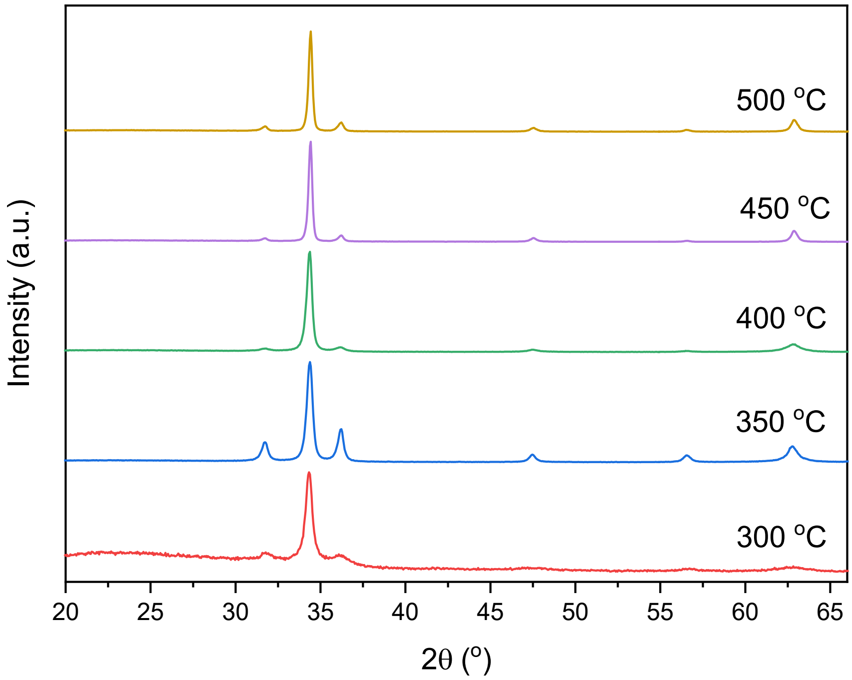

Figure 3.16 - X-ray diffraction pattern of ZnO grown using precursor 3, EZI, ethyl zinc ispropoxide

In the figure above, the XRD patterns of the thin films grown using precursor 3 (EZI) has been stacked in increasing deposition temperature. The thin film grown at 300°C shows a principal peak around 34.3° which can be assigned to the (002) plane in wurtzite ZnO. Either side of this principal peak, 2 smaller peaks are observed in the (100) and (101) planes confirming the presence of the wurtzite ZnO crystal structure. ZnO thin films almost exclusively exist in the wurtzite ZnO polymorph.

At 350°C defined peaks are observed with new peak formations in the (102), (110) and (103) suggesting an increase in crystallinity of the thin films. These new peaks then disappear again when ZnO is deposited at 400°C and the (002) peak remains to be the most intense. At both 450°C and 500°C the 002 peak is observed to become narrower and sharper indicating an increase in crystal quality of the thin films which is expected at higher deposition temperatures. In these films, the 002 remains to be the predominant peak and slightly more pronounced growth in the (103) plane is seen.

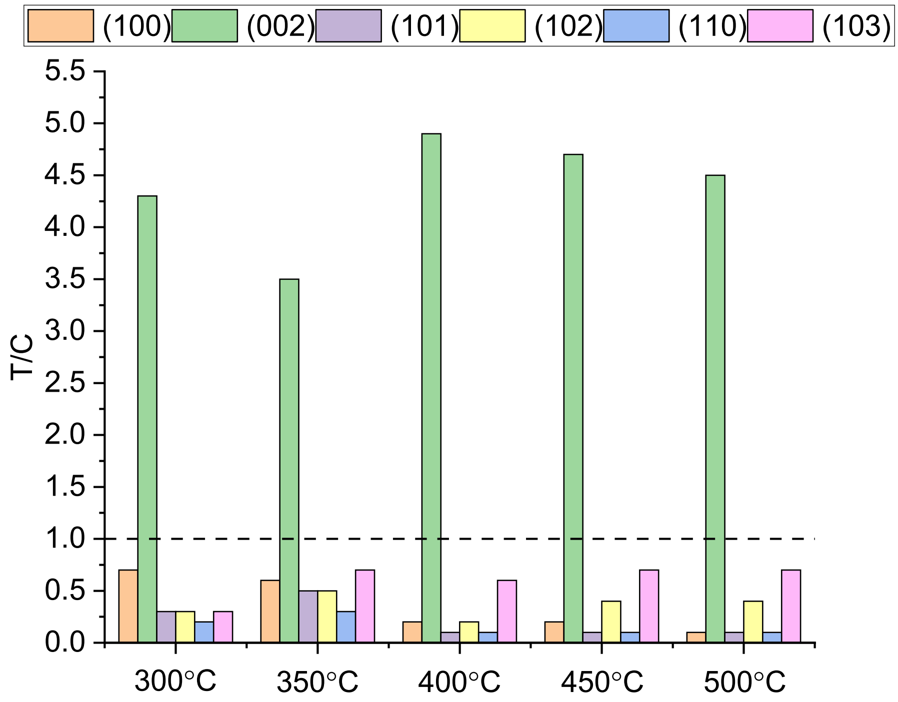

Figure 3.17 - Variation in texture coefficient for films deposited using precursor 3, EZI, ethyl zinc ispropoxide

The variation in texture coefficients for each plane has been calculated and plotted in the figure above. Preferred orientation in the 002 plane is observed similar to the films grown using precursor 2-T-I. However crystal growth is also seen in other planes such as 100, 102 and 103 across all the films. The film grown at 400°C is found to be the most textured with a T/C value above 4.5. Based on these calculations, precursor 3 presents a straightforward method to produce highly textured ZnO thin films in a single source deposition. Unlike the dual source deposition of precursor 2-T-I, precursor 3 does not require additional cooling systems or an extra bubbler set up with an alcohol source.

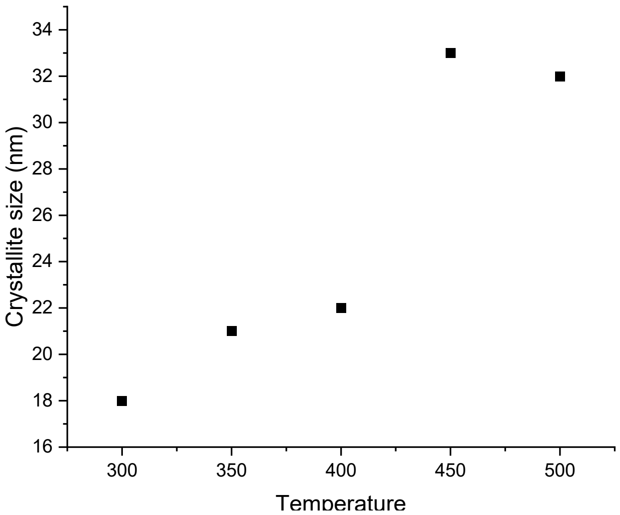

Figure 3.18 - Variation in crystallite size (nm) in thin films made using precursor 3, EZI, ethyl zinc ispropoxide

The crystallite sizes of the films grown using precursor 3 were estimated using the Scherrer equation and the results have been plotted in a scatter diagram above. The graph shows a positive correlation, whereby crystallite sizes increase as deposition temperature is increased. Crystallite sizes as large as 33nm have been achieved using this precursor. It is worth noting the dual source counterparts using precursor 2-H-I had only achieved crystallite size as large as 19nm at the highest deposition temperature. This confirms that sing this SSP produces thin films with superior crystal quality.

Higher deposition temperatures lead to larger crystallites and fewer grain boundaries due to increased adatom energy. This additional energy enables the adatoms to explore and locate the lowest energy sites before nucleation occurs, promoting the growth of films with larger crystallites. Consequently, the reduced presence of grain boundaries is observed in these films which is observed in the microscopy later.

3.5.2 Microscopy

SEM (scanning electron microscope) was used to capture top view images of the ZnO thin films and understand its surface morphology.

Precursor 1 – Zinc acetyl acetonate

Figure 3.19 shows the top view SEM images taken of ZnO thin films synthesised using Zn(acac)$_2$ as a precursor. The first two images in the series both show very thin and amorphous ZnO thin films grown at 300°C and 350°C. Small particle like wedges begin to form in the film grown at 350°C.

At a higher deposition temperature of 400°C much larger particle sizes are observed, and superficial wedges are seen which can be due to the contribution of non-planar planes as seen in the XRD in Figure 3.1. Some degree of directional growth is also seen to form in (Figure 3.19c) between the wedges which could be owed to the growth along the (002) plane.

In Figure 3.19d a much more compact and directional thin film is made with the disappearance of large superficial wedges. The thin film grown at 450°C appears to have a much more uniform appearance with larger crystallites in the (002) plane, as suggested by the XRD data in Figure 3.1. Walter *et al*. presented similar SEM micrographs of ZnO thin films grown at 450°C using Zn(acac)$_2$ and methanol whereby a similar morphology is seen.[72]

The final image in the series shows the top view SEM image taken of the ZnO thin film grown at 500°C. A mixture of smaller and larger crystallites is seen in this film. At higher temperature depositions of ZnO thin films grown using Zn(acac)$_2$ there is a tendency for the thin films produced to have a brown hue on the film suggesting there is a lot of carbon contamination on the film.

Therefore, the mixture of crystals seen in this film in Figure 3.19e could be due to the large carbon contamination in the film when depositing at higher temperature ranges. Aside from the larger crystal formations in this film grown at 500°C, it is evident that there are smaller directional crystallites grown in the 002 direction.

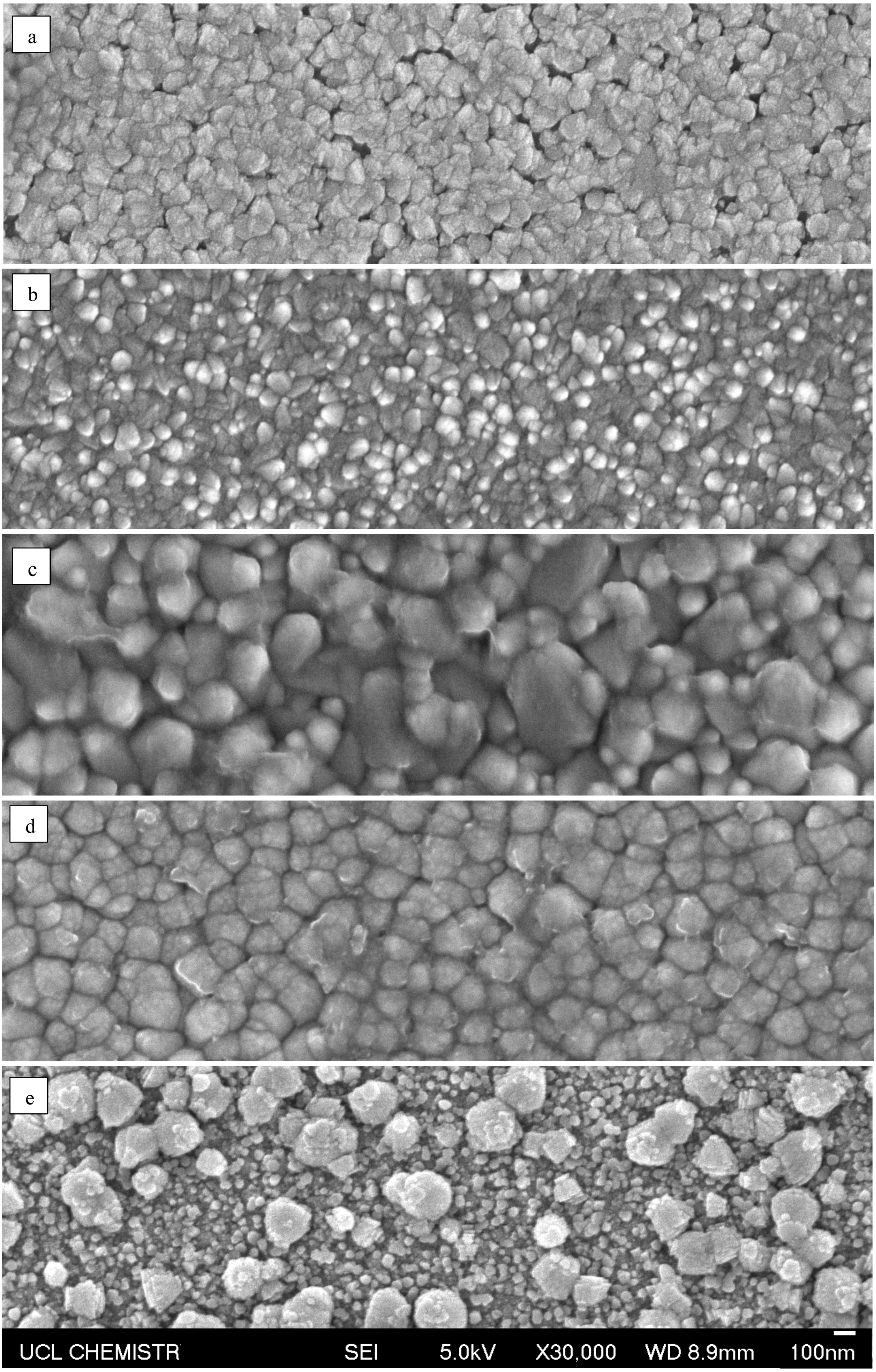

Figure 3.19 - Top view SEM images of ZnO thin films synthesised using precursor 1, Zn(acac)$_2$ as the precursor grown at a) 300 ℃ b)350 ℃ c) 400 ℃ d)450 ℃ e)500 ℃

Figure 3.20 displays the top view SEM images taken of the ZnO thin films grown using diethyl zinc in a dual source deposition with MeOH and Hexane. Image a shows small particle and is representative of an amorphous thin film produced, supported by the XRD measurement in Figure 3.4.

The film produced at 400°C (image b) appears to be more uniform with similar sized crystal formation. Larger particles can be observed in the film deposited at a higher deposition temperature of 400°C in image c. These particles could be owed to the growth seen in the (100) and (101) planes as seen in Figure 3.4 previously. When depositing at 450°C, a compact thin film is seen with top view SEM. Finally in image e, at 500°C, larger crystallites have formed with well-defined sharp wedges which protrude from the image.

Upon comparison with the XRD measurements in Figure 3.4 at 500°C there is a mixture of crystal growth in the (100), (002) and (101) planes which explains the multidirectional wedges seen to grow on top of each other in image e (final image of Figure 3.20).

In general, the films produced using diethyl zinc in a dual source deposition with Hexane and MeOH exhibited more transparent films with less carbon contamination than the films produced using $Zn(acac)_2$ and MeOH.

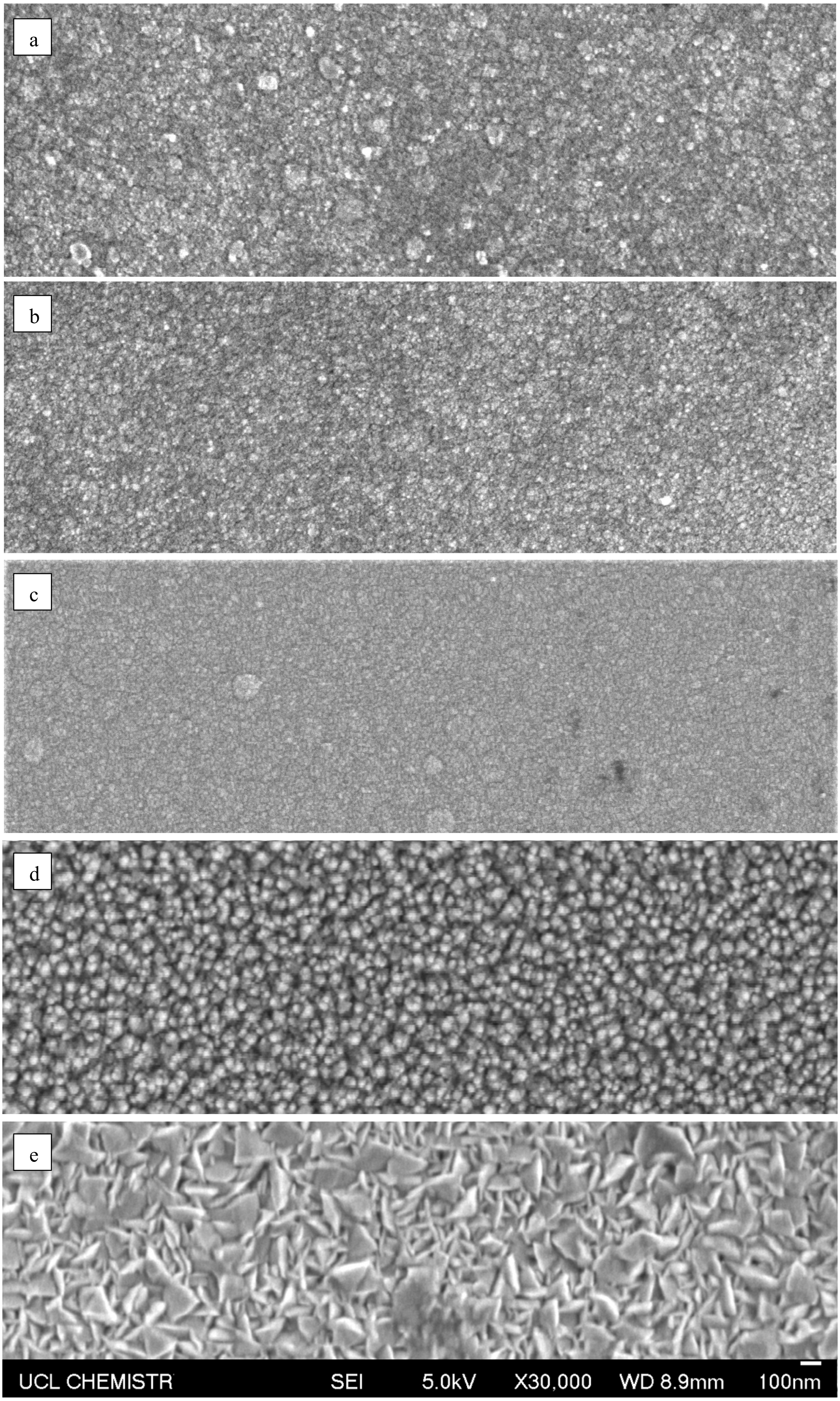

Figure 3.20 - Top view SEM images of ZnO thin films synthesised using precursor 2-H-M, DEZ with MeOH and Hexane grown at a) 300°C b)350°C c) 400°C d)450°C e)500°C

Top view SEM images of the thin films made using diethyl zinc in a dual source deposition with Toluene and MeOH have been presented in Figure 3.21 in order of increasing deposition temperature. Image a show the top view SEM image of the thin film made at 300°C. Small particle sizes are seen in this image with little crystal growth, which is representative of an amorphous film, as supported by the XRD of the film in Figure 3.7.

At a higher deposition temperature of 350°C an increase in particle size is seen and an improvement in the crystallinity of the film is seen however the film remains heterogeneous. In image C, a more homogeneous thin film with directional growth is seen in the top view SEM image. At 450°C the thin film in image D shows a very compact film produced with the formation of shallow wedge like surface crystals. This is in concordance with the XRD measurement of the thin film seen in Figure 3.7 where the peaks of the crystal planes intensify and sharpen indicating a highly crystalline film.

Image e in Figure 3.21 shows the top view SEM image taken of the thin film deposited at 500°C, here larger and sharper wedges are seen on the surface. The thin film has a compact structure with higher surface roughness as the higher deposition of 500°C enables the growth of larger crystals, seen in the crystallite estimations made using the Scherrer equation. This is characteristic of thin films deposited at 500°C using diethyl zinc in a dual source deposition with MeOH and Toluene as reported by Ponja *et al.* [67]

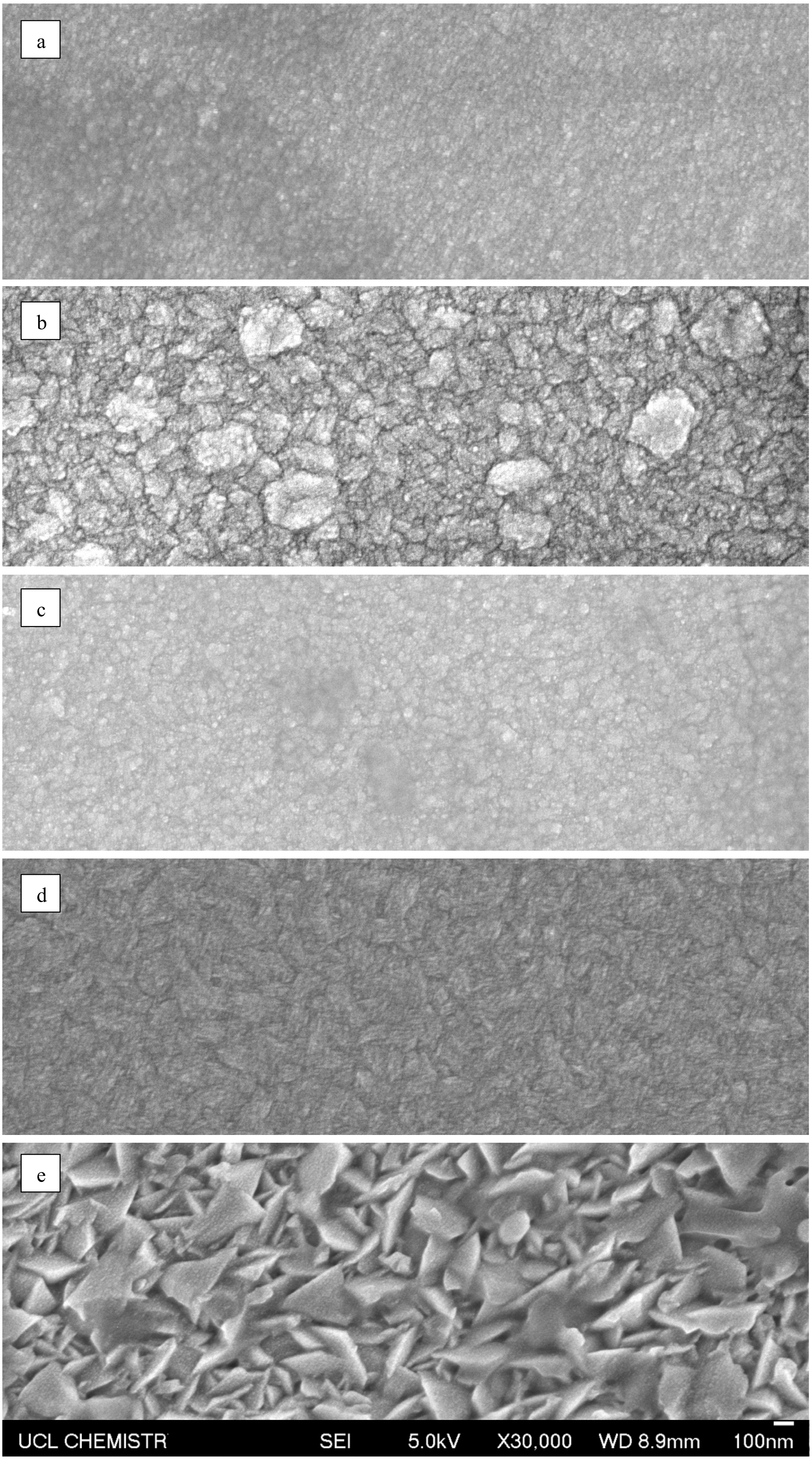

Figure 3.21 - Top view SEM images of ZnO thin films synthesised using precursor, 2-T-M, DEZ with MeOH and Toluene grown at a) 300°C b)350°C c) 400°C d)450°C e)500°C

Figure 3.22 displays the top view SEM images taken of the thin films made using diethyl zinc in a dual source deposition with Hexane and IPA grown between 300°C -500°C. Image a show the film grown at the lowest deposition temperature of 300°C, small but crystalline particles are seen in the image. This is in correlation with the XRD measurement of the film where a crystalline film is seen with growth in the (100) and (002) planes. Image b shows the thin film grown at 350°C where a compact thin film with a particle like surface is observed suggesting there is some degree of amorphousness in the film. At 400°C in image c, a more directional and compact film is seen with the formation of more defined particles.

At a higher deposition temperature of 450°C, a very directional and crystalline thin film is observed with a much flatter surface. This is consistent with the crystal structure of the thin film in Figure 3.10 where the XRD measurements of the thin film shows highly directional film in the (002) plane. At 500°C the thin film has a heterogeneous surface with the formation of larger wedges and block shaped particles. This is also seen in the crystal structure of the film with crystal growth seen in other crystal planes such as 100 and 101.

Up until a deposition of 450°C, growth in the (002) planes has dominated in the thin films making highly directional films. The increased energy at a deposition temperature of 500°C has enabled the growth of non-polar planes, giving rise to films with a rougher surface. Rough surfaces and polycrystalline growth are unwanted in thin films for TCO applications, as this results in increased grain boundaries that can hinder mobilities and reduce conductivity in the films.

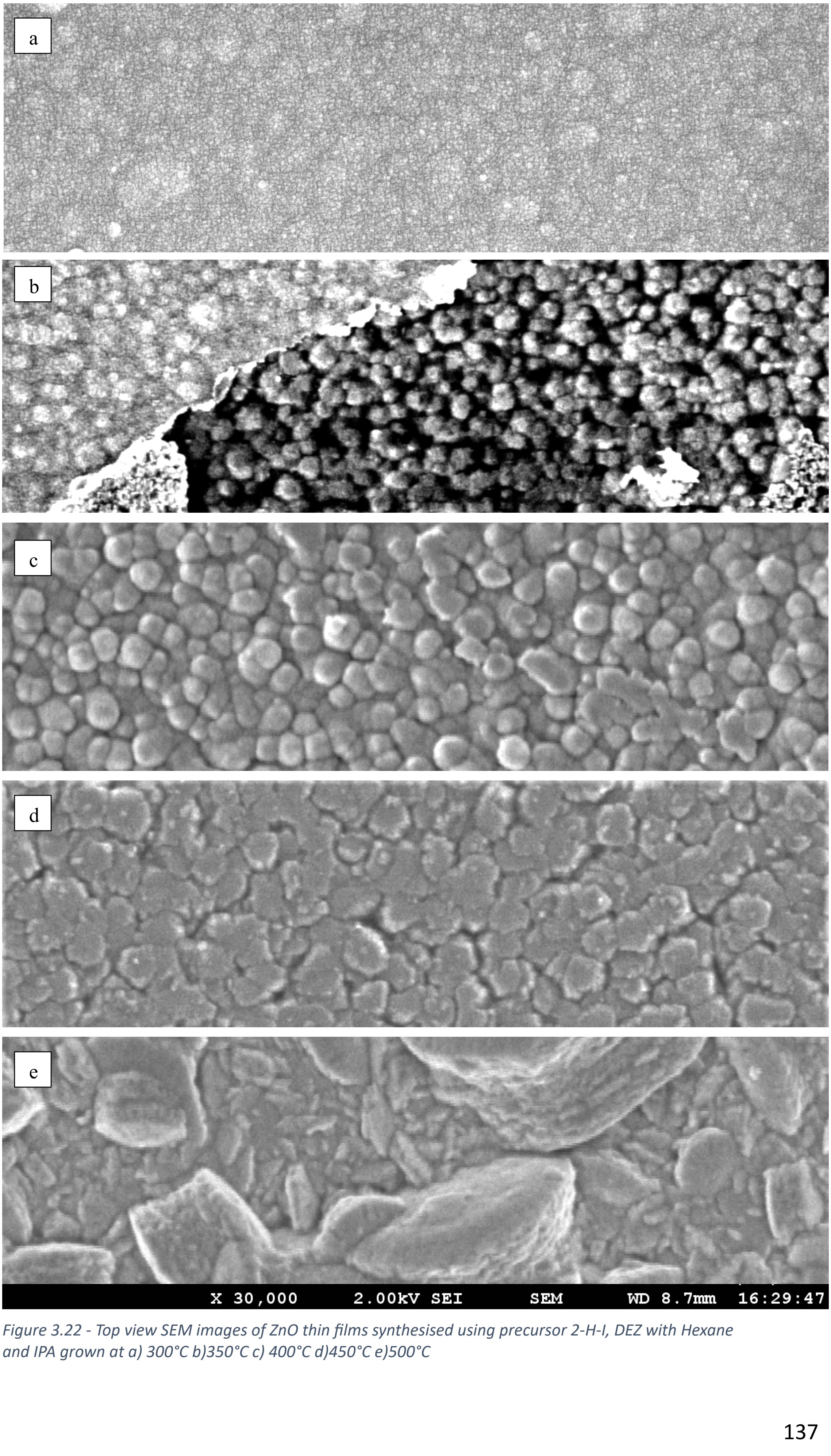

Figure 3.22 - Top view SEM images of ZnO thin films synthesised using precursor 2-H-I, DEZ with Hexane and IPA grown at a) 300°C b)350°C c) 400°C d)450°C e)500°C

The series of images presented in Figure 3.23 displays the top view SEM images taken of ZnO thin films grown using diethyl zinc in a dual source deposition with Toluene and IPA from 300°C to 500°C. Notably the first SEM image (a) of the ZnO thin film grown at 300°C appears to have bigger sized particle when comparing with the same film grown at 300°C in Figure 3.22a but with Hexane instead of Toluene. This film also has more directional growth in the (002) plane whereas the thin film grown with Hexane has more growth in the (100) plane.

At 400°C the surface morphology of thin film is seen to have round particles with wedge formation and directional growth in blocks. These features are even further defined at a higher deposition temperature of 450°C where large crystallites are observed with vertical growth of hexagonal towers. The thin film grown at 500°C in image e, shows the expansion and growth of the crystals in the film into larger blocks and wider plates in the (002) direction. The increase in crystallite sizes observed in the microscopy is further supported by the crystallite size calculations.

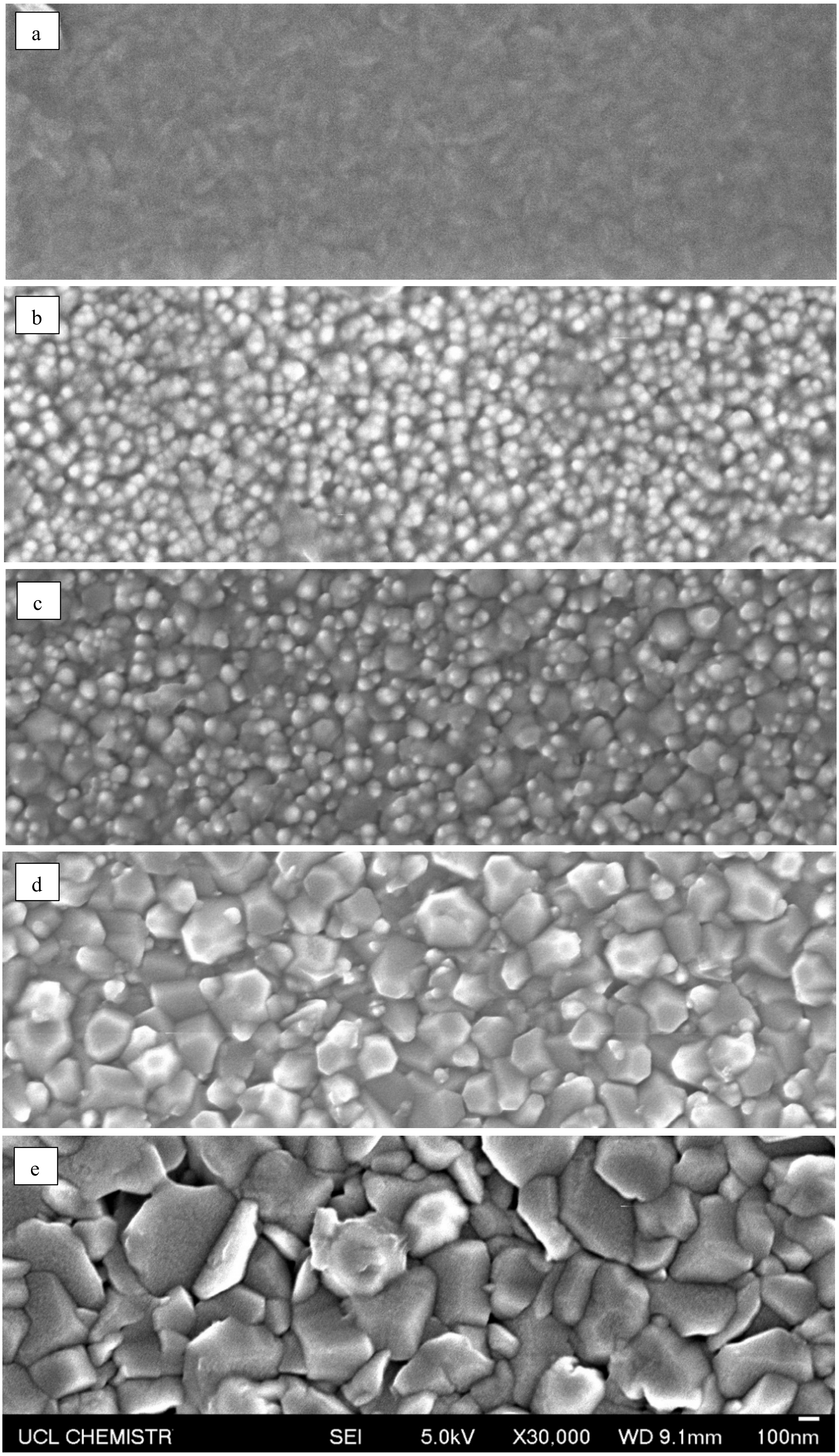

Figure 3.23 - Top view SEM images of ZnO thin films synthesised using precursor 2-T-I, DEZ with Toluene and IPA grown at a) 300°C b)350°C c) 400°C d)450°C e)500°C

3.5.3 Optical Properties

UV- Vis spectroscopy was used to determine the optical properties of the ZnO thin films between wavelength ranges of 200-1500nm. Tauc plots were derived from the transmittance data using the following equation:

$$(\alpha hv)^n = B\left(hv - E_g\right)$$

The Tauc plots were generated by plotting the square of $(\alpha h\nu)$ against the photon energy (hv), where B is a constant and E_g represents the optical band gap. The value of n indicates the nature of the transition, with n = 2 for direct allowed transitions and n = ½ for indirect allowed transitions. By plotting $(\alpha h\nu)^n$ against $h\nu$, and extrapolating the steepest part of the curve to the x-axis, an estimation for the value of E_g can be obtained. In some cases, two transitions are observed in the Tauc plots and this is explained in the relevant data later.

ZnO has a direct band gap, and therefore, when calculating the Tauc relation for deposited ZnO thin films, the exponent value of n = 2 is used. It is important to note that estimations of band gaps using the Tauc method was first developed in 1968 for amorphous semiconductors like Si and Ge.[77] However, in 1986, Hamberg & Granqvist discovered that TCOs, with their high electron density, cause frequent collisions and scattering of electrons upon photon absorption.[78] This broadens the photon absorption energy and the Tauc assumes that electrons can absorb photons without needing to conserve momentum, this assumption may not hold in crystalline materials.[79] As such correction methods for the widely adopted Tauc plot have been developed to find the corrected bandgap.

Implementing this correction method by Poeppelmeier *et al.* has given band gap values that closely align with those obtained through other techniques.[80] Previously, it has been used to ascertain the band gap of ZnO, finding values of Eg = 3.37 eV via spectroscopic ellipsometry[81], 3.37 eV through photoluminescence[82], and 3.41 eV using hybrid DFT [83]. However, employing the uncorrected 'traditional' Tauc approach yielded only 3.28 eV. Application of the correction resulted in Eg^{corr} = 3.34 ± 0.03 eV for ZnO[84]. However, for the purpose of this thesis and for ease of comparison of bandgap values the tauc plot has been employed to find the E_g of ZnO thin films.

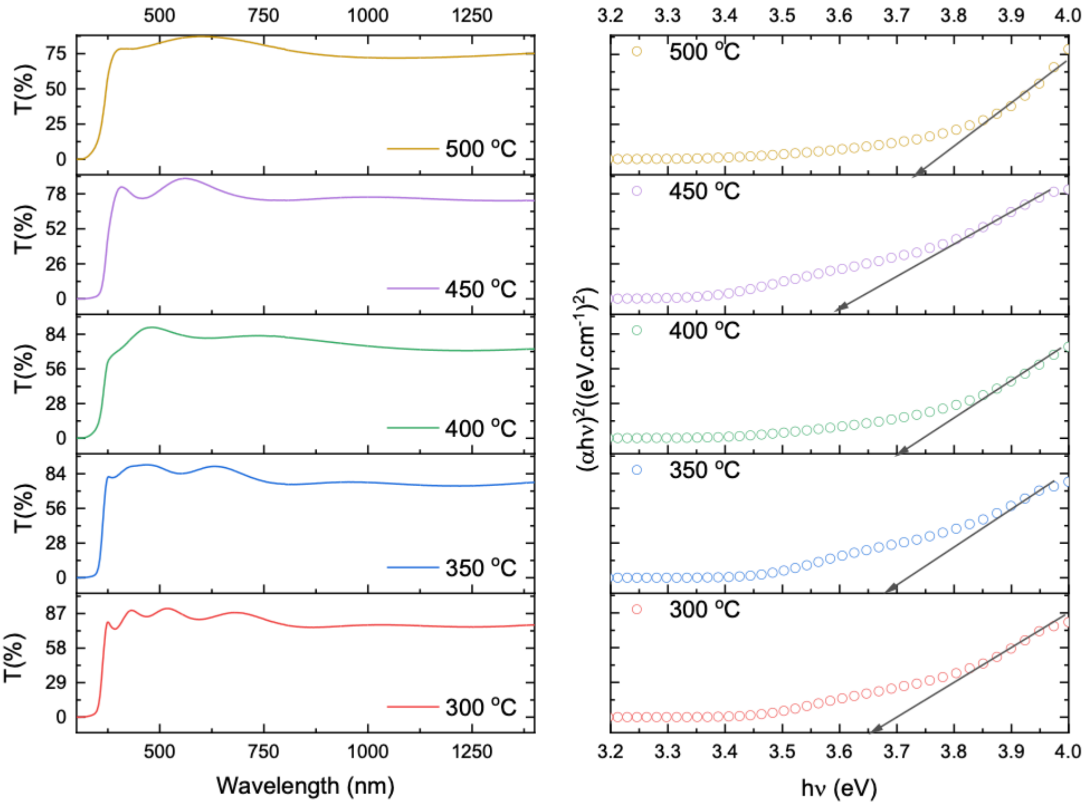

Sample	300°C	350°C	400°C	450°C	500°C
$T_{\lambda 550}$/ %	87	84	83	89	86
$T_{\lambda(400-700)}$/ %	86	88	83	82	84

Figure 3.24 – Optical transmittance spectra (left) and Tauc plots (right) for Zinc Oxide films grown using precursor 2-H-M, DEZ in Hexane with MeOH

The thin films grown using precursor 2-H-M, DEZ in Hexane with MeOH maintain a high transparency above 80% for all samples at both T_{550} and T_{vis}. In general, the ZnO thin films appeared to have a greater brown tint at higher deposition temperatures this could be due to the thicker films grown causing carbon contamination to be more visible at these temperatures. For films grown between 300°C to 400°C, a larger than expected bandgap of around 3.65 to 3.7eV is absorbed and the optical bandgap appears to be blue shifted. The prevalent amorphous phase found in ZnO films deposited at low temperatures is thought to be the primary cause of the blueshift observed in the optical band gap. Similar observations have been made in other studies of ZnO thin films grown via CVD in which the blueshift of the optical bandgap is believed to be caused by the presence of the amorphous phase ZnO.[85] This is further supported by the XRD pattern of the thin films whereby lower crystallinity of the thin films is seen at lower temperatures and the formation of partially amorphous ZnO can affect the optical properties as suggested by other studies.[86] [87]

An error of ± 0.2eV is estimated with the band gap calculations this is owed to the assumptions made in the tauc plot and from the step size used when measuring the UV-Vis data.

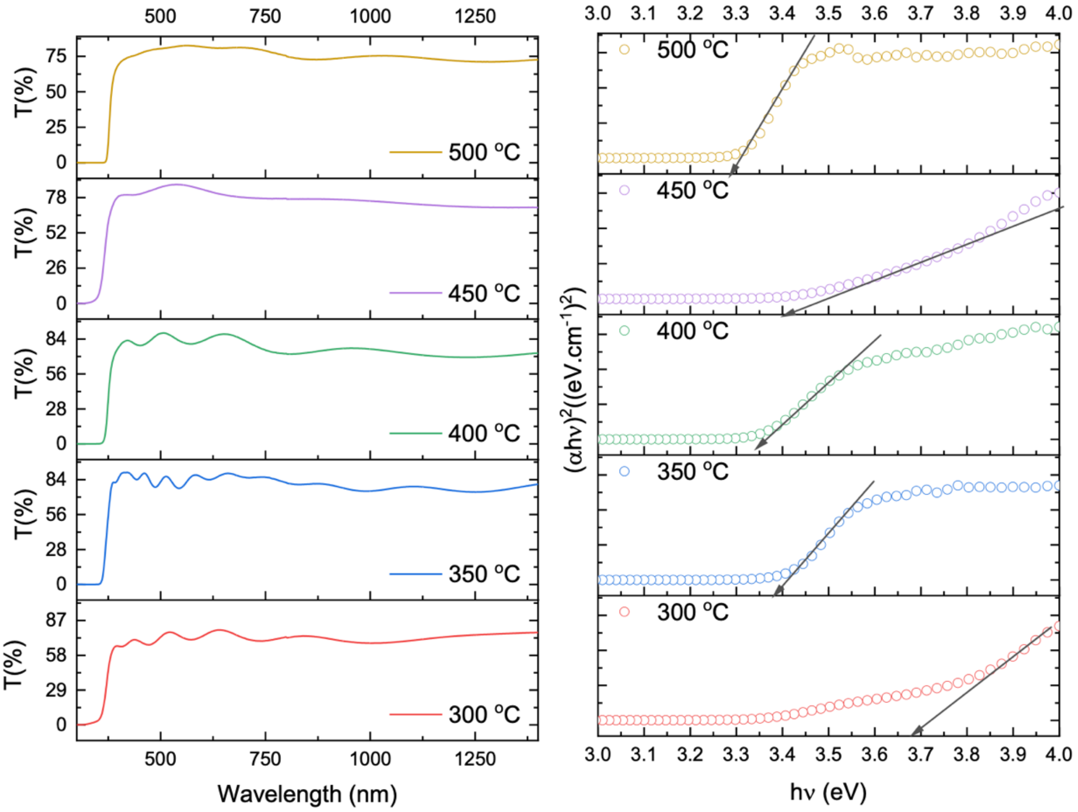

Sample	300°C	350°C	400°C	450°C	500°C
$T_{\lambda 550}$/ %	73	78	82	87	82
$T_{\lambda(400-700)}$/ %	73	85	84	83	80

Figure 3.25 - Optical transmittance spectra (left) and Tauc plots (right) for Zinc Oxide films grown using precursor 2-T-M, DEZ in Toluene with MeOH

UV-Vis spectra of the ZnO thin films grown using precursor 2-T-M, DEZ in Toluene and MeOH has been measured up to a wavelength range of 1500nm. Thin films grown above 400°C had a transmittance value above 80% at 550nm. At lower deposition temperatures the transmittance values at 550nm were 73% at 300°C and 78% for the ZnO film grown at 350°C. On average the transmittance value across the visible spectrum (T_{vis}) for films grown above 350°C have a transmittance value of at least 80%.

The bandgaps of the films were determined using the tauc plot method explained earlier and the bandgaps ranged between 3.7eV for ZnO grown at

300°C and 3.32eV at 500°C. A blueshift is evident in the thin film grown at 300°C, attributed to the presence of an amorphous phase of ZnO, as supported by XRD data illustrated in Figure 3.7.[88] The shallow transition observed in the film grown at 300°C with an intercept of ~3.3.eV can be attributed to the crystalline ZnO phase present in the film. Hence, as deposition temperature of ZnO thin films rises, a redshift in the bandgap becomes apparent, correlating with the enhancement in the film's crystallinity.

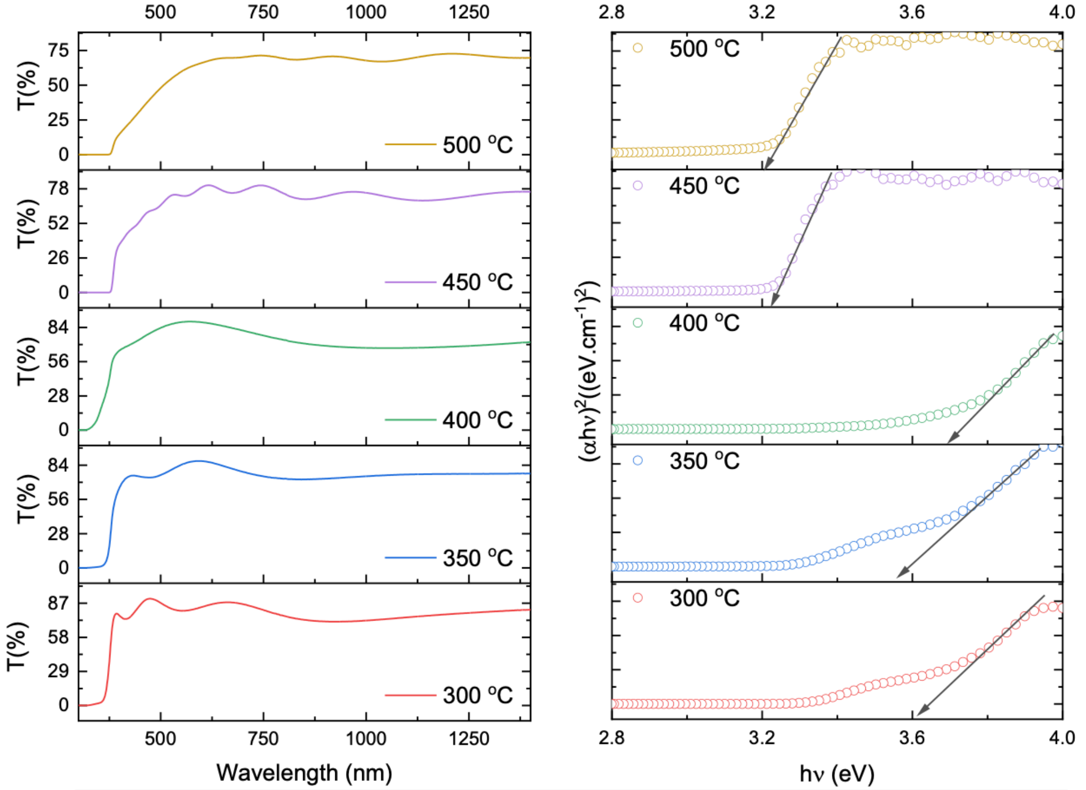

Sample	300°C	350°C	400°C	450°C	500°C
$T_{\lambda550}$/ %	81	85	89	73	61
$T_{\lambda(400-700)}$/ %	84	80	83	69	54

Figure 3.26 - Optical transmittance spectra (left) and Tauc plots (right) for Zinc Oxide films grown using precursor 2-H-I, DEZ in Hexane with IPA

UV-Vis spectra were obtained for ZnO thin films grown using the precursor 2-H-I, DEZ in hexane and IPA and has been plotted above in increasing deposition temperature. Overall, the transmittance of the ZnO thin films grown at temperatures between 300°C to 450°C had a transmittance of 80% or above at both 550nm and T_{vis}. However, at higher deposition temperatures above 450°C the transmittance dropped below 75% and the films appeared to have a dark brown tint. The darkening of the films at higher deposition temperatures can be explained by the thicker films grown which increase the visibility of carbon contamination in the thin film to the naked eye.

The bandgaps of the films were found to be between 3.29 eV for ZnO grown at 500°C to ~3.7eV for the film grown at 400°C. The ZnO thin films grown at lower temperatures of 300°C and 350°C appear to have two transitions; a sharp transition at ~3.7eV and a shallow transition at approximately 3.3eV which indicates the partial amorphous nature of the films resulting in the blueshift of the bandgaps at lower deposition temperatures.[87]

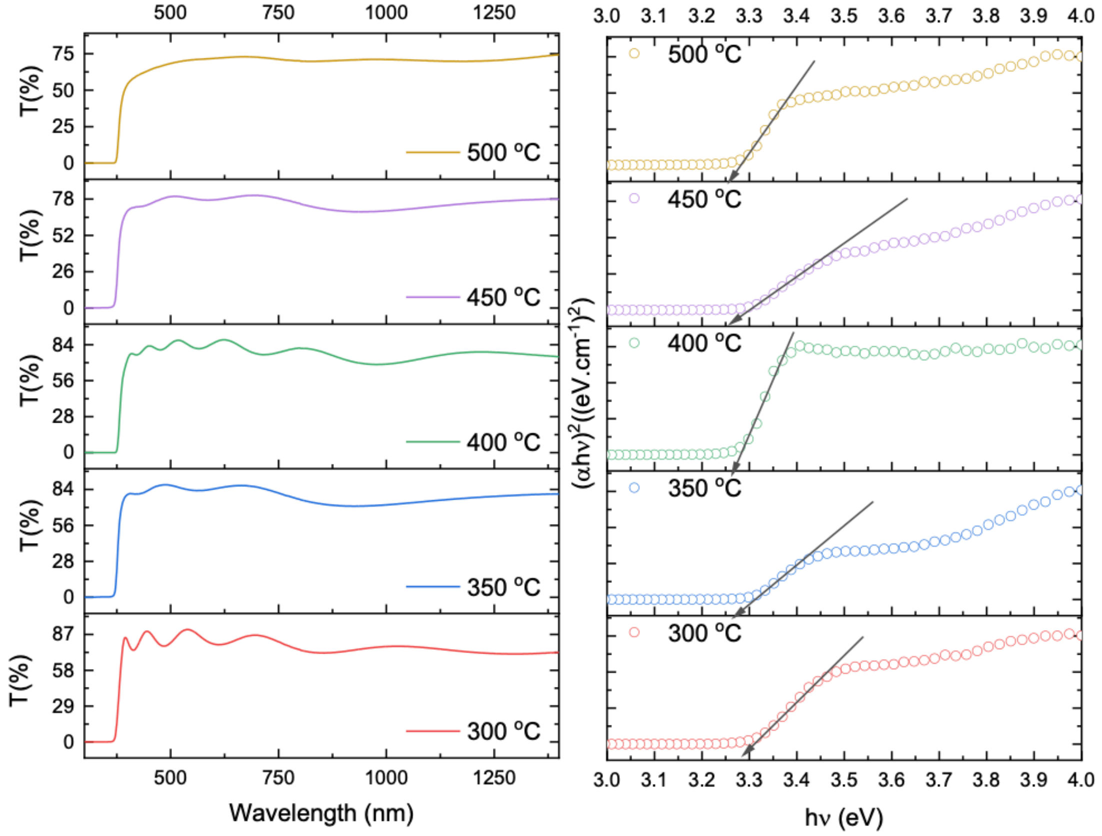

Sample	300°C	350°C	400°C	450°C	500°C
$T_{\lambda 550}$/ %	90	83	82	78	71
$T_{\lambda(400-700)}$/ %	83	85	82	78	69

Figure 3.27 - Optical transmittance spectra (left) and Tauc plots (right) for Zinc Oxide films grown using precursor 2-T-I, DEZ in Toluene with IPA

UV-Vis spectroscopy was employed to analyse the optical characteristics of the ZnO thin films within the wavelength range of 200-1500nm. The thin films were grown using precursor 2-T-I, DEZ in toluene with IPA, and exhibited highly transparent films exceeding 80% at 550nm and across the visible spectrum T_{vis} for films deposited up to 450°C. At 500°C the transmittance was found to be lower with a measured transmittance value of 71% at 550nm and averaged 69% across T_{vis}. Similar decrease in transparency has been observed across all the ZnO films grown at higher deposition temperatures regardless of the precursor combination used. A more pronounced brown hue was also seen with films deposited at higher deposition temperatures. This is likely due to the films being thicker and therefore the carbon contamination being more visible to the naked eye. This is further supported by the thickness measurements of the films reported later in Table 4 whereby films deposited at higher temperatures were found to be thicker, explaining the lower transmittance spectra obtained in UV-Vis. The band gaps of the ZnO thin films were found to be in concordance with literature values ranging between 3.26eV – 3.28eV for all 5 thin films.[89]

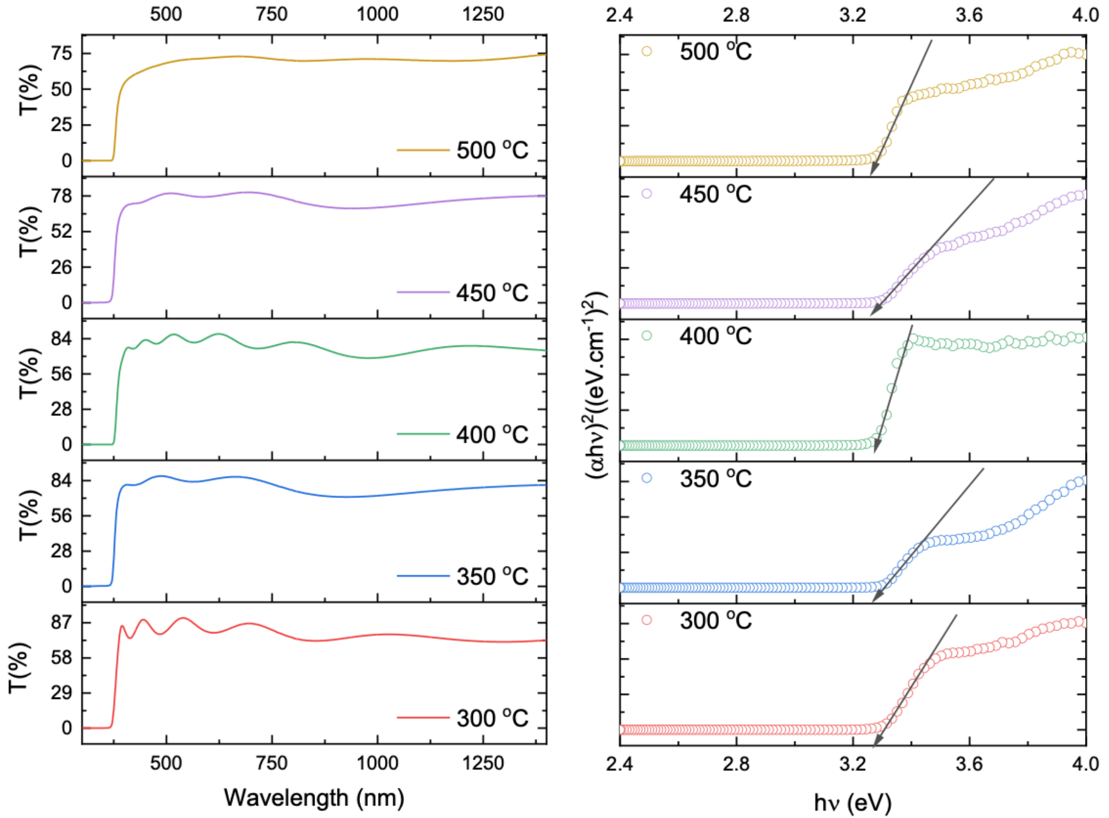

Sample	300°C	350°C	400°C	450°C	500°C
$T_{\lambda550}$/ %	90	83	80	76	72
$T_{\lambda(400\text{–}700)}$/ %	84	87	81	79	68

Figure 3.28 - Optical transmittance spectra (left) and Tauc plots (right) for Zinc Oxide films grown using precursor 3, EZI, ethyl isopropoxide

ZnO thin films grown using precursor 3, EZI exhibited excellent transparency in the visible range (400-700nm) surpassing the required threshold for commercial applications whereby transmittance of atleast 80% was achieved for thin films grown up to 450°C. In line with this the thin films grown using precursor 3 also appeared to be more highly transparent with no brown hues observed observed in the thin films at higher deposition temperatures. This observation could be explained by the clean decomposition path of precursor 3 which could minimise contamination in the ZnO thin films enabling the growth of highly transparent films. As seen in previous data at a higher deposition temperature of 500°C the transmittance at 550nm was lower and found to be 72%.

Moreover, at higher wavelengths, the transmittance of the films tended to decrease, indicating higher absorption of infrared light compared to visible light. The bandgaps of the ZnO thin films were found using the Tauc plot method described earlier. Thin films from precursor 3 showed consistently close band gap values, ranging from 3.29 to 3.31 eV.

3.5.4 Elemental Analysis

X-ray photoelectron spectroscopy was utilised to determine the oxidation states of Zn and O and thereby confirm the presence of these elements in all of the films made using the 3 different precursors. The XPS data was modelled using CasaXPS and the data was calibrated using adventitious carbon as a reference, with a carbon 1s peak at a binding energy of 285.0 eV. The films grown at 450°C for each of the precursor and or precursor combinations was further etched under argon for 200s to evaluate the surface and bulk properties of the ZnO thin films. The survey spectra indicated the presence of carbon, oxygen and carbon in all films. C contamination of the thin films were also assessed by comparing the peak areas of C1s to the combined peak areas of C1s and Zn 2p to estimate a percentage.

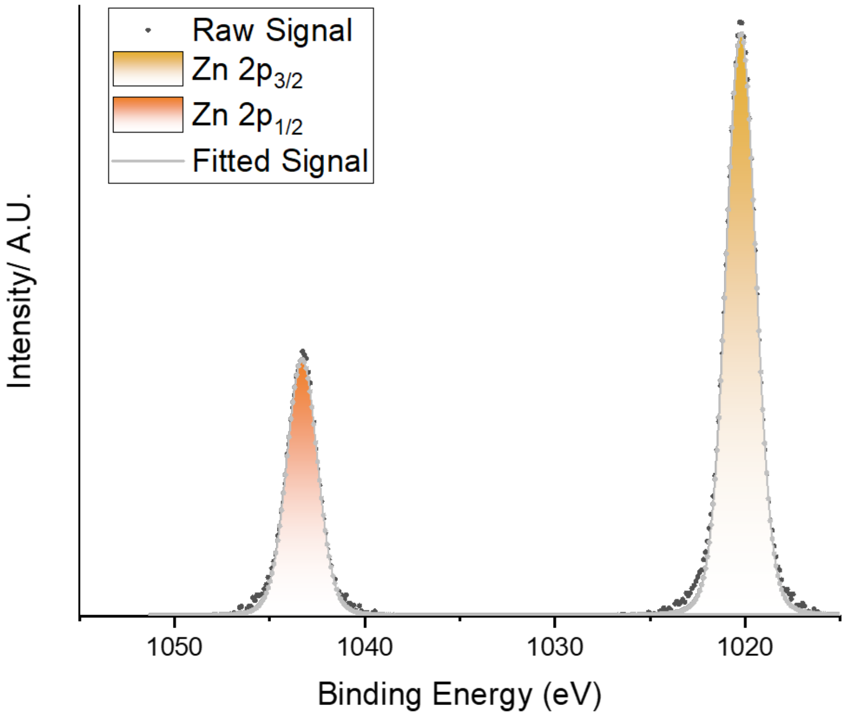

Figure 3.29 - XPS spectra of Zn2p peaks of ZnO thin film grown at 450℃ using precursor 3

Figure 3.29 illustrates a surface XPS scan with high resolution in the Zn 2p orbital region (1050-1010 eV) for a ZnO thin film grown using precursor 3, EZI. Only one sample is shown here as the pattern observed is consistent across all the analysed ZnO samples made using different precursors. The spectrum exhibits a doublet in this region, indicating the presence of two distinct binding energy states for the Zn 2p orbital, namely $2p_{1/2}$ and $2p_{3/2}$.

The observed peak splitting in the Zn 2p orbitals region is a consequence of spin-orbit coupling, which occurs when the spin of an electron interacts with the magnetic field generated by its motion. This interaction causes the 2p orbital to split into two distinct orbitals: the $2p_{1/2}$ orbital and the $2p_{3/2}$ orbital. The $2p_{1/2}$ orbital has a lower energy compared to the $2p_{3/2}$ orbital, which means that more energy is required to remove an electron from the $2p_{1/2}$ orbital. As a result, the $2p_{1/2}$ peak appears at a higher binding energy than the $2p_{3/2}$ peak in the XPS spectrum. The 2p orbitals were examined for Zn and the O1s for O.

The splitting of the zinc 2p peaks consistently measured around 23.1 eV, with peak positions of 1020.7 eV (± 0.2 eV) and 1043.8 eV (± 0.2 eV) for the $2p_{3/2}$ and $2p_{1/2}$ orbitals for the ZnO thin films. These peak positions can be attributed to the Zn^{2+} oxidation state in the ZnO material, confirming the presence of zinc in all the films.

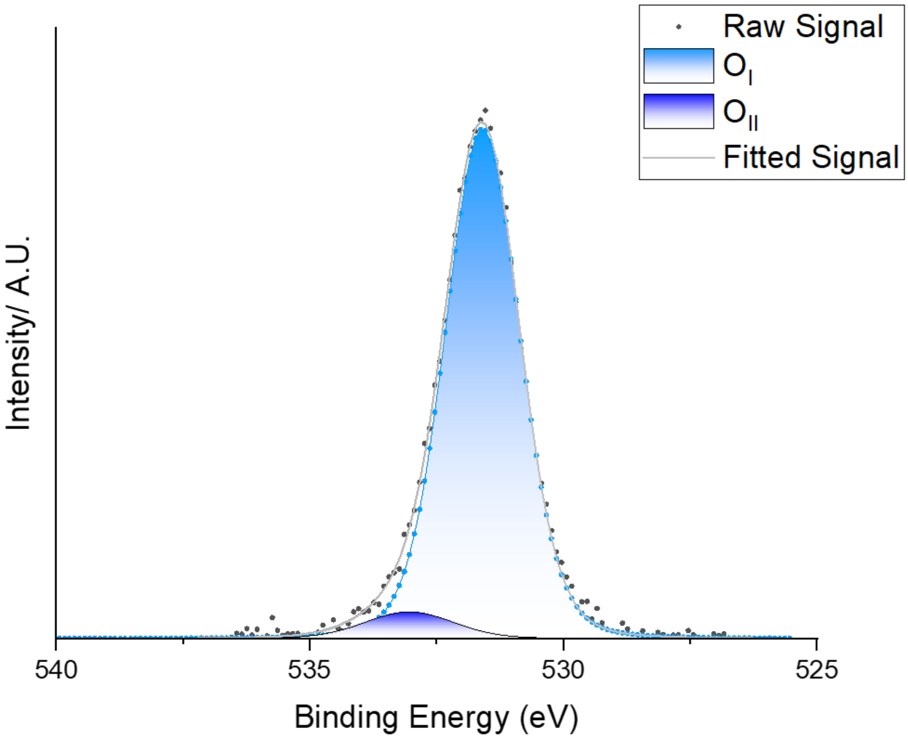

Figure 3.30 - XPS spectra of O1s peaks of ZnO thin film grown at 450℃ using precursor 3

The oxygen O1s peak observed in the ZnO films could be deconvoluted into two distinct peaks: OI and OII with binding energies of 530.9 eV (± 0.2 eV), and 532.7 eV (± 0.2 eV), respectively (as shown in Figure 3.30). All the measured values align with known binding energies associated with Zn^{2+} in the Zn-O environment of ZnO. This consistency further validates the XRD results obtained earlier to confirm the presence of wurtzite ZnO. The OI peak, being the most prominent, can be attributed to O^{2-} ions within the ZnO structure. The OII peak corresponds to O^{2-} ions situated in regions of oxygen deficiency within the ZnO material which indicates the concentration of oxygen vacancies and surface-bound oxygen species. The surface-bound oxygen species can include O^{2-} and H_2O.

Upon etching under argon for 200s, it was observed that the intensities of the OII peaks significantly diminished within the bulk of the ZnO films. This suggests that the etching process effectively removed surface-bound impurities and implies a lower concentration of oxygen vacancies within the bulk compared to the film's surface.

Quantitatively estimating the oxygen content of films deposited on glass is challenging because analytical techniques may also consider the oxygen content of the substrate. Therefore, drawing conclusions about the effect of oxygen content on the optoelectronic properties of these films and relating it to the oxygen content of the precursor may not be useful or valid.

It is also worth mentioning for films grown using precursor 2, diethyl zinc in a dual source deposition, a lower surface oxygen content was observed compared to the other films. This difference can be attributed to the use of diethylzinc, which has a Zn/O ratio of 1:0. Thus, it can be suggested that no oxygen from the precursor or ligand was bound at the surface in these films.

X-ray photoelectron spectroscopy was used to compare the bulk and surface properties of the ZnO thin films. The films grown at 450°C for all the precursor combinations were assessed to determine the carbon contamination in the films, tabulated below.

Table 3 - Carbon contamination of ZnO thin films grown at 450 using all 3 precursor combinations

Precursor	Deposition Temperature/ °C	Carbon contamination/ %
Precursor 1, $Zn(acac)_2$	450	17.6
Precursor 2-H-M	450	8.9
Precursor 2-T-M	450	8.0
Precursor 2-H-I	450	12.8
Precursor 2-T-I	450	9.5
Precursor 3, EZI	450	8.7

All the ZnO thin films grown using various precursors were found to have higher carbon contamination on the surface which is likely due to the handling of the films. Upon etching the carbon contamination was found to be lowered for all the ZnO thin films analysed, indicating that contamination was mainly limited to the surface.

Thin films grown using precursor 1, $Zn(acac)_2$ were seen to have the largest carbon contamination on the surface of the ZnO thin films. $Zn(acac)_2$ is known to have a larger organic content in comparison to precursors 2 and 3 which makes it less likely to have a clean decomposition path and thus leave behind unwanted impurities on the films.[75] This also correlates with the pronounced brown hue observed on the deposited thin films grown using this precursor.

Other studies made similar observations and have also found $Zn(acac)_2$ more likely to have carbon contamination in the films.

In comparison thin films grown using precursor 2, diethyl zinc with the various hydrocarbon and alcohol solvent combinations resulted in thin films with less carbon contamination. This suggests a more facile decomposition of the precursor minimising the impurities found on the surface of the films. Thin films grown using 2-T-M was found to have the least carbon contamination around 8% on the surface. In general, when using hexane as the hydrocarbon solvent, higher carbon contamination was observed in the films when compared with films grown with toluene. This correlation is in accordance with the UV-Vis spectra for these thin films where lower optical transmittance was found for films grown using hexane as the hydrocarbon solvent in a dual source reaction with precursor 2.

Precursor 3 was determined to have a carbon contamination of 8.7% which is lower than most of the ZnO thin films grown using the other precursors discussed above. The much lower organic content (approx. 45% less than precursor 1) of this SSP enables a cleaner decomposition path[75]. EZI is believed to undergo a β-H elimination process which enables the formation of volatile organic by-products that can easily be passed out through the exhaust. This process reduced the likelihood of by-products contaminating the thin film.

Based on this experimental evidence it can be inferred that an increased carbon content in the ligand of the precursor directly correlates with a higher proportion of carbon in the resulting films.

AACVD deposition on ZnO thin films using a single source precursor by Joe *et al.* has also reported the organic ligand attached to zinc complex and it's decomposition path can have a significant effect on the carbon contamination of the thin film.[90] Thus, it is favourable to use precursors with reduced organic content that have clean decomposition paths and form volatile organic by-products which can significantly reduce contaminants and yield thin films with superior properties.

3.5.5 Electrical Properties

Hall effect measurements were carried out using the Van der Pauw method to determine the electrical properties of the ZnO thin films at room temperature. The measured values for resistivity (ρ), carrier concentration (n), mobility (μ), T_{550}/ % and thickness (d) for each film have been tabulated below for films which showed sufficient conductivity. Using these values the R_{sh}/ $\Omega\ \square^{-1}$ and F.o.M. (figure of merit) values for the ZnO thin films produced in this chapter has been determined and discussed.

The Haacke figure of merit (FOM) compares the average transmittance *(λ)* = 550 nm ($T_{\lambda 550}$) of a material to its sheet resistance, providing a good initial assessment of the film's TCO performance. However, it is important to note this method overlooks important factors like the material's band gap, which can limit its usefulness in certain applications.

Table 4 - Carrier concentration (N_b), Hall mobility (μ), resistivity (ρ), thickness (d), sheet resistance (R_{sh}), average transmittance at λ = 550 nm ($T_{\lambda 550}$) and figure of merit (F.o.M.) for ZnO films grown in Chapter 1

Precursor Name	**Deposition Temperature/ °C**	**d/ *nm***	**n/ $x10^{19}$ cm^{-3}**	**μ/ $cm^2V^{-1}s^{-1}$**	**ρ/ $x10^{-3}$ Ωcm**	**R_{sh}/ Ω □$^{-1}$**	**T_{550}/ %**	**F.o.M/ $Ω^{-1}$**
Zn(acac)2	450	320	1.65	0.64	3.44	107.5	77	0.72
2-H-M	500	450	6.88	5.65	3.12	69.3	86	1.24
2-T-M	400	250	9.53	13.63	3.44	137.6	82	0.60
2-T-M	450	250	19.88	11.77	3.56	142.4	87	0.61
2-T-M	500	600	3.53	19.99	3.33	55.5	82	1.48
2-H-I	350	600	0.58	4.19	3.24	54.0	85	1.57
2-H-I	400	595	1.03	34.21	3.26	54.8	89	1.62
2-H-I	450	600	4.19	22.82	3.14	52.3	73	1.39
2-T-I	400	260	1.03	31.32	2.86	110.0	82	0.75
2-T-I	450	600	2.33	22.99	2.76	46.0	78	1.70
2-T-I	500	600	1.51	24.00	2.99	49.8	71	1.42
3	350	580	0.87	7.32	2.12	36.6	83	2.27
3	400	610	1.14	20.36	2.14	35.1	82	2.34
3	450	550	4.68	25.6	2.32	42.2	78	1.85
3	500	560	4.93	23.79	2.43	43.4	71	1.64

Amongst the thin films grown at different temperatures using precursor 1, $Zn(acac)_2$, only one film grown at 450°C was conductive enough to carry out Hall effect measurements. All the other thin films grown using precursor 1 were highly resistive and their electrical measurements could not be measured using Hall effect accurately. This film was found to be the highly resistive with a resistivity value of 3.44 Ωcm and a low F.o.M. value of 0.72.

The XRD pattern of the thin film grown at 450°C using precursor 1 shows a highly oriented thin film in the c-axis with the highest T/C value of 5.7 in (002) plane and minimal growth in other crystal planes. Thus, by analysing the crystallographic structure of the thin films grown using precursor 1, conductivity of the thin film is closely related to the crystal structure of the thin film. Highly oriented thin films can promote better electrical conductivity in thin films as seen in the series of thin films deposited using precursor 1, $Zn(acac)_2$ in which the highly oriented thin film grown at 450°C was found to be the most conductive. However, the large organic content of this precursor results in greater contamination from organic species on the ZnO thin films resulting in highly resistive films that were not conductive enough to measure electrical properties. Combined with the difficulties of using this precursor to deposit ZnO thin films we can conclude that this precursor is not ideal to deposit ZnO based thin films.

Similarly using precursor 2-H-M, only 1 film grown at 500°C was conductive enough to conduct Hall effect measurements. This was expected as the thin films grown using this precursor were seen to have poor crystallinity which can lead to poor conductivities. Films grown using this precursor exhibited the lowest T/C values in crystallographic planes and the films grown at lower deposition temperatures were found to be highly amorphous. Further to this the Zn:O of 1:0 in the precursor used results in an oxygen deficient environment during nucleation. This favours the growth of non-polar planes, as seen by the XRD measurements for these films. Resulting in the growth of multiple crystallographic planes which can increase grain boundaries in the film and therefore deteriorate the mobilities of charge carriers and thus conductivity.

Thin films grown using precursor 2-T-M displayed better electrical properties above a deposition temperature of 400°C. The highest carrier concentration and lowest mobilities were measured for the thin film grown at 450°C using this precursor. The measured electrical properties align with the crystallography of the thin films, above 400°C the thin films exhibit higher quality thin films with increased crystalline character. Thin films grown at higher temperatures often exhibit better crystallinity due to enhanced diffusion and increased energy of the adatoms. The increase in mobility and diffusion of atoms facilitates the movement and rearrangement of atoms during film growth, allowing for better crystalline ordering and larger crystal sizes.

Thin films grown using 2-T-M exhibits polycrystalline growth and favours growth in non-polar planes such as (100) and (101) plane. In order to achieve efficient charge transport and lower electrical resistance in thin films, near to monocrystalline growth is required to minimise the effects of grain boundaries and defects on electrical properties. Further to this polycrystalline growth can reduce transparency of thin films due to the increase in grain boundaries and scattering centres which can absorb light or further scatter light. Thus, for the reasons mentioned above and the cumbersome dual source AACVD deposition of precursor 2-T-M makes this precursor an unviable option.

ZnO films grown using precursor 2-H-I found to produce reliable results using Hall effect measurements for the film grown at a low deposition temperature of 350°C. In general, the films grown using this precursor exhibited higher conductivities. This observation aligns with crystal structure of the thin films which shows preferred orientation in the 002 plane for films grown up to 450°C.

Interestingly, the film grown at 500°C was found to be too resistive, and the electrical properties had deteriorated at this deposition temperature such that hall effect measurements could be taken. Taking a closer look at the XRD pattern for this film shows an increase in growth in multiple crystal planes and preferred orientation no longer remains in the 002 plane and instead preferred orientation is seen in the non-polar 101 plane. This further supports the idea that crystal growth in non-polar planes and multiple crystal planes can introduce grain boundaries, dislocations, or defects that can impede the flow of charge carriers and reduce conductivity of thin films. As such this type of growth is not desired in thin films grown for optoelectronic purposes.

The final set of thin grown using precursor 2, 2-T-I, DEZ in toluene with IPA in a dual source deposition exhibited higher mobilities and similar resistivities. Films grown above 400°C were conductive enough to carry our Hall effect measurements and determine electrical properties. This precursor combination yielded conductive ZnO thin films with preferred orientation in the 002 plane maintained across all deposition temperatures. The highly textured thin films and good electrical properties observed using 2-T-I demonstrates the growth of thin films which exhibit properties that are favoured for TCO applications.

However, the highly reactive and pyrophoric nature of precursor 2, DEZ, limits the feasibility of scaling thin film production due to the additional steps required to successfully and safely deposit ZnO thin films using this precursor.

ZnO films grown using the SSP, EZI or in this case referred to as precursor 3 consistently delivers thin films with good electrical properties as observed by the high conductivities and low resistivities measured for these films. Further to this higher carrier mobilities and F.o.M. values greater than 2 have been calculated for films grown at lower deposition temperatures of 350°C and 400°C suggesting good overall TCO performance for ZnO thin films grown using EZI. From the XRD patterns, preferred orientation is observed across all the deposited thin films in the 002 plane which can facilitate easier movement of charge carriers, resulting in higher conductivity.

Precursor 3 presents a non-hazardous and simple single source AACVD method to synthesise ZnO thin films without the need for additional steps like the dual source counterparts seen in precursor 2-T-I. This SSP precursor promotes the growth of thin films in the energetically favourable crystal plane 002 and contains all the required Zn-O bonds in its heterocubane structure. The desired Zn:O ratio of 1:1 in this precursor provides an oxygen rich environment that promotes growth in the polar plane and yields thin films with good optoelectronic properties as shown in this detailed study.

3.6 Conclusions

This study provides a comprehensive analysis of the correlation between three different precursors and the resulting thin films in AACVD reactions. The experimental findings offer compelling evidence linking the properties of the precursors to the optoelectronic characteristics of the thin films.

A series of three precursors with varying Zn/O ratio have been investigated in this chapter. Among them, two are commercially available precursors $Zn(acac)_2$ and diethyl zinc. The final precursor discussed is designed by Sanchez Perez *et al,* EZI, which is a single source precursor which has the optimum Zn/O ratio of 1:1.[64]

All ZnO thin films have undergone elemental analysis, crystal XRD, SEM and UV-vis spectroscopy. The three precursors have been employed in AACVD reactions to produce ZnO films with high purity. The resulting films have been subjected to standard analytical techniques for comprehensive characterisation.

Through these investigations, it has been demonstrated that the design and selection of precursors play a crucial role in determining the properties of the deposited films. This approach offers the opportunity to finely adjust the chemical environments during nucleation to achieve desired properties tailored for specific applications. By isolating the intermediate formed during the dual source AACVD reaction of diethyl zinc and IPA and forming a SSP with the desired Zn-O bonds preformed in the precursor yields highly conductive thin films that are closer to monocrystalline structures. The thin films exhibit optimal optoelectronic properties comparable to films produced in literature.

The influence of precursor design and choice on the film properties, particularly the preferred orientation observed in XRD analysis, has been established. Therefore, optimising the crystal structure and quality of thin films is essential for achieving higher conductivity and improving the performance of electronic and optoelectronic devices.

Moreover, it has been observed that a higher carbon content in the ligand leads to a greater carbon percentage in the resulting films. By conducting experiments with both single source and dual source reactions, it has been determined that direct metal-carbon bonds in the precursor and the oxygen environment around the Zn centres can impact the morphologies of the films and the resultant optoelectronic properties.

Single-source precursors provide an excellent pathway for thin film fabrication due to their inherent advantage: they contain all the necessary bonds for the thin film, typically in the desired stoichiometry. This characteristic provides several advantages, including the reduction of deposition temperature requirements and the ability to generate stoichiometric films.

Chapter 4 – ZnO seeding for epitaxial growth

This chapter investigates the use of ZnO thin films as seeding layers to epitaxially grow highly oriented ZnO thin films in the c-axis. The undoped ZnO thin films synthesised in Chapter 3 using different precursors all produced thin films with polycrystalline growth. Higher deposition temperatures increase adatom energy, promoting growth in higher surface energy crystal planes. The deposition of thin films on non-textured substrates such as glass also allows growth in multiple crystal directions and does not coerce crystal growth in a singular crystal direction. This leads to the growth of polycrystalline films with high roughness. The growth of polycrystalline thin films with such features for optoelectronic applications is not favourable, as this leads to increased resistance caused by grain boundaries resulting in reduced mobilities and thus lower conductivity in the films.

In order to achieve high performance optoelectronic properties, a compact and near-monocrystalline film is favourable to minimise resistivity and effectively increase conductivity. Thus, by directing crystal growth towards a singular crystallographic direction, for wurtzite ZnO, the polar crystal plane (002) with the lowest surface energy is favoured; thin films with near to monocrystalline structures can be obtained. Preferential crystal growth of this nature is known as “self-texturing” and requires good control over film thickness and morphology. [91]

Therefore, this chapter aims to produce thin films with near monocrystalline structure to minimise resistivities caused by grain boundaries and increase mobility and conductivity in ZnO based TCOs for optoelectronic applications. This is achieved through the promotion of crystalline growth in the 002-direction using ZnO seeding layers, deposited at low temperatures, for epitaxial growth of ZnO thin films.

Epitaxial growth usually requires the use of substrates such as c-silicon or Al_2O_3 which can be opaque and expensive, making it difficult to mass produce highly textured thin films. Epitaxial growth is also usually obtained using high temperatures and low growth rates as mentioned in the introduction chapter.

A study by Choopun *et al* reported the growth of smooth and epitaxial ZnO films through tuning the oxygen pressure at the initial and final growth stages to obtain films with high optical quality and electron mobility.[92] Following this two-step method, this chapter proposes the growth of a ZnO seeding layer as the initial step to promote the growth of c-axis oriented and fully crystalline ZnO thin films.

Thus, the findings presented in this chapter to grow highly textured ZnO thin films using c-axis oriented seeding layer grown at a low deposition temperature 350°C is a novel approach to achieve self-textured, uniform and densely packed ZnO thin films for optoelectronic applications. The work carried out in this chapter has been done in collaboration with Clara Sanchez-Perez. Whereby the seeding layer grown at 350°C was deposited by the author of this thesis and the subsequent ZnO layer grown on top was carried out by Clara Sanchez-Perez. The findings from this chapter are in submission to be published upon peer review satisfaction.

4.1 Introduction

It is well understood that thin films with near monocrystalline structure with low surface roughness and high purity are needed to achieve good optoelectronic properties in thin films. Thus, low-cost methods to attain highly compact and textured thin films are needed. The seeding layer approach described in this chapter to epitaxially grow c-axis oriented thin films demonstrates a novel method to efficiently achieve such properties.

4.1.1 Precursor

Following the precursor study in the previous chapter, the single source precursor EZI is employed to deposit both the seeding layer and the epitaxial layer on top. The pre-existent Zn-O bonds and preorganised Zn_4O_4 structure of the single source EZI precursor makes it ideal to deposit ZnO thin films as shown in Chapter 3. The seeding layer method presented in this chapter delivers highly oriented thin films in the 002-direction, carried out at low temperature depositions and removes the requirement for costly single crystal substrates.

4.1.2 Materials

Diethylzinc (DEZ) in anhydrous toluene (1.0 M, Acros Organics) and anhydrous isopropanol (IPA, Acros Organics) were employed for the synthesis of the ZnO precursors and thin films.

4.1.3 Film growth

A single source AACVD set up is employed to deposit both the seeding layer and epitaxial thin film on top. The novel single source precursor $[EtZnO^{i}Pr]_4$ is synthesised according to the instructions published by Sanchez-Perez *et al*.[64] Standard Schlenk technique under an argon atmosphere were employed to mix anhydrous toluene and DEZ, ensuring a moisture- and oxygen-free environment. The solution is then cooled down to - 78°C using a cold bath surrounding the Schlenk flask. Upon cooling down anhydrous IPA is added dropwise to form a cloudy solution. The cold bath is then removed, and the solution is left to stir and gradually warm up to room temperature. During this time, the AACVD reactor is switched on and heated up to the desired deposition temperature of 350°C. The isolated intermediate is dissolved in 15 ml of anhydrous IPA before being injected for deposition.

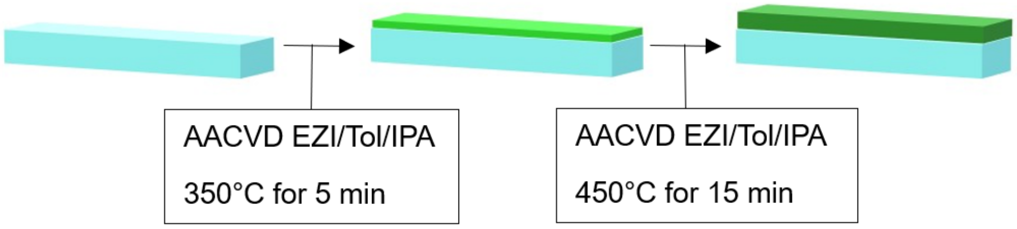

Figure 4.1 - Schematic showing seeding layer and epitaxial layer growth on top

Figure 4.1 above depicts the step-by-step deposition of the seeding layer and epitaxial ZnO thin film grown on top. The first step is the growth of the initial seeding layer at 350°C; this deposition is left to run for 5 minutes. Once this has completed, the AACVD reaction chamber is heated up to 450°C and the ZnO epitaxial layer on top is grown at this temperature. In total the deposition of both layers takes less than 30 minutes to complete, yielding fully crystalline, highly compact, and 002 textured thin films. The following sections of this chapter analyses the thin films grown using this low temperature seeding layer technique grown via AACVD.

4.2 Analysis

4.2.1 Crystallography

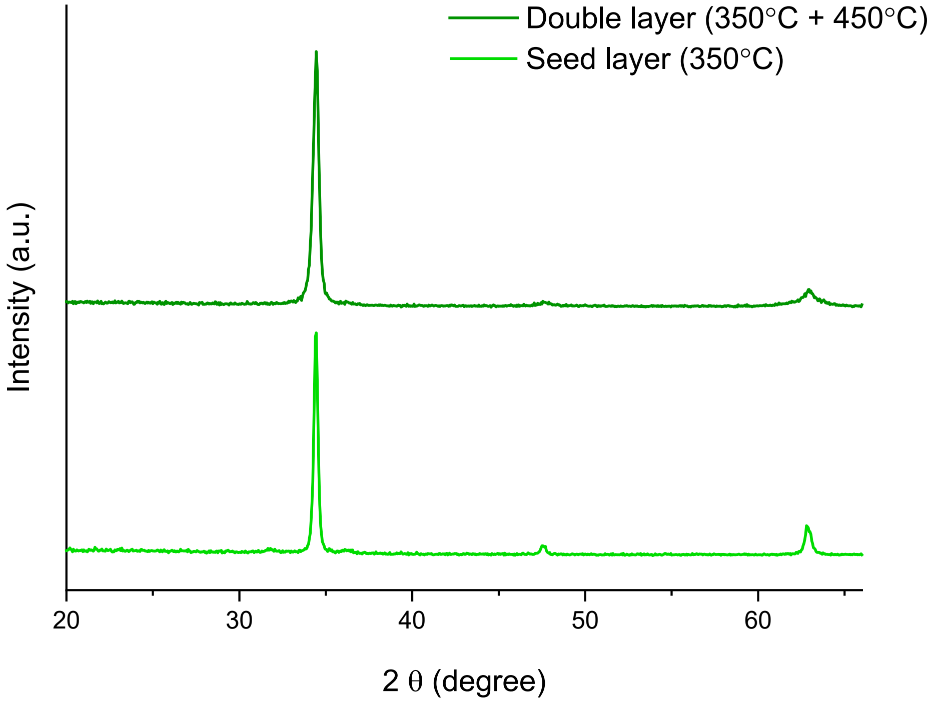

Figure 4.2 - XRD pattern of seed layer grown at 350°C and epitaxial ZnO layer grown on top at 450°C

XRD measurements of the seeding layer grown at 350°C and epitaxial ZnO thin film grown on top at 450°C have been presented in Figure 4.2 above confirming the presence of pure wurtzite ZnO with no apparent secondary phases. This crystal structure is the most common crystal structure reported for ZnO thin films in literature.

The sharp and narrow peaks observed in both XRD patterns exhibit thin films with high quality crystal growth. The deposition of the ZnO second layer on top of the seeding layer clearly shows a sharper peak observed at approx. 34.4° corresponding to the (002) plane in comparison to the seeding layer peak at 34.4° which could be attributed to the growth of larger crystallites on the top layer. The very small bumps observed either side of the 002 peak in the seeding layer, correspond to the (100) and (101) planes observed around 32° and 36°, these disappear in the second layer grown on top.

It is also worth noting the intensity of the peaks observed around 47° and 63° corresponding to the (102) and (103) planes is significantly reduced in the second epitaxial layer deposition at 450°C, as confirmed by the texture coefficient calculations plotted in the diagram below. Further to this it is evident the seeding layer grown at 350°C acts as a structural template and enhances growth in the 002 plane from a Tc value of 4.7 in the seeding layer to an improved value of 5.4. By comparing this double layer film with the thin film grown at 450°C without a seeding layer using the same precursor, EZI, the texture coefficient is found to be 4.7 whereas the double layer film has a higher texture officiation of 5.4 as shown in the figure below. This observation confirms the 2 step seeding layer method successfully yields highly textured thin films in the c-axis minimising growth in other crystal planes.

When increasing the temperature to deposit the second layer on top of the seeding layer there is the possibility of recrystallising seed layer during this step. In future the crystallinity of the seeding layer could be analysed using Xray diffraction after the temperature to increase to determine any changes to the crystallinity of the seeding layer during this step.

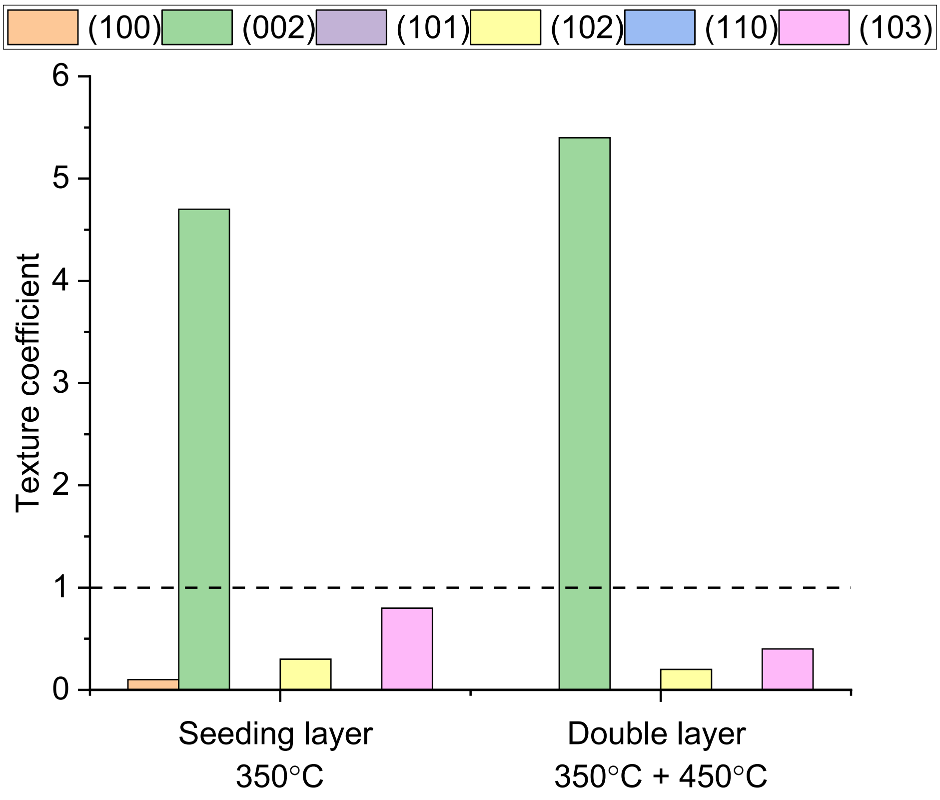

Figure 4.3 - Variation in texture coefficient for the seeding and double layers

The crystallite diameters of both layers were estimated using the Scherrer equation using the width of the (002) peak.[93] A pseudo-Voigt function was fitted to the (002) crystalline peak, and the resulting FWHM was used to estimate the average crystallite sizes of the thin film layers. An error of +/- 0.02° is estimated in the FWHM calculations carried out using this method. It was not possible to find an average value of crystallite diameters due to the absence or insufficient presence of other crystalline peaks. Therefore, when considering crystallite sizes estimated using the Scherrer equation the values are used on a qualitive basis to draw comparisons due to the known errors associated with this method.

The crystallite diameter of the seeding layer was estimated to be approximately 20nm and the double layer grown on top at 450°C was estimated to be 30nm. These values are in line with the crystallite diameters estimated for the ZnO thin films grown using the same precursor (EZI) as shown in figure 3.18. These results further confirm the seeding layer acts as a structural template and does not lead to the uncontrolled growth of large grains that can significantly hinder electron mobilities as seen when ZnO thin films are grown with precursor 1, Zn(acac)$_2$.

4.2.2 Optical Properties

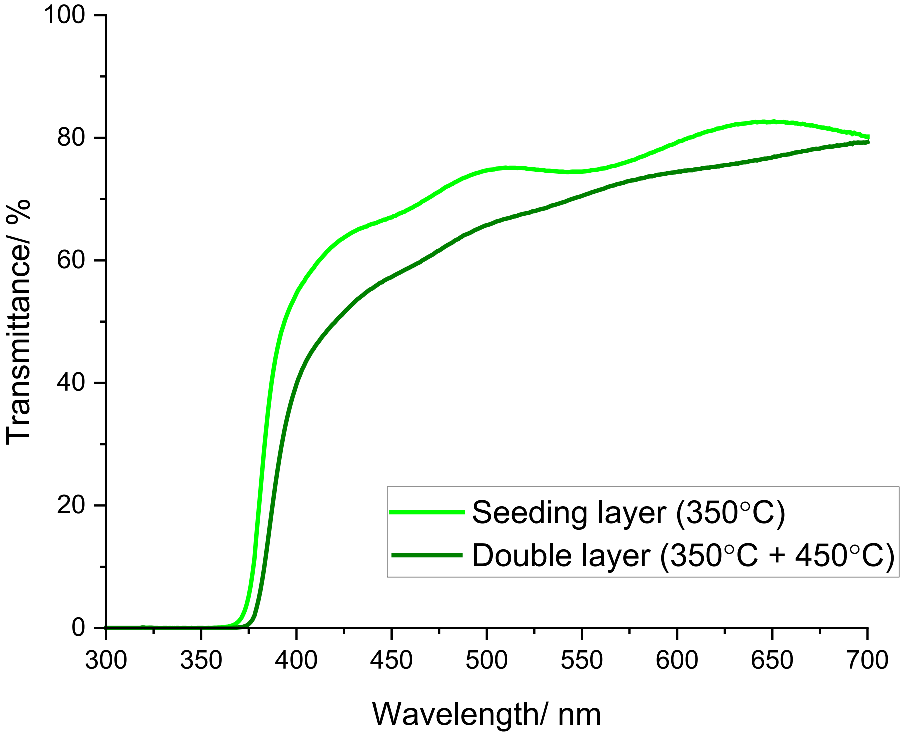

Figure 4.4 - UV-Vis measurements of seeding layer and epitaxial ZnO layer grown on top

For ZnO based thin films for TCO applications, transparency in the visible range is extremely important, as this ensures that visible light can pass through without being absorbed. As such UV-Vis measurements have been undertaken to assess the optical properties of the thin film over a wavelength range of 300-700nm, in the visible range.

Figure 4.3 shows that the seeding layer displays greater transparency in the visible region as expected, with transmittance greater than 70% at 500nm. The epitaxial layer grown on top of the seeding layer at 450°C has a slightly lower transmittance measured to be 65% at 500nm. The lower transmittance of the double layer is expected, due to the higher deposition temperature of the epitaxial layer on top. From visibly inspecting the seeding layer and the double layer thin films, the double layer presented a slightly yellower tint when compared with the seeding using the naked eye. Typically, at higher deposition temperatures darker thin films are observed and have been reported in similar ZnO thin film studies. [66]

The band gaps of the ZnO seeding layer and double layers were determined using the Tauc plot method described in the previous chapter. The band gap for the seeding layer and double layer were found to be 3.39 and 3.21eV respectively. The difference in band gap values can be attributed to the difference in thickness of the two ZnO thin films with the latter double layer film having an increased thickness. An estimated error of +/-0.2 eV is associated with the calculated band gap values using this method.

4.2.3 Microscopy

Scanning electron microscopy (SEM) was used to obtain high-definition top view and side view images of the thin films grown. These images are used to reveal the morphology of the thin films grown under these conditions and help understand the relationship between thin film morphologies and resultant optoelectronic properties.

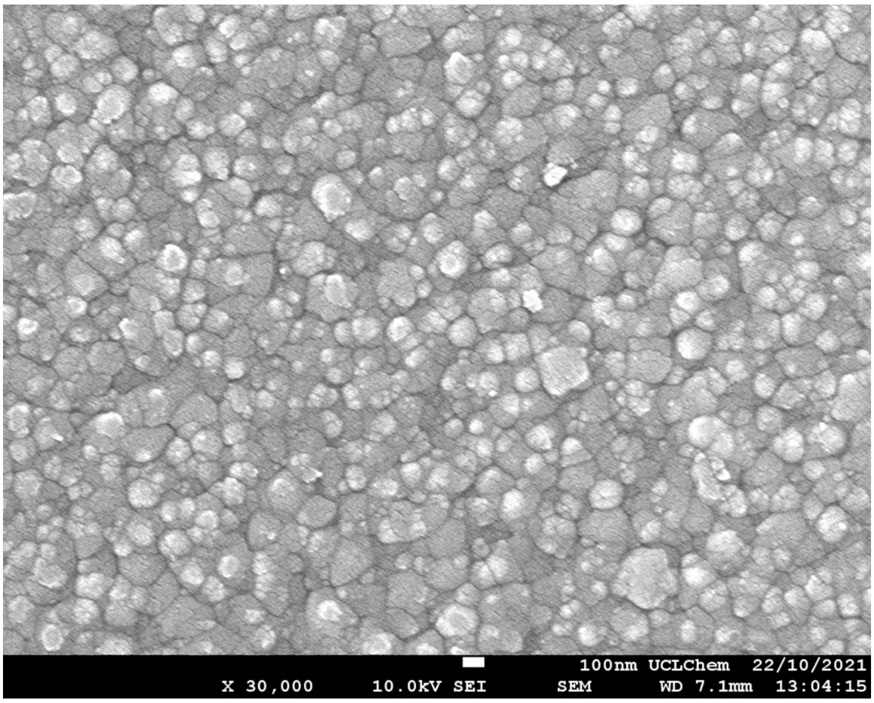

Figure 4.5 - Top view SEM image of seeding layer grown at 350°C for 5 minutes.

Figure 4.5 shows the top view SEM image taken of the seeding layer grown at 350°C for 5 minutes. In the duration of a short deposition time, this thin film already exhibits a highly directional and compact thin film. The typical columnar grain growth is seen in the films which is a typical characteristic of 002 oriented thin films and has been reported in other studies.[64,68] The formation of hexagonal tower tops is shown in these images.

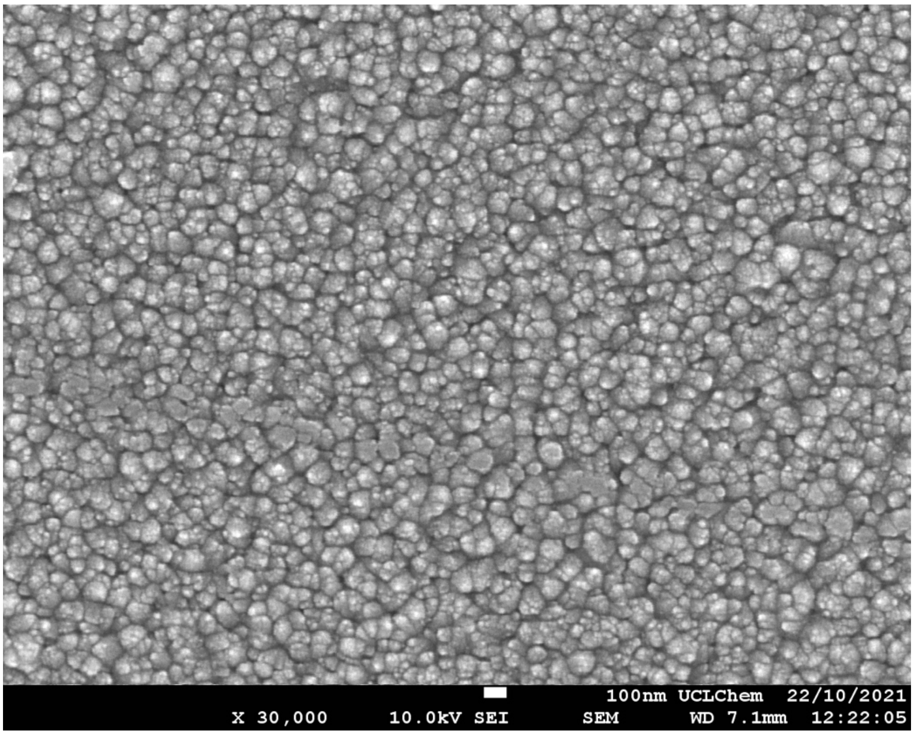

Figure 4.6 - Top view SEM image of double layer epitaxially grown on top of seeding layer

Figure 4.6 above shows the top view SEM image of the epitaxially grown ZnO layer grown at 450°C on top of the seeding layer. The impact of growing this film on top of a highly oriented seeding layer is immediately obvious when comparing Figures 4.4 and 4.5. The emerging tower tops in Figure 4 have now aligned and grown to have highly defined columnar growth. The thin film is much more uniform and compact with low surface roughness. The crystallites have all been densely packed along the c-axis, perpendicular to the substrate as a result of the highly textured homoepitaxial growth which is also seen in literature.[94,95]

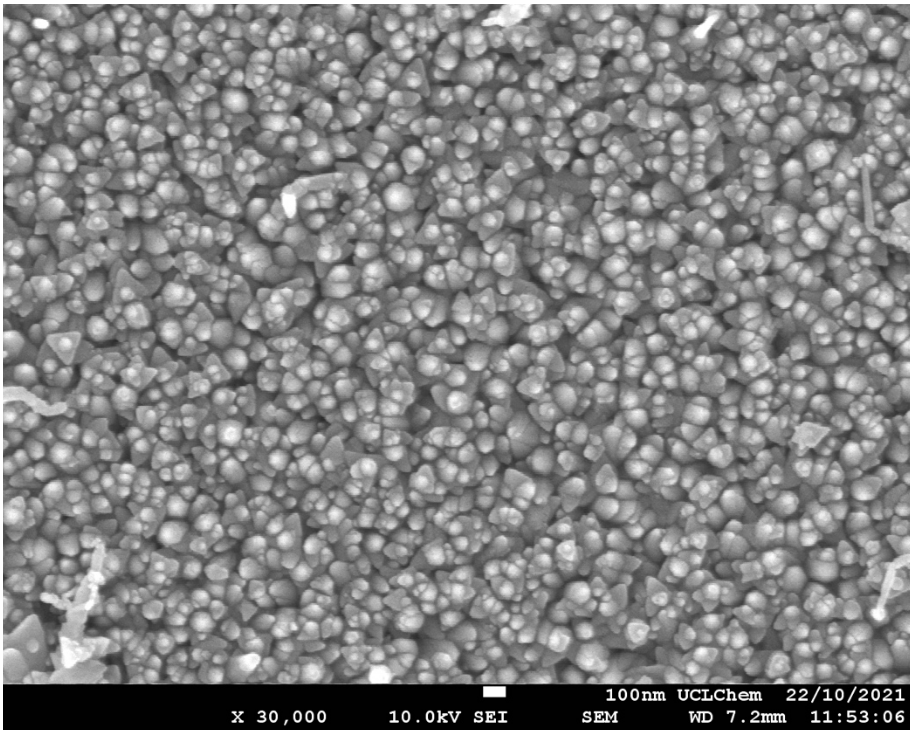

Figure 4.7 - Top view SEM image of thin film grown at 450°C using precursor 3 without a seeding layer

Figure 4.7 above shows the ZnO thin film grown at 450°C without the use of a seeding layer. Thin films grown with precursor 3 exhibited similar morphologies. However, upon comparison, the grains are not as tightly packed, and the columnar growth of the crystallites is varied. The tower tops are not yet well defined and variation in columnar growth reduces the compactness of the film. To attain high mobilities and conductivities, a highly compact and uniform thin film is needed.[91]

The top view SEM images in Figures 4.5, 4.6, and 4.7 successfully show the growth of highly directional and compact thin films with good coverage, using the seeding layer method described in this chapter. The drastic effect of using a seeding layer can be seen in these images giving rise to c-axis oriented thin films as confirmed by the XRD measurements and columnar growth seen in the SEM.

Side on SEM images were taken to further analyse thin film morphology and determine thickness.

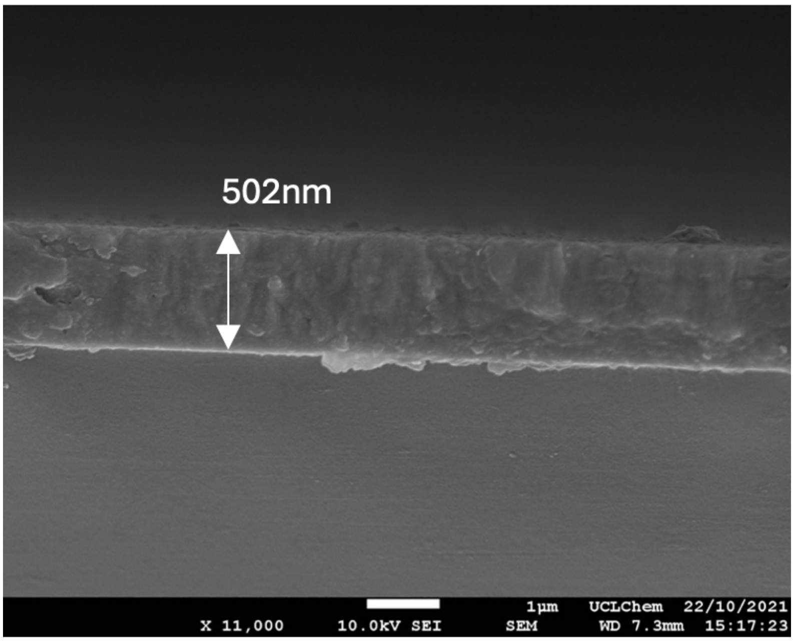

Figure 4.8 - Side on SEM image of epitaxially grown ZnO thin film on top of seeding layer

Figure 4.8 shows the side-on SEM image taken of the thin film epitaxially grown on top of the seeding layer at 450°C. The columnar growth of the grains perpendicular to the substrate, along the c-axis, can also be seen with the faint structures of columnar growth visible in this image. It is important to observe there is no obvious distinction between the seeding layer and double layer thin films in the side on SEM image above. The side on SEM image shows a uniform and compact structure further supporting the successful homoepitaxial growth of compact and 002 oriented thin films.

From this side view image, a conformal ZnO thin film is seen to be grown using the successful initial growth of a seeding layer followed by a secondary layer grown epitaxially at higher temperature. The side-on image was used to measure the thickness of the ZnO thin films; this was found to be around

500nm for the double layer grown using the seeding layer. Side-on SEM was also used to determine the thickness of the seeding layer grown at 350°C for 5 minutes which was found to be around 185nm.

4.2.4 Elemental Analysis

XPS was used to verify the presence of zinc and oxygen in both the seeding layer and double layer thin films. Figure 4.9 and 4.10 presents representative spectra depicting the Zn $2p_{3/2}$, Zn $2p_{1/2}$, and O 1s states on the film surface for the double layer film. The Zn2p peaks had a splitting of 22.5 eV appeared at energy levels of 1021.3 eV and 1043.8 eV, for Zn $2p_{3/2}$ and Zn $2p_{1/2}$ states respectively. These values fall within the expected range for ZnO.[96,97] The calculated binding energies are estimated to have an error of +/- 0.2 eV.

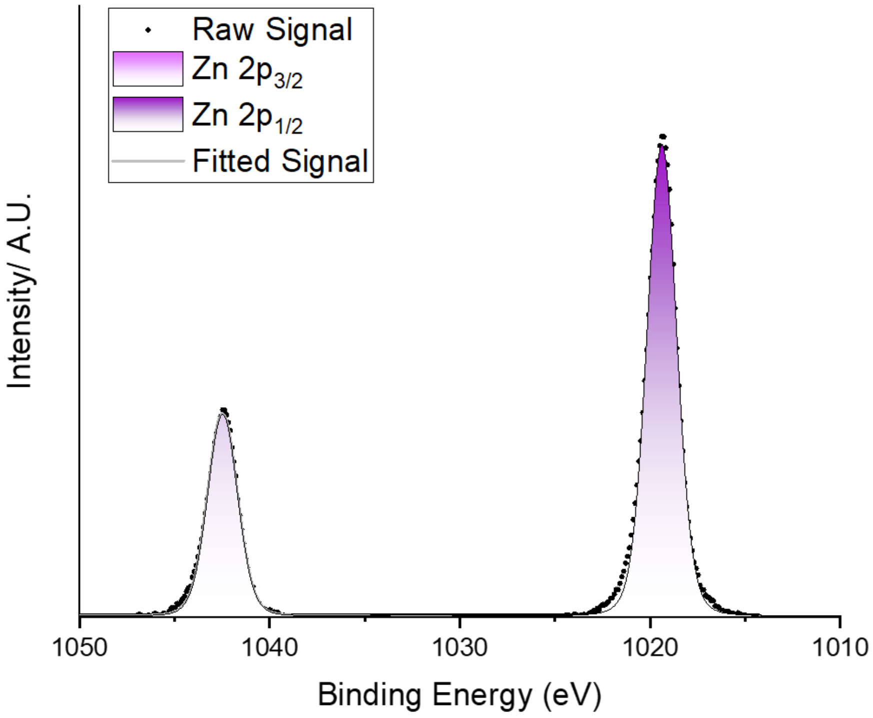

Figure 4.9 - XPS spectra for the double layer film showing the Zn 2p peaks on the film surface

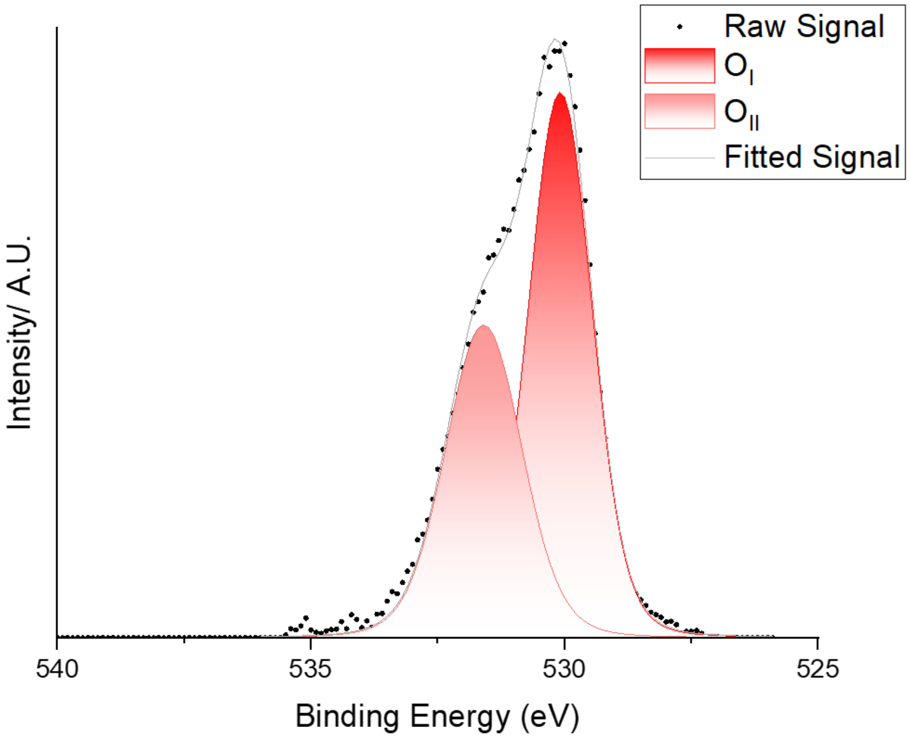

Figure 4.10 - XPS spectra for the double layer film showing the O 1s peaks on the film surface

The O 1s peak exhibited a deconvolution into two distinct states, labelled as (I) and (II) with binding energies of 530.6 eV (±0.2 eV) and 531.8 eV (±0.2 eV), respectively. The first state which is the most intense O_I is attributed with O^{2-} ions found within the ZnO structure, while the second state O_{II} can be attributed to O^{2-} vacancies in oxygen-deficient regions and surface-bound oxygen species.[98,99]

The carbon contamination in the ZnO thin film coatings, deposited from EZI solutions, was assessed by conducting X-ray photoelectron spectroscopy (XPS) after etching the films for 200 seconds under Ar. This allowed for the evaluation of the bulk film characteristics while minimising the influence of surface contaminants. This revealed the seeding layer thin film exhibited significantly lower levels of carbon species compared to the thin films deposited from precursors 1 and 2 in Chapter 1. These findings further support that the highly volatile organic by-products generated during the decomposition of EZI are more effectively desorbed at lower temperatures. This characteristic of precursor 3, enables a clean decomposition path minimising contamination during the thin film growth. During the etching process, a significant reduction in the intensity of the second peak (II) is also observed, as surface-bound oxygen species are diminished.

4.2.5 Electrical Properties

Hall effect measurements was carried out for both the seeding and double layer films at room temperature. The negative Hall effect coefficients confirms n-type conductivity in both films with electrons as the majority of charge carriers.

The thickness of the ZnO thin films was measured using two methods, first the Swanepoel method, employing a Filmetrics benchtop thin film measurement instrument. In this method, the specular reflectance profile of the films was obtained and fitted to an optical model known as the 'envelope method'. Only thickness values with a goodness-of-fit exceeding 95% were considered.

Second, the side on SEM image was also used to further corroborate the thickness of the ZnO thin films as shown in section 4.2 earlier. The film thicknesses, determined from side-on SEM images, indicate that the films double layer film is 502nm and the seeding layer film is 185nm as shown in figure 4.8.

The van der Pauw technique was used to find the resistivity (ρ), carrier concentration (n) and mobility (μ) for the seeding and double layer and has been tabulated below. Notably the carrier concentration and mobility of the double layer grown at 450°C is seen to be significantly improved from the electrical properties of seeding layer. Most importantly, the resistivity of the ZnO thin film has also decreased which implies the seeding layer method successfully produces highly textured thin films with enhanced electrical properties.

Table 5 - Electrical properties of seeding layer and double layer films

Sample Name	**d (nm)**	**n ($x10^{20}$ cm^{-3})**	**μ ($cm^2V^{-1}s^{-1}$)**	**ρ/ $x10^{-3}$ (Ω cm)**
Seeding layer (350°C)	185	1.18	16.9	2.54
Double layer (350°C + 450°C)	500	1.76	20.1	2.22

4.3 Conclusions

This study introduces a simple 2 step synthetic approach for the fabrication of conformal and ultrathin ZnO film coatings on non-epitaxial substrates grown at low temperatures using AACVD. Such studies have limited exploration in literature with most requiring higher deposition temperatures[100] or require the use of expensive epitaxial substrates.[101]

Sanchez Martin *et al* study the effect of deposition temperature on ZnO thin films grown using silicon wafer and alumina substrates at low temperatures ranging from 350°C - 400°C. Despite the use of such templates the films exhibited polycrystalline growth with diminished preferred orientation and pronounced crystal growth in multiple crystal planes when deposited at a higher temperature of 400°C.

As such this further reinforces our findings; to be able to deposit near monocrystalline thin films using a simple 2 step seeding layer method to deposit homoepitaxial ZnO thin films using a single source AACVD set up without the need for expensive epitaxial substrates. This advancement enables the rapid production of high-quality ZnO thin films for optoelectronic applications under ambient pressure conditions.

The methodologies presented in this chapter represent a significant breakthrough in the development of functional surfaces and underscore the significance of establishing precise control over conditions for designing the next generation of ZnO-based transparent conductive oxides (TCOs). The worked carried out in this chapter was done in collaboration with Clara Sanchez-Perez and the findings from this chapter have been submitted for peer review in a journal.

Chapter 5 - Aluminium Doped Zinc Oxide Thin Films

5.1.1 Background

In this chapter, the emphasis is placed on the fabrication of conductive and transparent thin films of aluminium-doped zinc oxide using a single-source AACVD setup. The resulting films exhibited a colourless appearance, demonstrated excellent adhesion, and showed no visible signs of degradation even after prolonged periods of storage.

Among the commercially utilised transparent conducting oxide (TCO) films, those composed of indium or tin-based oxides have gained widespread popularity. Indium tin oxide (ITO) stands out as the most employed TCO, closely followed by fluorine-doped tin oxide (FTO).[6,102] However, the limited availability and high cost of indium, as well as the significant increase in tin prices in recent years, have highlighted the necessity for alternative sustainable materials.[103] Zinc oxide (ZnO) films have emerged as a promising substitute due to their lower cost, greater abundance in the Earth's crust, and comparable optoelectronic properties.[89,104,105]

Doping is employed to increase the concentration of charge carriers, thereby enhancing the conductivity of a material. Additionally, at high doping concentrations, it can impact the width of the band gap.[106] At such concentrations, doping can cause the band gap to widen or undergo a blue shift, which is characterised by an increase in the frequency of phonons interacting with the incident photon. This widening occurs due to the blocking of lower states in the conduction band. Conversely, band gap narrowing can be observed when shallow-level donor impurities generate energy levels near the conduction band edge, or when shallow acceptor impurities create energy levels close to the valence band edge. The merging of the donor level with the conduction band effectively narrows the band gap.[107]

Excessive doping is detrimental to conductivity, as it degrades the film structure and hinders free electron mobility. Although intrinsic ZnO can exhibit desirable optical properties for a transparent conductive oxide (TCO), its carrier concentration at room temperature is relatively low, approximately 10^6 cm^{-3}, which is insufficient for practical TCO applications. Doping can alter the properties of ZnO, a wide band gap semiconductor with a wurtzite structure and 3.37 eV band gap.[108]

The introduction of group III dopants as shallow donors in ZnO has shown potential in the development of transparent conductive oxides (TCOs).[89,109–114] In particular, aluminium doped ZnO (AZO) films have been investigated using many different techniques such as magnetron sputtering[115,116], atomic layer deposition (ALD)[116], molecular beam epitaxy (MBE)[117], pulsed laser deposition (PLD)[118], spray pyrolysis[119], APCVD[120] and AACVD[121]. In these films, Al^{3+} ions (0.54 Å) substitute for Zn^{2+} ions (0.74 Å), resulting in a decrease in the lattice parameters.

Hu and Gordon employed atmospheric pressure chemical vapor deposition (APCVD) to deposit AZO films and observed improved conductivity compared to undoped ZnO when incorporating aluminium dopants ranging from 0.3-1.2 atomic percent (at.%).[112] AZO films deposited using a chemical spray technique (3 at.% Al doping at 450°C) exhibited lower conductivity than undoped ZnO films, according to Olvera et al.[26] This difference may stem from variations in the deposition method or higher Al doping levels leading to over-doping, though transparency remained high at approximately 85%.[122]

Sanchez-Perez *et al* reported GZO thin films with optical and electrical properties that exceed industrial standards using the novel precursor $[EtZnO^iPr]_4$.[64] As such, the following chapter focuses on the deposition and characterisation of aluminium doped ZnO thin films. To determine which of the dopants (Al/Ga), provides better optoelectronic properties. The resultant properties of thin films are not straightforward and depend on various factors, including the deposition method and conditions. Therefore, to enable a fair comparison, the films will be deposited using the same AACVD technique, employing the same carrier gas, and deposition temperature as utilised in the paper published by Sanchez-Perez *et al.*[64]

5.1.2 Introduction

This chapter details the deposition and characterisation of aluminium doped zinc oxide thin films with varying concentration of Al dopants using a single pot AACVD set up, as outlined in Chapter 1. Following the earlier precursor study in Chapter 3, thin films were deposited using the single source precursor $[EtZnO^{i}Pr]_4$ on silica coated glass. The preorganised zinc oxide precursor is used as it contains the key characteristics necessary to produce zinc oxide thin films with good optoelectronic properties, as demonstrated in Chapter 3.

5.1.2.1 The Precursor

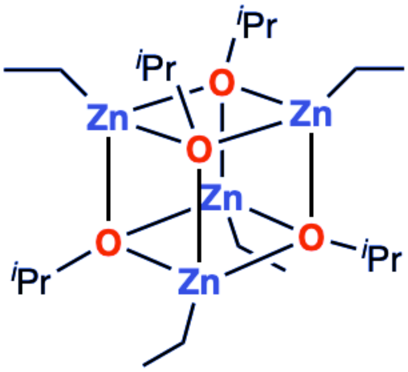

Figure 5.1 - Structure of precursor 3, ethyl isoproproxide (EZI) reproduced from Sanchez-Perez et al.

In AACVD, the precursor is transported using a carrier solvent in the form of an aerosol mist. Therefore, it is an important requirement for solid precursors to be soluble in a range of solvents for AACVD. In general, alcohols tend to be the most used solvent to transport the precursor to the reaction chamber. The presence of organic groups, which provide steric protection for the zinc centres, explains the precursor's broad solubility in organic solvents, encompassing both polar solvents such as isopropanol and non-polar solvents like toluene. As well as maximising solubility in a range of solvents, the organic groups undergo facile elimination during deposition which minimises carbon contamination in the ZnO thin films, a desirable feature in AACVD.

The preorganised “Zn_4O_4” precursor is ideal for ZnO thin film depositions because it:
- Possesses cubane-like core structure which contains the desired Zn/O ratio of 1:1;
- Undergoes a clean and favourable decomposition path eliminating volatile by-products via β-hydrogen elimination that minimises contamination; and
- Contains iPr–O moieties which enables the potential elimination of acetone, promoting the formation of oxygen-deficient species through a β-hydride transfer process.

These precursor features collectively establish this precursor as an exceptional candidate for synthesising high-quality ZnO-based coatings for opto-electronic applications, without relying on expensive epitaxial substrates. Furthermore, its stability in the presence of 2-propanol and $[Al(acac)_3]$ permits the use of a straightforward single-inlet AACVD setup to generate AZO coatings with rapid growth rates. The adoption of halogen-free synthetic routes also enables environmentally friendly and industrially sustainable deposition of TCO coatings without the necessity of scrubbers.

5.1.2.2 Materials

Diethylzinc (DEZ) in anhydrous toluene (1.0 M, Acros Organics) or toluene (1.1 M, Sigma), anhydrous isopropanol (IPA, Acros Organics) and aluminium acetylacetonate (99%, Sigma) were employed for the synthesis of the ZnO precursors and thin films.

5.1.2.3 Film deposition

The alkylzinc alkoxide molecular precursor $[EtZnO^iPr]_4$ was synthesised using the method published by Sanchez-Perez *et al*.[64] The precursor was prepared by firstly adding diethyl zinc and anhydrous toluene followed by the addition of anhydrous isopropanol at - 78°C using a drop-by-drop method. The low temperature required for the precursor synthesis was achieved using a cold bath set up around the Schlenk flask. After mixing of the reagents, a cloudy solution was formed and left to left stir under argon for 5 minutes. The solution was then left to warm up slowly to room temperature whilst stirring to allow the cloudiness to disappear. The intermediate was then isolated and various amounts of aluminium acetylacetonate $Al(acac)_3$ was added and dissolved in 15ml of anhydrous isopropanol ready for use in AACVD as shown in Scheme 1 below.

$$[EtZnO^iPr]_4 + C_6H_5CH_3 + Al(acac)_3 \xrightarrow[\text{450°C; } N_2]{\text{dry isopropanol}} AZO \qquad \text{(Scheme 1)}$$

Table 6 - Table showing deposition conditions and molar solutions for AZO thin films

Precursor(s)	**Sample Name**	**AACVD set up**	**Hydrocarbon**		**Alcohol**		**mol% in solution**	**Temperature**
			solvent	*(mL)*	*solvent*	*(mL)*	*(%(*	*(℃)*
Precursor 3 (EZI) + $Al(acac)_3$	AZO1	Single source	Toluene	*10*	IPA	*15*	*1*	*450*
Precursor 3 (EZI) + $Al(acac)_3$	AZO2	Single source	Toluene	*10*	IPA	*15*	*5*	*450*
Precursor 3 (EZI) + $Al(acac)_3$	AZO3	Single source	Toluene	*10*	IPA	*15*	*10*	*450*
Precursor 3 (EZI) + $Al(acac)_3$	AZO4	Single source	Toluene	*10*	IPA	*15*	*20*	*450*

ZnO thin films incorporating a range of Al dopant concentrations were deposited via AACVD using a one-pot precursor solution containing the zinc and aluminium precursors. The Al/ Zn molar ratios used for the precursor solutions is set out in Table 3 above to make ZnO thin films with varying Al concentration. The specified concentrations were utilised because prior studies have demonstrated that 10 mol% AZO deposited via AACVD exhibited superior electrical conductivities compared to other dopant concentrations. [123]

Thin film deposition was carried out in a cold walled AACVD reactor which contained a semi-circular graphite block upon which the glass substrate was placed and heated. The precursor solution was aerosolised using an ultrasonic liquid atomiser (LIQUIFOG, Johnson Matthey). The aerosolised precursor solution was transported to the reaction chamber using nitrogen (99.9%, BOC) as the carrier gas at a deposition temperature of 450°C.

Silica coated barrier glass was used as the substrate for thin film deposition to ensure ions from the glass did not leach into the thin films and contaminate the films. Prior to deposition, the silica coated glass substrates were cleaned using acetone (99%) and isopropanol (99%) followed by a distilled water rinse, before being left to dry at 160˚C for 1 hour.

AZO thin films grown using these conditions were smooth and adhered strongly to the substrate, fully resisting removal by a steel scalpel and by Scotch® tape. Bottom-plate deposition took place to yield hexagonal wurtzite films, typical crystal structure for ZnO thin films. The thin films produced were visibly transparent and electrically conductive; however, as Al loading increased a greater brown tint was observed in the films.

Precursor 3 (EZI) proved to be successful in the synthesis of high-quality undoped ZnO-based coatings for opto-electronic applications as shown in Chapter 1. The next set of thin films analysed in this chapter investigates the use of this novel precursor to synthesise Al doped ZnO thin films.

5.2 Results and discussion

5.2.1 Crystallography

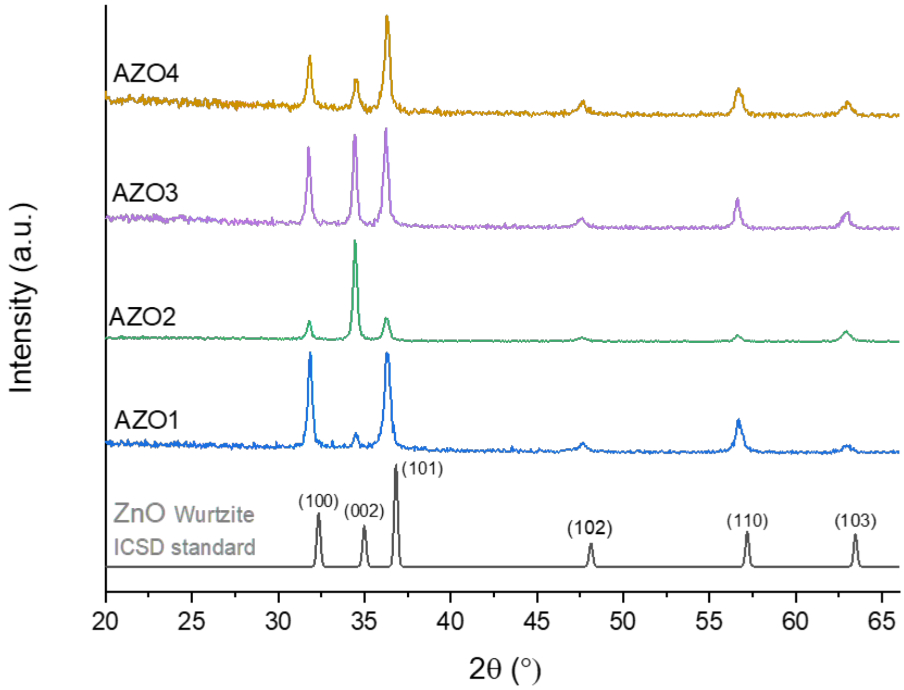

Figure 5.2 - XRD pattern of AZO thin films with varying Al concentration

The XRD patterns (figure above) confirm the presence of hexagonal wurtzite ZnO in the AZO thin films. Peaks corresponding to cubic ZnO [100], [002], [101], [102], [110] and [103] were observed at 31.8°, 34.4°, 36.3°, 47.6°, 56.7° and 62.3° values respectively. The XRD measurements does not show any peaks corresponding to secondary crystalline phases of ZnOx, AlOx, or AlZnOx. Though these peaks are absent, small quantities of these phases may exist at the grain boundaries. The intensity of the ZnO peaks in the XRD pattern could be masking the presence of these smaller phases.

AZO2 and AZO3 films presented in Figure 5.2 shows preferential orientation along the c-axis (002) direction. Preferred orientation is often observed in XRD measurements and is related to the surface free energy of the crystal plane.

Thin films tend to grow to minimise their surface energy and in the case of wurtzite ZnO, the (002) plane exhibits the highest stability, making it a commonly reported preference for ZnO thin film growth.[124–126]

The diffraction peaks observed in the XRD patterns are narrow AZO2 thin films with lower doping, suggesting good crystallinity. However, as doping is increased in the AZO thin films, the intensity of the peaks reduces suggesting a decrease in the crystallinity of the films. This is expected as heavier doping results in the disruption of the crystal structure reducing crystallinity.

Table 7 - Estimated crystallite sizes for undoped ZnO and doped AZO thin films determined using the Scherrer equation

Sample name	**Average crystallite size/ *nm***
AZO1	24
AZO2	22
AZO3	17
AZO4	16

Crystallite sizes of the undoped ZnO and doped AZO thin films were estimated using the Scherrer equation. A pseudo-Voigt function fit determined the FWHM, from which the average crystallite size was calculated. A decrease in estimated crystallite sizes were observed as Al doping increased from 1mol% in the AZO1 film to 20mol% in the AZO4 film. The Scherrer equation is known to have significant limitations in accurately determining crystallite size, and results derived from it should be interpreted cautiously.

As the concentration of aluminium loading increased in the thin films, there was a noticeable decrease in the intensity of the peaks. This phenomenon can be attributed to aluminium potentially causing a degradation in the crystalline structure of ZnO, leading to less pronounced X-ray reflections. The decreasing crystallite diameters observed further support this notion, as they are closely associated with the crystal quality of polycrystalline materials.

The expected cause for this effect lies in the disparity between the ionic radii of 4-coordinate Al^{3+} (0.53 Å) and 4-coordinate Zn^{2+} (0.74 Å). When Al^{3+} is substituted onto the Zn^{2+} sites, it introduces a slight strain within the unit cell due to the smaller ionic radius of Al^{3+}. [96,127,128] This strain can give rise to crystallographic defects like dislocations, self-interstitials, or point defects, which contribute to the observed degradation in crystallinity and the consequent decrease in X-ray reflection intensity. Similar observations have also been made in ZnO:Al thin films deposited using AACVD in previous studies.

5.2.2 Microscopy

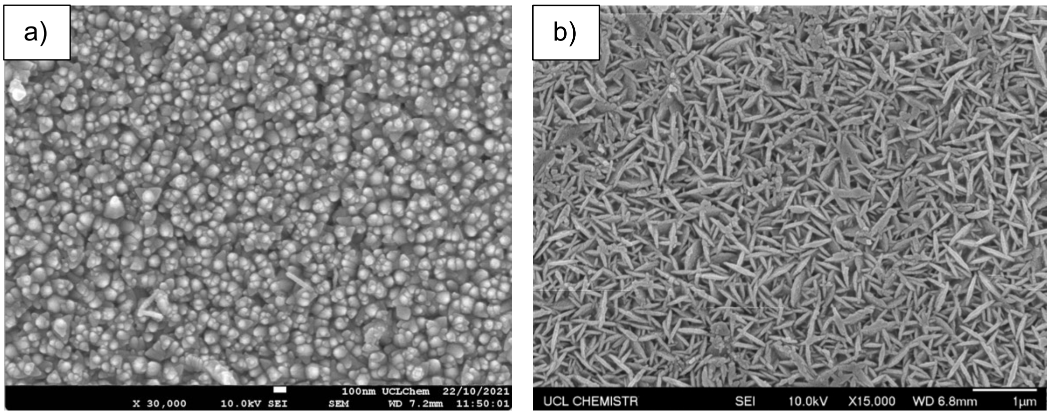

Figure 5.3 - Top view SEM images of a) undoped zinc oxide and b) Aluminium doped zinc oxide (AZO4) thin film

Scanning electron microscopy (SEM) of the undoped zinc oxide and aluminium doped zinc oxide thin film (AZO4) grown at 450°C are shown above in figure 5.3a and b above, confirming a homogeneous film across the entire surface analysed. The morphology of the thin film significantly change as aluminium is doped into the thin film as seen in figure 5.3b above.

The undoped ZnO thin film shown in Figure 5.3a exhibited a grain pattern composed of interconnected hexagonal like columns with no apparent void spaces. The almost hexagonal columns face upwards, away from the substrate which suggests columnar growth, supported by the predominant alignment along the (002) direction in the crystal structure. The diameter of the columns was roughly 60-80nm.

In Figure 5.3b, the addition of aluminium has altered the surface morphology of the film and the hexagonal like columnar growth away from the substrate is no longer seen. SEM imaging shows randomly oriented, thin, rice-shaped grains. Aluminium doping has created more defined grain shapes compared to undoped ZnO seen above and in Chapter 1. The stacking of these elongated grains suggests a Stranski-Krastanov growth mechanism, consistent with previous observations in literature. In general, the grain size decreased upon Al doping giving rise to more well-defined rice like grains which do not exhibit columnar growth in the c-axis. This is also seen in the XRD patterns and crystallite sizes, estimated for the thin films.

5.2.3 Elemental Analysis

X-ray photoelectron spectroscopy (XPS) provided information on the thin films' elemental composition, oxidation states, contaminant levels and the composition of the native oxide. The observed peaks in the XPS analysis were modelled, and the binding energy values were compared to those reported in the literature to identify the elements in the film and the native oxide layer. To examine the bulk of the film, films were etched for 200s under argon and the results were compared with the elemental composition on the surface of the film. Since sputtering can produce unreliable results due to variations in elemental sputtering rates, the XPS data from etching were not deconvoluted.

The survey spectra indicated the presence of carbon, oxygen, zinc, and aluminium in all the films. Carbon contamination was detected on both the surfaces and within the bulk of the films, indicating the presence of carbon. This contamination could be due to the thermal breakdown of $Al(acac)_3$, a process that is less efficient compared to the decomposition of other organoaluminium precursors like $AlMe_3$. Consequently, carbon species became trapped during the growth of the films. To calibrate the data, adventitious carbon was employed, with a binding energy of 285 eV for the carbon 1s peaks.

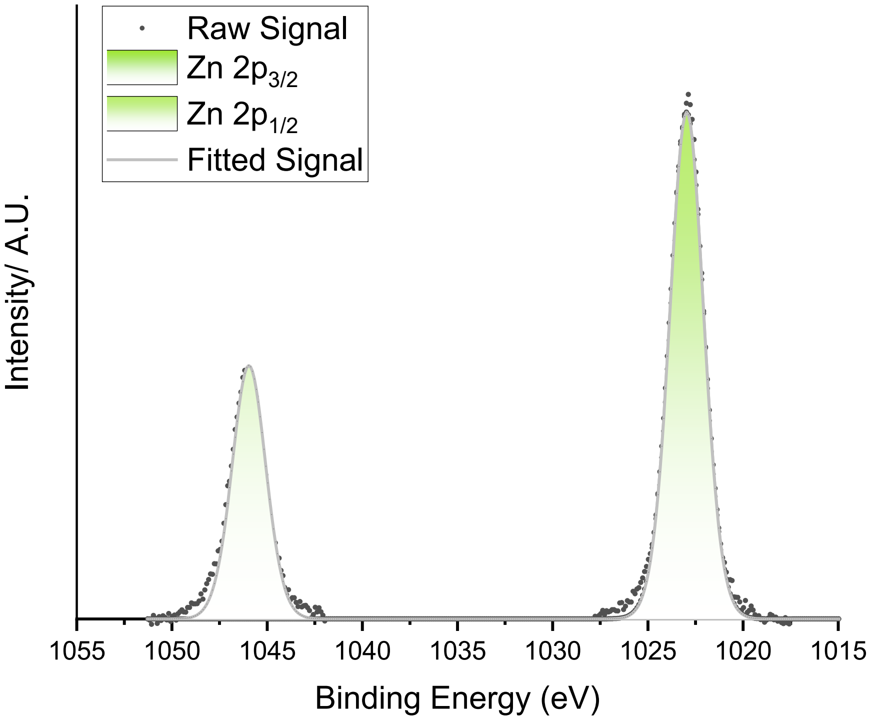

Figure 5.4 - XPS spectra showing Zn2p$_{3/2}$ and Zn2p$_{1/2}$ peaks on the surface of AZO1

The oxidation states of Zn and Al in the AZO films were analysed using X-ray photoelectron spectroscopy. Only one film (AZO1) has been shown here as the pattern is similar for all doped samples. CasaXPS was used to and deconvolute and analyse the scanned 2p peaks. This revealed that each peak consisted of two distinct components. This splitting of the peaks is attributed to spin-orbit coupling, wherein the spin of an electron interacts with the magnetic field generated by its motion.[129–132] As a result, the 2p orbital divides into a $2p_{1/2}$ orbital and a $2p_{3/2}$ orbital. The $2p_{1/2}$ orbital possesses lower energy compared to the $2p_{3/2}$ orbital, requiring more energy to free an electron from the former. Consequently, the $2p_{1/2}$ peak appears at a higher binding energy in the XPS spectrum than the $2p_{3/2}$ peak. The 2p orbitals were specifically investigated for zinc and aluminium.

The peak for Zn $2p_{3/2}$ was found to be approximately at 1022.2 eV confirming the presence of Zn^{2+} in ZnO, corroborated by the XRD patterns.[126,133] In the case of the Al 2p peaks, $2p_{3/2}$ and $2p_{1/2}$ states overlap and positions of the Al $2p_{3/2}$ and Al $2p_{1/2}$ were found to be at approximately 75.1 eV and 74.8 eV confirming the presence of Al^{3+}.[134–136] The distinctive peak associated with metallic aluminium at 72.8 eV was not detected on the surfaces or within the bulk of the films. [137]

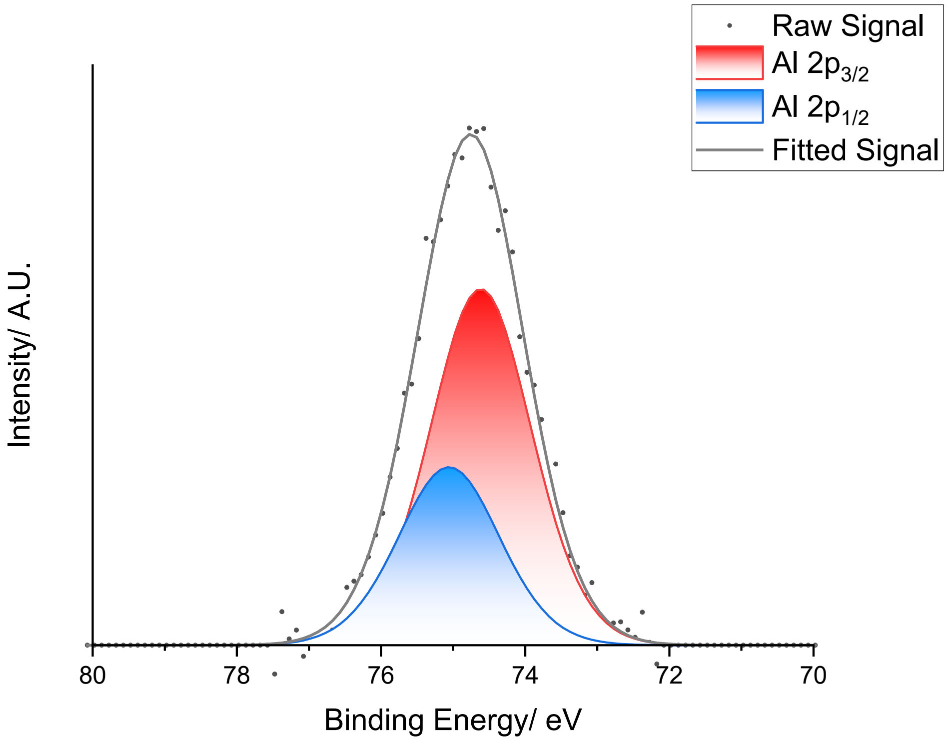

Figure 5.5 - XPS spectra showing Al$2p_{3/2}$ and Al$2p_{1/2}$ peaks on the surface of AZO1

A steady increase in aluminium at% is observed in the XPS data from sample AZO1 to AZO4. To calculate the aluminium concentration in doped thin films, the peak areas of Al 2p and Zn 2p are used. The following ratio estimates this concentration:

$$(A_{Al2p}/S_{Al2p})/\ (A_{Al2p}/S_{Al2p}+\ A_{Zn2p}/S_{Zn2p})$$

where A is the peak area of Al 2p or Zn 2p and S is the sensitivity factor (0.537 for Al 2p, 28.7 for Zn 2p). The at% of aluminium in the thin films has been determined using the method above using XPS data and tabulated below. The relative concentrations of Al and Zn were used to determine the different values for x in the formula $Al_xZn_{1-x}O$.

Sample Name	**mol.% in solution**	**at.% determined by XPS**	**$Al_xZn_{1-x}O$**
AZO1	1	0.4	$Al_{0.004}Zn_{0.996}O$
AZO2	5	3.2	$Al_{0.032}Zn_{0.968}O$
AZO3	10	9.6	$Al_{0.096}Zn_{0.904}O$
AZO4	20	13.3	$Al_{0.133}Zn_{0.867}O$

At the surface, x ranged from 0.4 to 13.3 while in the bulk Al concentration decreases considerably. This is expected and has also been reported in similar Al doped ZnO thin film studies using AACVD.

5.2.4 Optical Properties

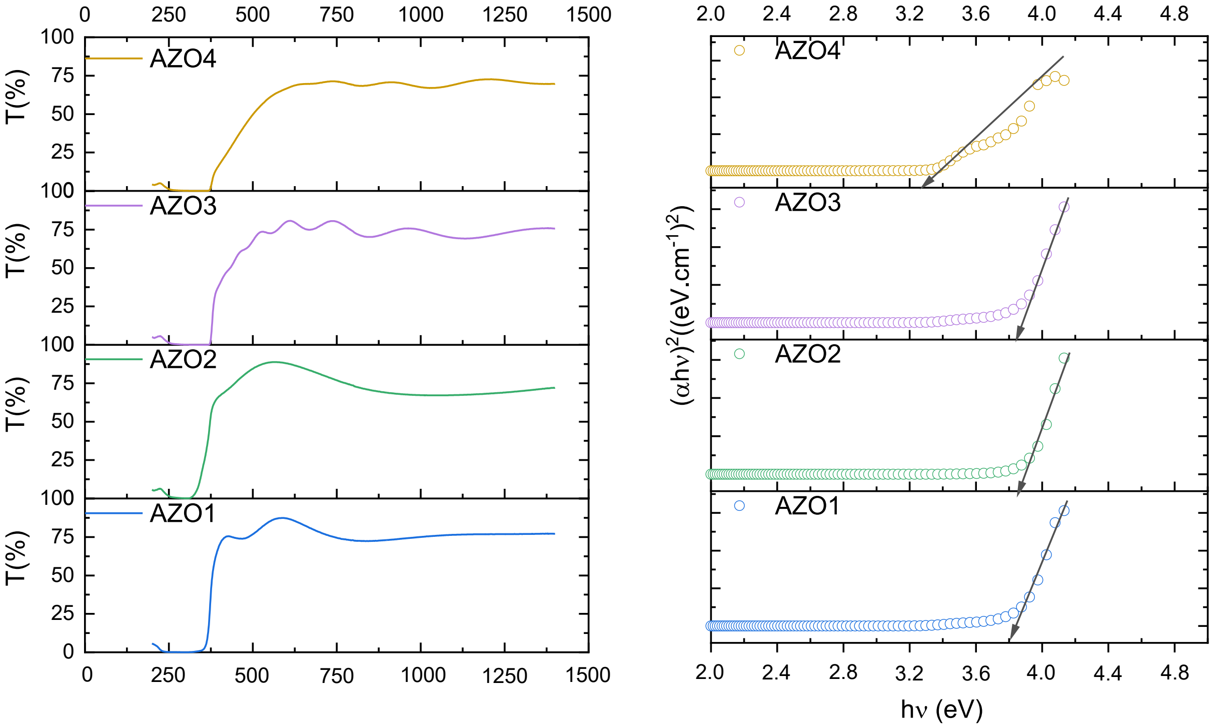

Figure 5.6 - Optical transmittance of Aluminium doped ZnO thin films grown at 450℃ (left) and tauc plots (right)

Both doped and undoped ZnO thin films exhibited high transparency in the visible range, as shown by UV-Vis spectroscopy in Figure 5.6 above. Specifically, at a wavelength of 550 nm, the aluminium-doped films exhibited transparencies exceeding 75%, while the undoped ZnO film was found to be slightly less than this. In general, at longer wavelengths, a lower transmittance is observed as Al concentration is increased. This suggests a greater absorption of infrared light than visible light as Al doping increased.

The transmission data for the undoped and doped AZO thin films was used to determine the band gap of the films using Tauc plot calculations. Upon doping the films with aluminium the band gap initially increased to around 3.8 eV for AZO1, AZO2 and AZO3. This observation aligns with the Moss-Burstein effect, as discussed earlier. The observed increase in band gap aligns with the enhanced transparency observed in the visible spectrum (Figure 5.6). However, as the dopant concentration increased in AZO4, a noticeable reduction in band gap was seen due to band gap narrowing, as discussed earlier.

The calculated band gap values for each of the films have been tabulated below. It is important to note band gap estimations calculated using Tauc relation are subject to a significant margin of error. Therefore, definitive values derived from this approach may not accurately represent the true optical properties of the thin film.

Table 8 - Band gap values of undoped ZnO and doped AZO thin films

Sample name	Band gap/ eV
AZO-1	3.79
AZO-2	3.84
AZO-3	3.81
AZO-4	3.29

Interference fringes were seen on the undoped ZnO film. This is due to variations in thickness across the thin film. The presence and intensity of interference fringes were dependent on the thickness of the films. Multiple reflections at the interfaces (air/thin film, thin film/substrate and barrier coating/substrate) can also create interference fringes.

5.2.5 Electrical Properties

Resistivity (ρ), carrier concentration (n) and mobility (μ) were determined for each film using the van der Pauw method. Negative Hall coefficients confirmed n-type conductivity with electrons as the predominant charge carriers in both doped and undoped thin films.

Table 9 - Film thickness and electrical properties of doped and undoped ZnO thin films.

d, film thickness; n, charge carrier concentration; μ, charge carrier mobility; ρ, bulk resistivity

Sample Name	**d (nm)**	**n ($\times10^{20}$ cm^{-3})**	**μ (cm^{2}V^{-1}s^{-1})**	**ρ/ $\times10^{-3}$ (Ω cm)**	**R_{sh}/ Ω □$^{-1}$**	**T_{550}/ %**	**F.o.M/ Ω^{-1}**
ZnO	500	1.18	20.1	2.53	50.6	78	1.54
AZO1	440	1.76	16.9	2.22	50.5	88	1.74
AZO2	480	1.83	14.6	1.93	40.2	87	2.16
AZO3	450	2.14	15.3	1.76	39.1	73	1.87
AZO4	410	1.54	13.3	2.43	59.3	65	1.10

The doped films showed improved electrical properties compared to the undoped thin films, as expected and shown in the table above. In general, the charge carrier concentration (n) increased and resistivity (ρ) decreased with higher levels of aluminium dopant except for AZO4 not following this trend. Resistivity was found to increase for AZO4 with a higher aluminium concentration. The initial decrease in resistivity is attributed to the introduction of charge carriers into the conduction band, whereby aluminium acts as a donor dopant. However, at high dopant concentrations, there is a subsequent increase in resistivity due to a decrease in electron mobility which can be influenced by various factors.

One contributing factor is the reduction in crystal quality as shown in the XRD pattern for AZO-4. The loss of long-range crystal order hinders the easy passage of electrons through the film compared to a perfect crystal structure. Additionally, the high concentration of charged dopant sites in the films leads to increased scattering of electrons, known as impurity scattering. This scattering effect further reduces electron mobility as the electrons interact with the charged dopant sites.

Generally, increased charge carrier concentration reduces mobility due to more collisions. Trapping of charge carries at grain boundaries further reduces mobility and increases resistivity. The AZO films exhibited a higher carrier concentration compared to the undoped ZnO film, resulting in a decrease in mobility.

The electrical properties of the AZO films produced in this chapter can be compared to other studies on aluminium doped ZnO thin films deposited under comparable conditions.

Bhachu *et al.* and Ponja *et al.* made AZO films on glass substrates through AACVD at a deposition temperature of 450 °C.[124,126] They achieved improved resistivity values of 8.35×10^{-4} Ω·cm and 2.15×10^{-3} Ω·cm, respectively. However, it is noteworthy that both studies utilised highly pyrophoric precursors, namely diethyl zinc and trimethyl aluminium [$AlMe_3$]. The highly reactive and pyrophoric nature of these precursors required extra precautions making the synthesis process challenging and hazardous.

In contrast, the films deposited in this chapter employed significantly safer and non-pyrophoric precursors. This is advantageous, especially for commercial applications where safety considerations play a crucial role.

In another study of AZO thin films grown using Zn(acac)$_2$ with different solvents by Potter *et al.* it was found that the use of only MeOH as a solvent had lower resistance and higher mobilities whereas the addition of other solvents such as Toluene and THF were reported to have significantly increased resistance and subsequently reduced mobility. The lower electrical properties of these films is attributed to their inferior crystal quality, as suggested by the relatively low intensity peaks observed in the XRD pattern. A similar pattern is also observed in the AZO films discussed in this thesis whereby poorer crystal quality is observed in the XRD as the aluminium doping increases, indicated by the relatively low intensity peaks.

The electrical properties for AZO films made using the precursor 3, [EtZnO^{i}Pr]$_4$ exhibited lower mobility values than those reported for GZO thin films made using the same precursor by Sanchez-Perez *et al.*[64] The higher mobilities exhibited by the GZO films could be explained by looking at the ionic radii of the two dopants Al^{3+} and Ga^{3+}. Out of the 2 dopants, Ga^{3+} has the closest ionic radius to Zn^{2+}.[138,139] This implies that substituting Ga^{3+} for Zn^{2+} should cause less lattice distortion compared to Al^{3+}.[140] A comparative study on aluminium doped and gallium doped ZnO thin films for TCO applications also suggested Ga^{3+} ions could minimise their impact on ZnO crystallinity when incorporated into ZnO films owed to the smaller difference in atomic radii of Ga^{3+} and Zn^{2+}.[141] By preserving the crystal structure, more favourable pathways for charge carriers are created, resulting in higher mobility.

Additionally, the larger size of gallium compared to aluminium means the 3d orbitals of gallium are more shielded than the 2p orbitals of aluminium. As a result, it is relatively easier to remove an electron from the gallium 3d orbitals compared to the 2p orbitals of aluminium.

Another contributing factor could be the relative increase in surface segregation of the dopant as aluminium concentration is increased. This phenomenon, previously documented, occurs when the dopant segregates to the grain boundaries and forms oxide bonds.[142] It occurs when the dopant reaches its solubility limit in the film. [143,144] High aluminium concentrations result in significant surface segregation, which can be attributed to the small ionic radius of Al^{3+}. The high deposition temperatures provide the Al^{3+} ions with sufficient energy to diffuse through the lattice[145] Typically, dopant segregation becomes more pronounced at higher dopant concentrations.[96] The formation of oxide phases, such as Al_2O_3, within the grain boundaries, caused by the segregation, has insulating properties and often leads to a deterioration in the electrical characteristics of the film.[127] These grain boundaries trap charge carriers which can also hinder the mobility of electrons.

5.3 Conclusions

In this study aluminium doped zinc oxide (AZO) thin films were successfully produced via AACVD with the novel zinc precursor, EZI. Varying dopant concentrations of 1, 5, 10, and 20 mol% were used in samples AZO1, AZO2, AZO3 and AZO4 respectfully to find the optimum dopant concentration. The resulting films exhibited high quality and excellent adhesion to the glass substrates. XRD analysis confirmed the presence of only wurtzite ZnO, with no secondary phases observed. The Al doped films displayed high transparency, with lower doped samples exceeding 80% in the visible spectrum, thus meeting the requirements for various industrial TCO applications.

The electrical properties of the films were comparable to those reported in other studies involving doped ZnO films deposited under similar conditions. Notably, the electrical performance was particularly impressive considering the simplicity and cost-effectiveness of the synthesis process, achieved by using safe and easy-to-handle precursors. The 10 mol% AZO film (AZO3) exhibited the lowest resistivity achieved, measuring 1.76×10^{-3} Ω·cm and a figure of merit (F.o.M) value of 1.87. Doping at higher concentrations lead to increased resistivities, narrowing of the band gap and unwanted pronounced brown hue on the thin films.

Chapter 6 - Conclusions and Future Work

6.1 General conclusions

This thesis demonstrates the use of Aerosol Assisted Chemical Vapour Deposition as a facile method to produce thin films with desirable characteristics for Transparent Conducting Oxides (TCOs) applications. AACVD is a versatile technique that opens the use of a larger range of precursors that do not have to be volatile.

The thesis has focused on synthesising zinc oxide based thin films for optoelectronic applications by primarily focusing on two key areas:

1. Investigating the effect of molecular precursor choice on the resultant morphologies and optoelectronic properties of ZnO thin films
2. Enhancing optoelectronic properties of ZnO based TCOs through:
    a. Using a ZnO seeding layer to promote the growth of highly textured c-axis oriented thin films (Chapter 3)
    b. Dope varying concentrations of aluminium to find the optimum dopant concentrations to yield high performance TCOs

Within this thesis, a total of 36 films were analysed and extensively discussed regarding their optoelectronic properties. Remarkably, the majority of the films exhibited transparencies close to the desired 80% threshold, which is a fundamental requirement for a Transparent Conducting Oxide (TCO). It is worth mentioning that the aluminium-doped films discussed in Chapter 5 exhibited reduced transparency at higher dopant concentrations. For comparison purposes, all films were evaluated against an undoped ZnO.

Chapter 3 of the thesis explores how the purity and morphology of ZnO thin film coatings are significantly influenced by various synthetic parameters during crystal nucleation and growth. A comprehensive investigation is conducted in this chapter to understand the impact of molecular precursors with different Zn:O atomic ratios in different chemical environments, aiming to gain insights into the chemical environment of Zn centres during crystal growth.

In this chapter, it is observed that conventional acetylacetonate-based precursors tend to yield ZnO coatings with subpar properties, such as low purity, non-compact structures, and large crystallites. To address these issues, an alternative approach is employed in which ZnO film coatings are synthesised using a chemical intermediate obtained from the reaction of DEZ/toluene with IPA, as previously developed by Sanchez-Perez *et al*. This methodology allows for the synthesis of ZnO films with comparable nucleation and growth rates while achieving improved properties compared to those obtained with acetylacetonate-based precursors.

Following this chapter, the single source precursor has been used to deposit ZnO as seeding layers to grow highly textured c-axis oriented thin films with near to monocrystalline structures. This simple two step seeding layer approach successfully yielded ZnO thin films with preferred orientation in 002 crystal plane, significantly reducing the growth of other crystal planes. The low temperatures used to achieve epitaxial growth in ZnO thin films using AACVD is the first of its kind.

The final chapter of this thesis explores varying concentrations of aluminium doping in ZnO thin films to find an optimum dopant concentration to increase optoelectronic properties. The AZO thin films produced in chapter 5 also use the novel zinc precursor ethyl isopropoxide to produce aluminium doped zinc oxide thin films. From this study, 10mol% of Al doping was found to achieve the lowest resistivity of $1.76 \times 10^{-3}\ \Omega\cdot\text{cm}$.

6.2 Future Work

The findings presented in this thesis have made a significant contribution to the existing literature in materials chemistry. However, there is still potential for further exploration and expansion in this field.

The results from Chapter 3 have demonstrated that precise control over the structural and optoelectronic characteristics of ZnO films can be achieved through careful choice and design of the precursor. To deepen our understanding of this relationship, it would be beneficial to explore a broader range of precursors to further understand the Zn:O ratios impact on resultant film morphologies and optoelectronic properties.

Further analysis could also be carried out on the thin films presented in this chapter such as using TEM (transmission electron microscopy) to obtain high resolution images of the thin films which can provide more information on the thin film microstructure such as crystallite structure, grain boundaries, defects and interfaces within the film. TEM can also refine the Scherrer analysis for crystallite size in thin films, leading to more accurate measurements of grain size and shape which can improve the reliability of this method.

Furthermore, the Williamson-Hall method could also be used to study the strain within the crystallites of ZnO thin films which can influence optoelectronic properties. By analysing the broadening of diffraction peaks in X-ray diffraction patterns, the strain induced in the crystallites can be measured and used to optimise thin film deposition processes to minimise strain and enhance the performance of thin films in TCO applications.

Another technique which could be used in future research is Atomic Force Microscopy (AFM). AFM can be used to characterise the surface characteristics such as defects (pinholes or grain boundaries) or smoothness of thin films, which are crucial factors affecting the optical and electrical properties of TCOs. More specifically conductive AFM (c-AFM) could be used to simultaneously measure electrical conductivity and surface topography, offering a more comprehensive understanding of the thin film's properties.

Chapter 4 presents a promising seeding layer approach to produce highly textured c-axis oriented ZnO thin films. However, the research discussed in this chapter does not explore the potential for recrystallising the seeding layer during the two-step deposition process. Therefore, an important avenue for future research would be to investigate the crystallinity of the seeding layer to determine if there are any changes following the temperature increase. Assessing the crystallinity of the seeding layer could provide valuable insights into whether the structure evolves during the deposition process and how this affects the overall properties of the thin films. As such this investigation could provide valuable insights into optimising the two-step deposition method and improving the quality of the resulting thin films.

Further exploration into the low-temperature deposition of seeding thin films in AACVD holds promise for advancing epitaxial growth and achieving near monocrystalline structures in thin films. Fine-tuning and exploring the parameters of this method could lead to optimised deposition conditions, enhancing the quality and uniformity of thin films for TCO application.

Additionally, the deposition of ZnO seeding layers at low temperatures opens up possibilities for applications in flexible optoelectronics. These thin films could be deposited on temperature-sensitive substrates, enabling the fabrication of flexible devices for various optoelectronic applications.

The final results chapter investigates the use of aluminium as a dopant using the zinc precursor, ethyl isopropoxide. The only other dopant studied in literature using this precursor is Ga, as such other dopants can be investigated using this precursor. Furthermore, the ZnO seeding layers discussed in Chapter 4 could be used to deposit AZO or other doped ZnO layers on top to produce thin films with near monocrystalline structure minimising resistivities caused by grain boundaries and increase mobility and conductivity in ZnO based TCOs for optoelectronic applications.

Finally for future work, using positron annihilation spectroscopy (PAS) with monoenergetic, variable-energy positron beams (VEPAS) as an additional analysis technique could provide insights into vacancy-type defects in both doped and undoped ZnO thin films. Previous studies employing VEPAS have revealed important information about the microstructure and defects in ZnO films, including identifying dominant defect types under different growth conditions.[146–148] For example, Peng *et al*. observed that the primary defects in reactively sputtered ZnO films varied with the oxygen-to-metal ratio (R), while Uedono *et al.* detected zinc vacancies as predominant defects in thin ZnO films grown by laser MBE.[149,150] Additionally, Zubiaga *et al.* correlated photoluminescence (PL) spectra with the concentration of Zn vacancies in ZnO films grown by MOCVD.[151] Incorporating VEPAS analysis in future research could further enhance our understanding of defect behaviour in both doped and undoped ZnO thin films.

Chapter 7 - References

1. Hille K, Sevastopulo D. TSMC: the Taiwanese chipmaker caught up in the tech cold war. Financial Times. 2022 Oct;
2. Dixon SC, Scanlon DO, Carmalt CJ, Parkin IP. n-Type doped transparent conducting binary oxides: an overview. J Mater Chem C. 2016;4:6946–61.
3. Hayashi K, Matsuishi S, Kamiya T, Hirano M, Hosono H. Light-induced conversion of an insulating refractory oxide into a persistent electronic conductor. Nature. 2002 Oct 3;419(6906):462–5.
4. Ikhmayies SJ. Transparent Conducting Oxides for Solar Cell Applications. In: Sayigh A, editor. Mediterranean Green Buildings & Renewable Energy. Cham: Springer International Publishing; 2017. p. 899–907.
5. Granqvist CG. Electrochromics for smart windows: Oxide-based thin films and devices. Vol. 564, Thin Solid Films. Elsevier; 2014. p. 1–38.
6. Minami T. Transparent conducting oxide semiconductors for transparent electrodes. Semicond Sci Technol. 2005 Apr;20(4).
7. Godinho KG, Carey JJ, Morgan BJ, Scanlon DO, Watson GW. Understanding conductivity in SrCu2O2: Stability, geometry and electronic structure of intrinsic defects from first principles. J Mater Chem. 2010;20(6):1086–96.
8. Anthony R West. Basic Solid State Chemistry. 1999.
9. Sze SM, Ng KK. Physics of semiconductor devices. Wiley-Interscience; 2007. 815 p.
10. Hoffman R. Solids and surfaces: A chemist’s view of bonding in extended structures. 1st ed. 1988. 139 p.
11. Yu PY, Cardona M. Fundamentals of Semiconductors - Physics and Materials Properties. 4th ed. Springer; 2010. 1–669 p.
12. Kahraman S, Çakmak HM, Çetinkaya S, Bayansal F, Çetinkara HA, Güder HS. Characteristics of ZnO thin films doped by various elements. J Cryst Growth. 2013;363:86–92.
13. Wenham S, Green M, Watt M, Corkish R, Sproul A. Applied Photovoltaics. 3rd ed. 2011. 36 p.
14. Mishra S, Ganguli B. Effect of p-d hybridization, structural distortion and cation electronegativity on electronic properties of ZnSnX2 (X=P, As, Sb) chalcopyrite semiconductors. J Solid State Chem. 2013 Apr;200:279–86.
15. Luque A (Antonio), Hegedus Steven. Handbook of photovoltaic science and engineering. Wiley; 2011.
16. Fujita M. Silicon photonics: Nanocavity brightens silicon. Vol. 7, Nature Photonics. 2013. p. 264–5.
17. Kikkawa JM, Awschalom DD. Resonant Spin Amplification in n-Type GaAs. Physical Review. 1998;80(19):4313.
18. Kittel C. Introduction to Semiconductor Physics. 7th ed. John Wiley & Sons; 1996. 428 p.
19. Ganose AM, Scanlon DO. Band gap and work function tailoring of SnO2 for improved transparent conducting ability in photovoltaics. J Mater Chem C Mater. 2016;4(7):1467–75.

20. Banerjee AN, Chattopadhyay KK. Recent developments in the emerging field of crystalline p-type transparent conducting oxide thin films. Progress in Crystal Growth and Characterization of Materials. 2005 Jan 1;50(1–3):52–105.
21. Jain A, Sagar P, Mehra RM. Band gap widening and narrowing in moderately and heavily doped n-ZnO films. Solid State Electron. 2006 Jul;50(7–8):1420–4.
22. Hung-Chun Lai H, Basheer T, Kuznetsov VL, Egdell RG, Jacobs RMJ, Pepper M, et al. Dopant-induced bandgap shift in Al-doped ZnO thin films prepared by spray pyrolysis. J Appl Phys. 2012 Oct 15;112(8).
23. Saw KG, Aznan NM, Yam FK, Ng SS, Pung SY. New Insights on the Burstein-Moss Shift and Band Gap Narrowing in Indium-Doped Zinc Oxide Thin Films. Mishra YK, editor. PLoS One [Internet]. 2015 Oct 30 [cited 2023 Jun 28];10(10):e0141180. Available from: https://dx.plos.org/10.1371/journal.pone.0141180
24. Burstein E. Anomalous Optical Absorption Limit in InSb. Physical Review. 1954;93:632.
25. Moss TS. The Interpretation of the Properties of Indium Antimonide. Proceedings of the Physical Society Section B [Internet]. 1954 Oct 1;67(10):775–82. Available from: https://iopscience.iop.org/article/10.1088/0370-1301/67/10/306
26. Jin S, Yang Y, Medvedeva JE, Ireland JR, Metz AW, Ni J, et al. Dopant ion size and electronic structure effects on transparent conducting oxides. Sc-doped CdO thin films grown by MOCVD. J Am Chem Soc. 2004 Oct 27;126(42):13787–93.
27. Liu H, Avrutin V, Izyumskaya N, Özgr Ü, Morkoç H. Transparent conducting oxides for electrode applications in light emitting and absorbing devices. Vol. 48, Superlattices and Microstructures. 2010. p. 458–84.
28. Stadler A. Transparent Conducting Oxides—An Up-To-Date Overview. Materials. 2012 Apr 19;5(12):661–83.
29. Gordon R. Criteria for Choosing Transparent Conductors. MRS Bull. 2000;25:52–7.
30. Ginley DS, 秀雄細野, Paine DC. Handbook of transparent conductors. 2011. 1–25 p.
31. Lokanc M, Eggert R, Redlinger M. The Availability of Indium: The Present, Medium Term, and Long Term [Internet]. 2015. Available from: www.nrel.gov/publications.
32. Hamberg I, Granqvist CG. Evaporated Sn-doped In2O3 films: Basic optical properties and applications to energy-efficient windows. J Appl Phys [Internet]. 1986 Dec 1;60(11):R123–60. Available from: https://doi.org/10.1063/1.337534
33. Banyamin ZY, Kelly PJ, West G, Boardman J. Electrical and optical properties of fluorine doped tin oxide thin films prepared by magnetron sputtering. Coatings. 2014 Dec 1;4(4):732–46.
34. Bhachu DS, Waugh MR, Zeissler K, Branford WR, Parkin IP. Textured fluorine-doped tin dioxide films formed by chemical vapour deposition. Chemistry - A European Journal. 2011 Oct 4;17(41):11613–21.
35. Suffner J, Ágoston P, Kling J, Hahn H. Chemical vapor synthesis of fluorine-doped SnO2 (FTO) nanoparticles. Journal of Nanoparticle Research. 2010 Sep;12(7):2579–88.

36. Noor N, Parkin IP. Enhanced transparent-conducting fluorine-doped tin oxide films formed by Aerosol-Assisted Chemical Vapour Deposition. J Mater Chem C Mater. 2013 Feb 7;1(5):984–96.
37. Mıˆinea LM, Suh S, Bott SG, Liu JR, Chuc WK, Hoffman DM. Materials Synthesis of aluminium and gallium fluoroalkoxide compounds and the low pressure metal-organic chemical vapor deposition of gallium oxide films.
38. Nordberg GF, Fowler BA, Nordberg M, Friberg LT. Handbook on the Toxicology of Metals. 3rd ed. 2007. 975 p.
39. Abdolahzadeh Ziabari A, Rozati SM. Carrier transport and bandgap shift in n-type degenerate ZnO thin films: The effect of band edge nonparabolicity. Physica B Condens Matter. 2012 Dec 1;407(23):4512–7.
40. Scanlon D. CHEM3401 : New Directions in Materials Chemistry : Electronic Materials Lecture 2 : Conductivity Resistivities of Real Materials. In 2016.
41. Dixon SC, Scanlon DO, Carmalt CJ, Parkin IP. N-Type doped transparent conducting binary oxides: An overview. Vol. 4, Journal of Materials Chemistry C. Royal Society of Chemistry; 2016. p. 6946–61.
42. Haacke G. New figure of merit for transparent conductors. J Appl Phys [Internet]. 1976 Sep 1 [cited 2024 Apr 30];47(9):4086–9. Available from: /aip/jap/article/47/9/4086/502461/New-figure-of-merit-for-transparent-conductors
43. Seshan K. Handbook of Thin Film Deposition: Techniques, Processes, and Technologies: Third Edition. Handbook of Thin Film Deposition: Techniques, Processes, and Technologies: Third Edition. 2012 Jun 27;1–392.
44. Depla D, Mahieu S, Greene JE. Sputter Deposition Processes. In: Handbook of Deposition Technologies for Films and Coatings: Science, Applications and Technology. Elsevier; 2009. p. 253–96.
45. Perednis D, Gauckler LJ. Thin Film Deposition Using Spray Pyrolysis. Vol. 14, Journal of Electroceramics. Springer Science + Business Media, Inc. Manufactured in The Netherlands; 2005.
46. Lewis BG, Paine DC. Applications and Processing of Transparent Conducting Oxides Large-Scale Manufacturing of ITO Thin-Film Coatings. MRS Bull. 2011;25:22–7.
47. Mooney JB, Radding SB. Spray Pyrolysis Processing. Ann Rev Mater Sci [Internet]. 1982;12:81–101. Available from: www.annualreviews.org
48. Hench LL, West JK. The Sol-Gel Process [Internet]. Vol. 90, Chem. Rev. 1990. Available from: https://pubs.acs.org/sharingguidelines
49. Al-Dahoudi N. Wet chemical deposition of transparent conducting coatings made of redispersable crystalline ITO nanoparticles on glass and polymeric substrates. 2003.
50. Malandrino G. Chemical Vapour Deposition. Precursors, Processes and Applications. Edited by Anthony C. Jones and Michael L. Hitchman. Angewandte Chemie International Edition. 2009 Sep 28;48(41):7478–9.
51. Hou X, Choy KL. Processing and applications of aerosol-assisted chemical vapor deposition. Chemical Vapor Deposition. 2006;12(10):583–96.
52. Kodas TT (Toivo T, Hampden-Smith MJ. The chemistry of metal CVD. VCH; 1994. 530 p.
53. Chambers SA. Epitaxial growth and properties of thin film oxides. 2000.

54. Xu Y, Yan XT. Chemical Vapour Deposition. 2010 [cited 2024 Dec 17]; Available from: http://link.springer.com/10.1007/978-1-84882-894-0
55. Dobkin DM, Zuraw MK. Principles of Chemical Vapor Deposition. Principles of Chemical Vapor Deposition. 2003;
56. Choy KL. Chemical vapour deposition of coatings. Prog Mater Sci. 2003 Jan 1;48(2):57–170.
57. Jones AC;, Hitchman ML. Chemical Vapour Deposition: Precursors, Processes and Applications.
58. Frey H. Chemical vapor deposition (CVD). Handbook of Thin-Film Technology. 2015 Jan 1;225–52.
59. Thin Film Deposition Principles Practice by Donald Smith - AbeBooks [Internet]. [cited 2024 Dec 17]. Available from: https://www.abebooks.co.uk/book-search/title/thin-film-deposition-principles-practice/author/donald-smith/
60. Qazi SJS, Rennie AR, Cockcroft JK, Vickers M. Use of wide-angle X-ray diffraction to measure shape and size of dispersed colloidal particles. J Colloid Interface Sci. 2009 Oct 1;338(1):105–10.
61. Scherrer P. Nachrichten von der Gesellschaft der Wissenschaften zu Göttingen. Mathematisch-Physikalische Klasse. 1918;2:98.
62. Monshi A, Foroughi MR, Monshi MR. Modified Scherrer Equation to Estimate More Accurately Nano-Crystallite Size Using XRD. World Journal of Nano Science and Engineering. 2012;02(03):154–60.
63. Klug HP, Alexander LE. X-Ray Diffraction Procedures: For Polycrystalline and Amorphous Materials, 2nd Edition. xdpf [Internet]. 1974 [cited 2024 May 1];992. Available from: https://ui.adsabs.harvard.edu/abs/1974xdpf.book.....K/abstract
64. Sanchez-Perez C, Dixon SC, Darr JA, Parkin IP, Carmalt CJ. Aerosol-assisted route to low-E transparent conductive gallium-doped zinc oxide coatings from pre-organized and halogen-free precursor. Chem Sci. 2020 May 21;11(19):4980–90.
65. Fujimura N, Nishihara T, Goto S, Xu J, Lto T. Control of preferred orientation for ZnO x films: control of self-texture. Vol. 130, Journal of Crystal Growth. 1993.
66. Ponja SD, Sathasivam S, Parkin IP, Carmalt CJ. Transparent conductive aluminium and fluorine co-doped zinc oxide films via aerosol assisted chemical vapour deposition. RSC Adv. 2014;4(91):49723–8.
67. Ponja SD, Sathasivam S, Parkin IP, Carmalt CJ. Highly conductive and transparent gallium doped zinc oxide thin films via chemical vapor deposition. Sci Rep. 2020 Dec 1;10(1).
68. Potter DB, Parkin IP, Carmalt CJ. The effect of solvent on Al-doped ZnO thin films deposited via aerosol assisted CVD. RSC Adv. 2018;8(58):33164–73.
69. Lemire A. Zinc Methoxide. In: Encyclopedia of Reagents for Organic Synthesis (EROS) [Internet]. 2012. Available from: https://doi.org/10.1002/047084289X.rn01466
70. Jana S, Berger RJF, Fröhlich R, Pape T, Mitzel NW. Oxygenation of simple zinc alkyls: Surprising dependence of product distributions on the alkyl substituents and the presence of water. Inorg Chem. 2007 May 14;46(10):4293–7.
71. Sokołowski K, Justyniak I, Bury W, Grzonka J, Kaszkur Z, Mąkolski Ł, et al. Tert-BUTYL(tert-butoxy)zinc hydroxides: Hybrid models for

single-source precursors of ZnO nanocrystals. Chemistry - A European Journal. 2015 Mar 27;21(14):5488–95.

72. Walters G, Parkin IP. Aerosol assisted chemical vapour deposition of ZnO films on glass with noble metal and p-type dopants; use of dopants to influence preferred orientation. Appl Surf Sci. 2009 Apr 15;255(13–14):6555–60.
73. Mar GL, Timbrell PY, Lamb RN. Factors Influencing the Chemical Vapor Deposition of Oriented ZnO Films Using Zinc Acetate. Chem Mater [Internet]. 1995 [cited 2024 May 2];7:1890–6. Available from: https://pubs.acs.org/sharingguidelines
74. Potter DB, Powell MJ, Parkin IP, Carmalt CJ. Aluminium/gallium, indium/gallium, and aluminium/indium co-doped ZnO thin films deposited: Via aerosol assisted CVD. J Mater Chem C Mater. 2018;6(3):588–97.
75. Sanchez-Perez C, Sriluxmi Srimurugananthan ab, Sotelo-Vazquez C, Sathasivam S, Mingyue Wang ad, Marugá J, et al. Self-textured ZnO via AACVD of alkyl alkoxides: a solution-based seed-less route towards optoelectronic-grade coatings †. Cite this: Mater Adv [Internet]. 2023 [cited 2024 May 1];4:3774. Available from: https://doi.org/
76. Langford JI, Wilson AJC. Seherrer after Sixty Years: A Survey and Some New Results in the Determination of Crystallite Size. Vol. 11, J. Appl. Cryst. 1978.
77. And G, Tauc SJ. OPTICAL PROPERTIES AND ELECTRONIC STRUCTURE OF AMORPHOUS. Mat Res Bull. 3:37–46.
78. Hamberg I, Granqvist CG. Evaporated Sn-doped In2O3 films: Basic optical properties and applications to energy-efficient windows. J Appl Phys [Internet]. 1986 Dec 1 [cited 2024 May 2];60(11):R123–60. Available from: /aip/jap/article/60/11/R123/172211/Evaporated-Sn-doped-In2O3-films-Basic-optical
79. Viezbicke BD, Patel S, Davis BE, Birnie DP. Evaluation of the Tauc method for optical absorption edge determination: ZnO thin films as a model system. physica status solidi (b) [Internet]. 2015 Aug 1 [cited 2024 May 2];252(8):1700–10. Available from: https://onlinelibrary.wiley.com/doi/full/10.1002/pssb.201552007
80. Dolgonos A, Mason TO, Poeppelmeier KR. Direct optical band gap measurement in polycrystalline semiconductors: A critical look at the Tauc method. 2016 [cited 2024 May 2]; Available from: http://dx.doi.org/10.1016/j.jssc.2016.05.010
81. Oba F, Togo A, Tanaka I, Paier J, Kresse G. Defect energetics in ZnO: A hybrid Hartree-Fock density functional study.
82. Wang L, Giles NC. Temperature dependence of the free-exciton transition energy in zinc oxide by photoluminescence excitation spectroscopy. J Appl Phys. 2003 Jul 15;94(2):973–8.
83. Clark SJ, Robertson J, Lany S, Zunger A. Intrinsic defects in ZnO calculated by screened exchange and hybrid density functionals. Phys Rev B Condens Matter Mater Phys [Internet]. 2010 Mar 10 [cited 2024 May 2];81(11):115311. Available from: https://journals.aps.org/prb/abstract/10.1103/PhysRevB.81.115311
84. Dixon SC, Sathasivam S, Williamson BAD, Scanlon DO, Carmalt CJ, Parkin IP. Transparent conducting n-type ZnO:Sc – synthesis, optoelectronic properties and theoretical insight. J Mater Chem C Mater

[Internet]. 2017 Aug 3 [cited 2024 May 2];5(30):7585–97. Available from: https://pubs.rsc.org/en/content/articlehtml/2017/tc/c7tc02389h

85. Majeed Khan MA, Kumar S, Naziruddin Khan M, Ahamed M, Al Dwayyan AS. Microstructure and blueshift in optical band gap of nanocrystalline AlxZn1−xO thin films. J Lumin. 2014 Nov 1;155:275–81.
86. Mora-Fonz D, Shluger AL. Making amorphous ZnO: Theoretical predictions of its structure and stability. Phys Rev B [Internet]. 2019 Jan 4 [cited 2024 May 2];99(1):014202. Available from: https://journals.aps.org/prb/abstract/10.1103/PhysRevB.99.014202
87. Tan ST, Chen BJ, Sun XW, Fan WJ, Kwok HS, Zhang XH, et al. Blueshift of optical band gap in ZnO thin films grown by metal-organic chemical-vapor deposition. J Appl Phys [Internet]. 2005 Jul 1 [cited 2024 May 2];98(1). Available from: /aip/jap/article/98/1/013505/796607/Blueshift-of-optical-band-gap-in-ZnO-thin-films
88. Guermat N, Daranfed W, Mirouh K. Extended wide band gap amorphous zno thin films deposited by spray pyrolysis. Annales de Chimie: Science des Materiaux. 2020 Oct 1;44(5):347–52.
89. Liu Y, Li Y, Zeng H. ZnO-based transparent conductive thin films: Doping, performance, and processing. Vol. 2013, Journal of Nanomaterials. 2013.
90. Manzi JA, Knapp CE, Parkin IP, Carmalt CJ. Aerosol-Assisted Chemical-Vapour Deposition of Zinc Oxide from Single-Source β-Iminoesterate Precursors. Eur J Inorg Chem [Internet]. 2015 Aug 1 [cited 2024 May 2];2015(22):3658–65. Available from: https://onlinelibrary.wiley.com/doi/full/10.1002/ejic.201500416
91. Singh T, Lehnen T, Leuning T, Sahu D, Mathur S. Thickness dependence of optoelectronic properties in ALD grown ZnO thin films. Appl Surf Sci. 2014 Jan 15;289:27–32.
92. Vispute SD, Noch RD, Balsamo W, Sharma AP, Venkatesan RP, Iliadis T, et al. Oxygen Pressure-Tuned Epitaxy and Optoelectronic Properties of Laser-Deposited ZnO Films on Sapphire [Internet]. Vol. 75, Applied Physics Letters. 1999. Available from: https://corescholar.libraries.wright.edu/physicshttps://corescholar.libraries.wright.edu/physics/61
93. Stegmann C, Muench F, Rauber M, Hottes M, Brötz J, Kunz U, et al. Platinum nanowires with pronounced texture, controlled crystallite size and excellent growth homogeneity fabricated by optimized pulsed electrodeposition. RSC Adv. 2014;4(10):4804–10.
94. Bhachu DS, Sankar G, Parkin IP. Aerosol assisted chemical vapor deposition of transparent conductive zinc oxide films. Chemistry of Materials. 2012 Dec 21;24(24):4704–10.
95. Zhang H, Yang S, Liu H, Yuan C. Preparation and characterization of transparent conducting ZnO:W films by DC magnetron sputtering. Journal of Semiconductors. 2011 Apr;32(4).
96. Gulino A, Fragala I. Deposition and characterization of transparent thin films of zinc oxide doped with Bi and Sb. Chemistry of Materials. 2002;14(1):116–21.
97. Karamat S, Rawat RS, Lee P, Tan TL, Ke C, Chen R, et al. Ferromagnetic signature in vanadium doped ZnO thin films grown by

pulsed laser deposition. J Mater Res [Internet]. 2016/10/03. 2016;31(20):3223–9. Available from: https://www.cambridge.org/core/article/ferromagnetic-signature-in-vanadium-doped-zno-thin-films-grown-by-pulsed-laser-deposition/8B39F1F9CB5041C14C41D4293AAEFC4B

98. Gao Y, Hong YL, Yin LC, Wu Z, Yang Z, Chen ML, et al. Ultrafast Growth of High-Quality Monolayer WSe2 on Au. Advanced Materials. 2017 Aug 4;29(29).

99. Chirakkara S, Krupanidhi SB. Gallium and indium co-doped ZnO thin films for white light emitting diodes. Physica Status Solidi - Rapid Research Letters. 2012 Jan;6(1):34–6.

100. Noor N, Chew CKT, Bhachu DS, Waugh MR, Carmalt CJ, Parkin IP. Influencing FTO thin film growth with thin seeding layers: a route to microstructural modification. J Mater Chem C Mater. 2015 Aug 11;3(36):9359–68.

101. Sánchez-Martín S, Olaizola SM, Castaño E, Urionabarrenetxea E, Mandayo GG, Ayerdi I. Study of deposition parameters and growth kinetics of ZnO deposited by aerosol assisted chemical vapor deposition. RSC Adv. 2021 May 18;11(30):18493–9.

102. Durrani SMA, Khawaja EE, Al-Shukri AM, Al-Kuhaili MF. Dielectric/Ag/dielectric coated energy-efficient glass windows for warm climates. Energy Build. 2004 Sep;36(9):891–8.

103. Zhang L, Zhou Y, Guo L, Zhao W, Barnes A, Zhang HT, et al. Correlated metals as transparent conductors. Nat Mater. 2016 Feb 1;15(2):204–10.

104. Waugh MR, Hyett G, Parkin IP. Zinc oxide thin films grown by aerosol assisted CVD. Chemical Vapor Deposition. 2008;14(11–12):366–72.

105. Carta G, El Habra N, Rossetto G, Torzo G, Crociani L, Natali M, et al. Growth of hafnium dioxide thin films by MOCVD using a new series of cyclopentadienyl hafnium compounds. Chemical Vapor Deposition. 2007 Nov;13(11):626–32.

106. Yang Y, Jin S, Medvedeva JE, Ireland JR, Metz AW, Ni J, et al. CdO as the archetypical transparent conducting oxide. Systematics of dopant ionic radius and electronic structure effects on charge transport and band structure. J Am Chem Soc. 2005 Jun 22;127(24):8796–804.

107. Knapp CE, Hyett G, Parkin IP, Carmalt CJ. Aerosol-assisted chemical vapor deposition of transparent conductive gallium-indium-oxide films. Chemistry of Materials. 2011 Apr 12;23(7):1719–26.

108. Srikant V, Clarke DR. On the optical band gap of zinc oxide. J Appl Phys [Internet]. 1998 May 15;83(10):5447–51. Available from: https://doi.org/10.1063/1.367375

109. Kumar J, Kumar Srivastava A. Band gap narrowing in zinc oxide-based semiconductor thin films. J Appl Phys. 2014 Apr 7;115(13).

110. Janotti A, Van De Walle CG. Fundamentals of zinc oxide as a semiconductor. Reports on Progress in Physics. 2009;72(12).

111. Ebrahimifard R, Golobostanfard MR, Abdizadeh H. Sol-gel derived Al and Ga co-doped ZnO thin films: An optoelectronic study. Appl Surf Sci. 2014 Jan 30;290:252–9.

112. Hu J, Gordon RG. Atmospheric pressure chemical vapor deposition of gallium doped zinc oxide thin films from diethyl zinc, water, and triethyl gallium. J Appl Phys. 1992;72(11):5381–92.

113. Babar AR, Deshamukh PR, Deokate RJ, Haranath D, Bhosale CH, Rajpure KY. Gallium doping in transparent conductive ZnO thin films prepared by chemical spray pyrolysis. J Phys D Appl Phys. 2008 Jul 7;41(13).
114. Aragones AC, Palacios-Padros A, Caballero-Briones F, Sanz F. Study and improvement of aluminium doped ZnO thin films: Limits and advantages. Electrochim Acta. 2013;109:117–24.
115. Ben Ayadi Z, Mahdhi H, Djessas K, Gauffier JL, El Mir L, Alaya S. Sputtered Al-doped ZnO transparent conducting thin films suitable for silicon solar cells. In: Thin Solid Films. 2014. p. 123–6.
116. Saarenpää H, Niemi T, Tukiainen A, Lemmetyinen H, Tkachenko N. Aluminum doped zinc oxide films grown by atomic layer deposition for organic photovoltaic devices. Solar Energy Materials and Solar Cells. 2010 Aug;94(8):1379–83.
117. Ohgaki T, Kawamura Y, Kuroda T, Ohashi N, Adachi Y, Tsurumi T, et al. Optical Properties of Heavily Aluminum-Doped Zinc Oxide Thin Films Prepared by Molecular Beam Epitaxy. Key Eng Mater [Internet]. 2003 Aug [cited 2024 Apr 30];248:91–4. Available from: https://www.scientific.net/KEM.248.91
118. Sans JA, Sánchez-Royo JF, Segura A, Tobias G, Canadell E. Chemical effects on the optical band-gap of heavily doped ZnO: MIII (M=Al,Ga,In): An investigation by means of photoelectron spectroscopy, optical measurements under pressure, and band structure calculations. Phys Rev B Condens Matter Mater Phys [Internet]. 2009 May 1 [cited 2024 Apr 30];79(19):195105. Available from: https://journals.aps.org/prb/abstract/10.1103/PhysRevB.79.195105
119. Hung-Chun Lai H, Basheer T, Kuznetsov VL, Egdell RG, J Jacobs RM, Pepper M, et al. Dopant-induced bandgap shift in Al-doped ZnO thin films prepared by spray pyrolysis □Dopant-induced bandgap shift in Al-doped ZnO thin films prepared by spray pyrolysis. J Appl Phys [Internet]. 2012 [cited 2024 Apr 30];112:83708. Available from: https://doi.org/10.1063/1.4759208
120. van Deelen J, Illiberi A, Kniknie B, Steijvers H, Lankhorst A, Simons P. APCVD of ZnO:Al, insight and control by modeling. Surf Coat Technol. 2013 Sep 15;230:239–44.
121. Ponja SD, Sathasivam S, Parkin IP, Carmalt CJ. Transparent conductive aluminium and fluorine co-doped zinc oxide films via aerosol assisted chemical vapour deposition. RSC Adv [Internet]. 2014 Oct 6 [cited 2024 Apr 30];4(91):49723–8. Available from: https://pubs.rsc.org/en/content/articlehtml/2014/ra/c4ra09997d
122. Kim H, Auyeung RCY, Piqué A. Transparent conducting F-doped SnO2 thin films grown by pulsed laser deposition. Thin Solid Films. 2008 Jun 2;516(15):5052–6.
123. Potter DB, Bhachu DS, Powell MJ, Darr JA, Parkin IP, Carmalt CJ. Al-, Ga-, and In-doped ZnO thin films via aerosol assisted CVD for use as transparent conducting oxides. physica status solidi (a) [Internet]. 2016 May 1 [cited 2024 Apr 30];213(5):1346–52. Available from: https://onlinelibrary.wiley.com/doi/full/10.1002/pssa.201532996
124. Bhachu DS, Sankar G, Parkin IP. Aerosol assisted chemical vapor deposition of transparent conductive zinc oxide films. Chemistry of Materials. 2012 Dec 21;24(24):4704–10.

125. Fujimura N, Nishihara T, Goto S, Xu J, Ito T. Control of preferred orientation for ZnOx films: control of self-texture. J Cryst Growth [Internet]. 1993;130(1):269–79. Available from: https://www.sciencedirect.com/science/article/pii/002202489390861P
126. Ponja SD, Sathasivam S, Parkin IP, Carmalt CJ. Transparent conductive aluminium and fluorine co-doped zinc oxide films via aerosol assisted chemical vapour deposition. RSC Adv. 2014;4(91):49723–8.
127. Jayathilake DSY, Peiris TAN, Sagu JS, Potter DB, Wijayantha KGU, Carmalt CJ, et al. Microwave-Assisted Synthesis and Processing of Al-Doped, Ga-Doped, and Al, Ga Codoped ZnO for the Pursuit of Optimal Conductivity for Transparent Conducting Film Fabrication. ACS Sustain Chem Eng. 2017 Jun 5;5(6):4820–9.
128. Shukla RK, Srivastava A, Srivastava A, Dubey KC. Growth of transparent conducting nanocrystalline Al doped ZnO thin films by pulsed laser deposition. J Cryst Growth [Internet]. 2006;294(2):427–31. Available from: https://www.sciencedirect.com/science/article/pii/S0022024806006178
129. Theis W. A Simple Classical Derivation of Spin-Orbit Couplings. Z Physik A. 1979;290:355–8.
130. Beck G, Davidovich N. On spin-orbit coupling. Il Nuovo Cimento B (1971-1996) [Internet]. 1975;27(1):19–26. Available from: https://doi.org/10.1007/BF02726334
131. Dresselhaus G, Kip AF, Kittel C. Plasma Resonance in Crystals: Observations and Theory*. Physical Review. 1955;100(2):618–25.
132. Elliott RJ. Theory of the Effect of Spin-Orbit Coupling on Magnetic Resonance in Some Semiconductors. Phys Rev. 1954;96(2):266.
133. Gulino A, Fragala I. Deposition and characterization of transparent thin films of zinc oxide doped with Bi and Sb. Chemistry of Materials. 2002;14(1):116–21.
134. Theis W, Horn K. Temperature-dependent line broadening in core-level photoemission spectra from aluminum. Vol. 47, PHYSICAL REVIEW B. 1993.
135. Berg C, Raaen S, Borg A, Andersen JN, Lundgren E, Nyholm R. Observation of a low-binding-energy peak in the 2 *p* core-level photoemission from oxidized Al(111). Phys Rev B [Internet]. 1993 May 15 [cited 2023 Jun 28];47(19):13063–6. Available from: https://link.aps.org/doi/10.1103/PhysRevB.47.13063
136. Miller AC, McCluskey FP, Taylor JA. An x-ray photoelectron spectroscopy study of aluminum surfaces treated with fluorocarbon plasmas. Journal of Vacuum Science & Technology A [Internet]. 1991 May 1;9(3):1461–5. Available from: https://doi.org/10.1116/1.577646
137. Domen K, Chuang TJ. Laser induced photodissociation and desorption. I. CH2I2 adsorbed on Al2O3. J Chem Phys [Internet]. 1989 Mar 15;90(6):3318–31. Available from: https://doi.org/10.1063/1.455886
138. Kim KH, Park KC, Ma DY. Structural, electrical and optical properties of aluminum doped zinc oxide films prepared by radio frequency magnetron sputtering. J Appl Phys [Internet]. 1997 Jun 15 [cited 2024 May 1];81(12):7764–72. Available from: /aip/jap/article/81/12/7764/492528/Structural-electrical-and-optical-properties-of

139. Al Asmar R, Juillaguet S, Ramonda M, Giani A, Combette P, Khoury A, et al. Fabrication and characterization of high quality undoped and Ga2O3-doped ZnO thin films by reactive electron beam co-evaporation technique. J Cryst Growth. 2005 Mar 1;275(3–4):512–20.
140. Shannon RD, IUCr. Revised effective ionic radii and systematic studies of interatomic distances in halides and chalcogenides. urn:issn:0567-7394 [Internet]. 1976 Sep 1 [cited 2024 May 1];32(5):751–67. Available from: //scripts.iucr.org/cgi-bin/paper?a12967
141. Jun MC, Park SU, Koh JH. Comparative studies of Al-doped ZnO and Ga-doped ZnO transparent conducting oxide thin films. 2012 [cited 2024 May 1]; Available from: http://www.nanoscalereslett.com/content/7/1/639
142. Ohyama M, Kozuka H, Yoko T. Sol-Gel Preparation of Transparent and Conductive Aluminum-Doped Zinc Oxide Films with Highly Preferential Crystal Orientation. Journal of the American Ceramic Society [Internet]. 1998 Jun 1;81(6):1622–32. Available from: https://doi.org/10.1111/j.1151-2916.1998.tb02524.x
143. Miki-Yoshida M, Paraguay-Delgado F, Estrada-López W, Andrade E. Structure and morphology of high quality indium-doped ZnO films obtained by spray pyrolysis. Thin Solid Films [Internet]. 2000;376(1):99–109. Available from: https://www.sciencedirect.com/science/article/pii/S0040609000014085
144. Shinde SS, Shinde PS, Pawar SM, Moholkar A V, Bhosale CH, Rajpure KY. Physical properties of transparent and conducting sprayed fluorine doped zinc oxide thin films. Solid State Sci [Internet]. 2008;10(9):1209–14. Available from: https://www.sciencedirect.com/science/article/pii/S1293255807003603
145. Krajewski TA, Luka G, Smertenko PS, Zakrzewski AJ, Dybko K, Jakiela R, et al. Schottky Junctions Based on the ALD-ZnO Thin Films for Electronic Applications. Vol. 120. 2011.
146. Krause-Rehberg R, Leipner H. Positron annihilation in semiconductors: defect studies. 1999 [cited 2024 May 1]; Available from: https://books.google.com/books?hl=en&lr=&id=WXOkEvr4sxcC&oi=fnd&pg=PR13&ots=bSVDKGtVl7&sig=EyfTF-HP4pZ77gHcsry57CLZ91s
147. Selim FA, Weber MH, Solodovnikov D, Lynn KG. Nature of native defects in ZnO. Phys Rev Lett [Internet]. 2007 Aug 21 [cited 2024 May 1];99(8):085502. Available from: https://journals.aps.org/prl/abstract/10.1103/PhysRevLett.99.085502
148. Brauer G, Anwand W, Grambole D, Grenzer J, Skorupa W, Čížek J, et al. Identification of Zn-vacancy-hydrogen complexes in ZnO single crystals: A challenge to positron annihilation spectroscopy. Phys Rev B Condens Matter Mater Phys [Internet]. 2009 Mar 3 [cited 2024 May 1];79(11):115212. Available from: https://journals.aps.org/prb/abstract/10.1103/PhysRevB.79.115212
149. Uedono A, Koida T, Tsukazaki A, Kawasaki M, Chen ZQ, Chichibu SF, et al. Defects in ZnO thin films grown on ScAlMgO4 substrates probed by a monoenergetic positron beam. J Appl Phys. 2003 Mar 1;93(5):2481–5.
150. Peng CX, Weng HM, Yang XJ, Ye BJ, Cheng B, Zhou XY, et al. Dependence of intrinsic defects in ZnO films on oxygen fraction studied

by positron annihilation. Chinese Physics Letters. 2006 Feb 1;23(2):489–92.

151. Zubiaga A, García JA, Plazaola F, Tuomisto F, Saarinen K, Zuñiga Pérez J, et al. Correlation between Zn vacancies and photoluminescence emission in ZnO films. J Appl Phys. 2006 Mar 1;99(5):053516.